Microstructures and Deformation Mechanisms of Ballistic Impacts in Stone

Oliver Campbell

Submitted for the degreee of

Doctor of Philosophy

at Cardiff University

Wales

December 2022

Abstract

Bullet impacts are a ubiquitous form of damage to the built environment arising from armed conflicts. The risk of damage to cultural heritage is increasing as armed conflicts shift towards more urbanised centres, yet the effects and mechanisms of small arms damage are unclear. The aim of this thesis is to investigate the damage morphology and mechanisms of bullet impacts into stone. The influences of target materials, impact angle, and projectile type on damage in limestone and sandstone, was investigated through a series of controlled experiments.

A proof of concept study showed that digital documentation can be an effective method for quantifying the surface morphology of impact damage, and that surface and subsurface damage are linked. Controlled firearm impacts were undertaken to study the influence of projectile type, target material, and angle of impact on surface and subsurface damage. Structure from motion photogrammetry produced 3D models of damage for quantitative analysis. The results showed that bullet impacts into natural stone targets at engagement distances of approximately 200m cause approximately conical craters, with some impacts having a complex two-part structure. Radial fractures centred on the impact crater are commonly present, and can reach sides adjacent to the target face. Oblique impact trajectories result in asymmetric crater morphologies that can be distinguished from damage caused by perpendicular trajectories.

In the subsurface, damage is characterised by grain crushing and pore space collapse close to the impact point, with discrete open fractures characterising damage further away. Both surface and subsurface fractures have circum- and transgranular pathways close to the impact, but with increasing distance tend towards predominantly circumgranular pathways. Fracture intensity analysis reveals high fracture intensities close to the impact, which reduce beyond a distance of 10 mm from the impact. Conical fractures, or zones of increased fracture intensity, dip away from the crater centre, with the potential to form interconnected networks in the subsurface.

Cratering from bullet impacts into stone is controlled by momentum transfer, meaning target and projectile properties have a strong influence on damage morphology. Limestone targets exhibited wider, deeper, and more voluminous craters than impacts in sandstone targets . Craters caused by a 5.56 $\times$ 45 mm NATO projectile, containing a steel tip, were wider and deeper than craters caused by a 7.62 $\times$ 39 mm, without a steel tip, under comparable conditions.

Contents

List of Tables

List of Figures

Acknowledgements

First and foremost I want to thank my primary supervisor, Prof. Tom Blenkinsop. This thesis would not have been possible without his excellent guidance and advice over the last four years. His patience in reading countless drafts and early manuscripts has helped me to become the researcher that I am today. For that, I am immensely grateful. Secondly, a huge thanks to my other supervisor Dr Lisa Mol, for obtaining funding for this project and providing me with opportunities that I would not have conceived at the start of the project. I would be remiss if I did not mention other members of the the Heritage in the Crossfire Group who have provided valuable support, technical advice, and stimulating conversations throughout the course of this process, so thank you Charlotte, Lucy, Kaitlyn, and Casey. Funding for this project was provided by The Leverhulme Trust, grant number RPG-2017-408.

Further gratitude is owed to Oscar, through all of the delays in organising experiments, late nights in the lab, early mornings on the road, and dreary days at the firing range, his company and conversation made them a memorable part of this experience. I am grateful for the friendship we have forged through joint adversary, although I feel I may have had the better end of the stick in that regard.

Everyone's PhD journey is different, but global events during the course of this project have given me a shared experience with so many others. To all those I met in Cardiff whilst the world was 'normal': Ben, Ana, Will, Erin, Sophie, and Manny, I am truly grateful for the games of table tennis and after work pub visits whilst we still could. I wish them all the greatest of success in their future careers, for they are all wonderful people who deserve it. I'd also like to thank: Max for being a great housemate and for the chill evenings on our controversial 'balcony', Ben, Alex, Levent, and Suame of the Cracks and Copper reading group for their engaging discussions and helpful feedback on early manuscripts, Ian Thomas for sharing some of his vast Python knowledge to make much of this thesis possible, and finally to Anthony Oldroyd for his assistance in preparing

my numerous thin sections.

I owe special thanks to my friends from home, whose mere presence in my life assisted me during times of stress and difficulty. As scattered as we are now, the laughter, kindness, and generosity of them all has been a constant. So I thank: Matt (the bread one), Adam, Jack, other Matt (Jake's dad), Gemma, and Dave.

For my family, few words can do justice to the gratitude I have for them. My parents were always willing to assist me in any way they could, even spending weekends making prototype contraptions out of dustbins and tarpaulin. I may not have said it enough or at all, but Mum, Dad, and Hannah, I am truly thankful for you all. I must also thank all of my Grandparents, for their love and support has guided me through life and brought me to this moment.

This thesis has at times been one of my toughest challenges, but thankfully in those instances I was never alone. From the beginning, my partner Charlotte has been there for me, an unshakeable foundation of strength and a source of great reassurance, love, and pride. You are truly an amazing person and I would not be who I am today without you.

This thesis is dedicated to those in my life who are no longer here to see it complete, or to see the person I have come to be.

Chapter 1

Introduction

1.1 Armed Conflict and Heritage

Many modern rebel groups, terrorist organisations, and non-state militias utilise abundant Cold War era stocks of weapons (Greene & Macaspac Penetrante, 2012). For example, weapons used by Islamic State (IS) are predominantly AK variant assault rifles of differing origins, mainly ex-Soviet and Chinese manufactured. Seizures also show a large number of AR-15 pattern rifles, such as the US made M16 and M4 (Conflict Armament Research, 2014; Amnesty International, 2015). The rapid fire rates (hundreds of rounds per minute) and high muzzle velocities ($>$700 $\mathrm{m\,s^{-1}}$) of these types of small arms mean each projectile has substantial potential to cause damage. Conflict Armament Research's (2014) report highlights the variety of weapons available to non-state actors, listing more than just rifles and machine guns, with personal anti-tank weapons, artillery pieces, and improvised explosive devices also common. Contemporary armed conflicts regularly occur within urbanised environments due to the prevalence of insurgency tactics and the increased urbanisation of today's world (Stone, 2015). The diversity of small arms (and therefore ammunition type) and artillery being utilised in these environments will likely have diverse, and yet unquantified, damage types. The diversity of impacts from small arms and shrapnel therefore present an ever increasing risk to cultural heritage.

The United Nation's (1972) definition of cultural heritage emphasises the 'outstanding universal value' that it provides, and includes:

- Monuments: Architectural works, works of sculpture and painting, elements of structures of an archaeological nature, inscriptions cave dwellings and combination of features, which are

of an outstanding universal value from the point of view of history, art, or science.

- Groups of Buildings: Groups of separate or connected buildings which, because of their architecture, their homogeneity or their place in the landscape, are of outstanding universal value from the point of view of history, art, or science.

- Sites: Works of man or combined works of nature and man, and areas including archaeological sites which are of outstanding value for the historical, aesthetic, ethnological or anthropological point of view (Section I, Article 1).

These broad definitions mean that many buildings, monuments, and sites in urban areas are classified as cultural heritage, making any intentional damage a war crime. Aware of this threat, UNESCO further classifies conflict damage into four categories: intentional damage, collateral damage, forced neglect, and organised trafficking/looting (Weiss & Connelly, 2017). Despite these protections under international law, cultural heritage is regularly both a target and unfortunate collateral of armed conflicts.

The most dramatic manifestations are the destruction of culturally significant sites by explosives, rockets, and heavy artillery. Ideological extremism has led to the targeted demolition of hundreds of cultural sites across the Middle East and North Africa (MENA) region, such as in Afghanistan, Syria, and Iraq (Weiss & Connelly, 2017; Isakhan & González Zarandona, 2018). Meanwhile, Russia's invasion of Ukraine in February 2022 has led to high profile examples of conflict damage to heritage due to urban fighting and the use of long range missiles and artillery, including to places of worship, museums, cemeteries, and war memorials (MKIP, 2022). Damage caused by small arms projectiles (bullets) and shrapnel is ubiquitous in conflict zones and affects a wide area around missile and artillery impact sites. Despite its abundance, there has been little targeted, quantified investigation into the effects of this damage on material properties and future deterioration.

1.2 Impact Studies

The following terms which are widely used later are defined here (Backman & Goldsmith, 1978):

- The **Target** simply refers to the object or material that is being impacted by the projectile. Its use does not necessarily imply intent or purposeful aim.

- The **Projectile** is the object that is impacting the target.

- **Perforation** is the complete passage of a projectile though a target.
- **Penetration** is when a projectile is stopped by the target.
- **Ricochet** is when the projectile is deflected by the target, such that there is no complete perforation.
- **Spallation** refers to material ejected from the target as a result of projectile impact. If the target is perforated, then spall can be ejected due to the entry or exit of the projectile, and is differentiated based on its face of origin, e.g. front face or rear face spall.

Since the invention of early firearms there have been investigations into the effects of projectile impacts into various materials (Robins, 1742; Helié, 1840; Bahsforth, 1873; Robertson, 1941). However, the first studies of projectiles and impact conditions relevant to this thesis stem from military testing conducted during World War Two (WWII). These studies did not investigate in detail the subsurface damage in target materials, nor its effect on future deterioration. Instead, they primarily focused on the penetration and perforation resistance of construction materials, such as concrete and brick, to various projectiles ranging from .30 calibre bullets up to 1000 lb bombs. These target materials differ from the various natural stone materials used commonly used in heritage sites. Bullet impacts of .30 and .50 calibre projectiles into concrete targets create roughly conical, but irregular craters through spalling of target material. Impacts also exhibit crushed material below, and spoke-like fractures centred about the impact (White, 1946). Experiments simulating the impacts of bomb shrapnel into concrete observed funnel-shaped craters with radial fractures (Road Research Laboratory, 1941). In some studies, radial fractures reach the edge of the target block and fracture along block-mortar boundaries instead of traversing into adjacent blocks (Tolch & Bushkovitch, 1947). The (semi-) conical crater, grain crushing below the impact, radial fractures, and ejected material are common observations across a range of projectile impacts into concrete (non-reinforced and reinforced) and natural rock targets (White, 1946; Tolch & Bushkovitch, 1947; Yankelevsky, 1997; Frew, 2001; Booker et al., 2009; Soe et al., 2013; Kosteski et al., 2015; Sovják et al., 2015; Rosenberg & Dekel, 2016; Rajput & Iqbal, 2017). Relationships between impact variables, such as projectile velocity and penetration depth, can be derived (Backman & Goldsmith, 1978; Rosenberg & Dekel, 2016). These empirical relationships primarily focus on calculating the ballistic limit (i.e. the minimum velocity of a projectile to reliable penetrate a target) of various metal tiles. The ductile nature of metal target materials mean there is less focus on variables such as crater volume (Backman & Goldsmith, 1978).

Hypervelocity (>1,500 $m\,s^{-1}$) experiments simulating meteorite impacts exhibit damage similar to the ordnance experiments described above. Crater profiles from hypervelocity impacts have deeper central penetrations and a shallower dipping surrounding spall zone, similar to ordnance velocity impacts (Moore et al., 1963; Hörz, 1969; Lange et al., 1984; Polanskey & Ahrens, 1990; Kenkmann et al., 2018). Radial fractures are centred on the crater and grain crushing and pore space collapse are observed directly below the impact (Polanskey & Ahrens, 1990; Buhl, Kowitz, et al., 2013). Like ordnance velocity experiments, relationships between impact variables and damage can be derived, but unlike ordnance velocity experiments, these relationships focus on variables such as crater depth, diameter, and volume (Gault et al., 1963; Moore et al., 1963; Melosh, 1980; Holsapple & Schmidt, 1982; Holsapple & Schmidt, 1987). A series of dimensionless parameters (known as Pi-scaling parameters) can also be derived, enabling comparison between different target materials and impact variables. Cratering in hypervelocity experiments is primarily controlled by energy transfer and a spherical shock wave. There is an overlap in the range of variables between ordnance and hypervelocity impact experiments, and although impact damage is similar in appearance, the relevance of hypervelocity impact studies to ordnance velocity impacts is unclear. It is also unclear how different impact variables, such as target properties, impact angle, and projectile properties, affect the morphology and severity of damage.

1.3 Implications for Heritage

Impacts from bullets and shrapnel are one element in the spectrum of damage sustained by heritage during armed conflict, which is often overlooked in initial damage assessments. There are few studies on the quantitative effects of this widespread form of damage, but initial studies suggest small arms impacts exacerbate deterioration of stone in the long term (Mol et al., 2017; Mol & Gomez-Heras, 2018; Gilbert et al., 2020). Small scale impacts from .22 calibre lead bullets into sandstone targets realign clay minerals beneath the impact (Mol & Green, 2015). This can act to reduce the near surface permeability in the immediate vicinity of the impact (Mol & Green, 2015; Mol et al., 2017). Targets that have undergone case hardening are less susceptible to moisture ingress because pore spaces near the surface have been infilled with cement (if naturally case hardened) or by consolidants (if artificially case hardened). However, case hardened materials have a lower surface elasticity and exhibit greater fracturing as a result when impacted, compared to unhardened surfaces, suggesting that target properties may influence the resultant damage (Mol et al., 2017). Larger impacts caused by higher calibre rifle bullets and shrapnel show that

the most severe weakening is not directly under the impact point, but in the regions surrounding the impact (Mol & Gomez-Heras, 2018; Gilbert et al., 2019). Mol and Gomez-Heras (2018) found that fracture networks and energy dissipation caused by relatively contemporaneous (1936 – 1939) weaponry are more complicated and extensive than damage caused by older firearms (such as 17^{th} muskets). Ballistic theory quantifies an array of variables influencing the partitioning of damage during impacts, but fundamentally damage is controlled by the energy of the system. The primary source of energy at impact is the projectile's kinetic energy ($E_K = 0.5mv_i{}^2$), which is proportional to v_i^2 Average muzzle velocities of historic muskets were 400 – 500 $\mathrm{m\,s^{-1}}$, but the aerodynamic inefficiency of spherical projectiles causes rapid deceleration with distance, at rates of 2.5 $\mathrm{m\,s^{-1}}$ per metre travelled (Krenn et al., 1995). Modern firearms, with rifled barrels, more aerodynamic projectile shapes, and improved propellants, have greater average muzzle velocities (700 – 1000 $\mathrm{m\,s^{-1}}$) and lower deceleration rates (0.6 – 1 $\mathrm{m\,s^{-1}}$ per metre travelled). This results in modern projectiles retaining a greater proportion of their muzzle velocity at impact, resulting in greater impact energies than historic firearms. Modern projectiles are also comprised of multiple materials, typically a lead or steel core surrounded by a copper jacket. The shape and composition of modern projectiles result in more efficient target penetration than spherical lead projectiles (Backman & Goldsmith, 1978; Collins et al., 2011). Mol and Gomez-Heras (Mol & Gomez-Heras, 2018) also observed large open fractures sub-parallel to unconfined faces on window ledges damaged during the Spanish Civil War (1936 – 1939). These initial studies all indicate that the damage caused by bullet and shrapnel impacts can alter target properties and that overall damage might be more significant than just the visible surface damage. However there is little understanding from observations and measurements of surface damage as to how it is related to subsurface damage. It is vital to a comprehensive understanding of conflict damaged heritage that relationships between the surface and subsurface damage are understood.

The changes in stone properties caused by impact aid the ingress of weathering agents such as moisture and dissolved salts, enlarging the volume of stonework at risk of deterioration (Lebedeva & Brantley, 2017). A higher effective porosity, i.e. the combination of inherent porosity and impact induced fractures, facilitates greater ingress of moisture via capillary flow (Scherer, 2004). This moisture can dissolve matrix and constituent minerals, reducing overall stone strength and further increasing its effective porosity. Moisture transports dissolved salts into the stonework that create outward pressures upon crystallisation, widening pore spaces and fractures. This results in the loss of material from the surface of the stone, reduced stone strength, and an exacerbated negative feedback loop of stone deterioration (Goudie & Viles, 1997; Scherer, 2004; Mol & Viles, 2012;

Navarre-Sitchler et al., 2015).

1.4 Main Research Aims and Objectives

The availability of small arms and their use use within urban environments is damaging cultural heritage sites, increasing their risk to future deterioration and weathering. Within the broad spectrum of damage sustained, there is a limited understanding of the damage resulting from shrapnel and bullet impacts. To address this, a series of controlled firearm experiments were conducted to simulate small arms damage to stone constructions during conflict. The experiments used two different ammunition types, fired at two different angles of incidence, into two different sedimentary stones. These samples were then used to quantify the surface and subsurface damage through 3D photogrammetry (Chapters 3, 6, 4), scanning electron microscopy (Chapter 3), and thin section and fracture intensity analysis via optical microscopy (Chapters 3, 5). General methodologies are detailed in Chapter 2, with relevant specific details in the appropriate chapters.

This thesis aims to quantify the surface and subsurface effects of bullet impacts into sedimentary stone through the investigation and synthesis of the following research questions:

1. To what extent does observable surface damage correlate with subsurface damage?
2. Can digital documentation effectively capture damage morphology?
3. How can we efficiently measure impact damage in the field?
4. What are the subsurface effects of bullet impacts in stone?
5. What influence does impact angle, target material, and projectile type, have on surface damage morphology?

1.5 Thesis Outline

This thesis is comprised of 7 parts: The introduction above outlines how armed conflict poses a risk to heritage, summarising the current state of research into small arms and shrapnel impacts, and how alteration of stone properties influences its susceptibility to weathering deterioration. It finishes with the main research aims of this thesis. Chapter 2 outlines common methodologies used in later sections, whilst chapter specific methods are detailed in the appropriate chapters. The

following chapters address the above aims based on the original data gathered from my experiments, followed by a concluding synthesis of the results and proposals for future research.

Chapter 3 presents a pilot experiment of a bullet impact into a sandstone target. It explores and develops a methodology for quantifying surface and subsurface damage, which is used in later chapters. It uses photogrammetry to produce a 3D model of the damaged target in order to quantify the damage morphology and estimate the minimum extent of internal fractures. It combines these results with observations of surface damage from scanning electron microscopy (SEM), and subsurface damage from thin sections examined using optical microscopes, to discuss how these expressions of damage are intrinsically linked throughout the target. Finally it analyses how fracture intensity changes with increasing distance from the impact crater.

Chapter 4 follows on from Chapter 3, investigating the applicability of crater scaling relationships derived from hypervelocity experiments to the results of ordnance velocity experiments. This study compares three simplified volume geometries to the measured crater volume to propose a quick and efficient method of estimating crater volumes in the field.

With surface damage sufficiently characterised, Chapter 5 investigates the subsurface damage using thin sections examined using optical microscopy. Analysis of subsurface fracture intensity highlights the spatial distribution of fractures within the target block.

Using the methods developed in Chapter 3, Chapter 6 explores the relationship between impact trajectory and surface damage on a larger suite of experimentally generated examples of impact damage. It uses the morphology of crater profiles to distinguish between oblique and perpendicular impact trajectories, as well as the influence of projectile type and target lithology on the resultant damage.

Chapters 3, 6, and 4 are the subject of published manuscripts (Campbell et al., 2021, 2022a, 2022b), whilst Chapter 5 is derived from a submitted manuscript. Oliver Campbell wrote all chapters. Other contributions of authors are outlined at the start of each chapter.

Finally, Chapter 7 synthesises the findings of the previous chapters in the context of the research aims, as well as laying out proposals for future work.

This thesis forms part of the larger Heritage in the Crossfire (HiTC) research project (Mol et al., 2020). As part of HiTC, Oscar Gilbert is conducting a parallel PhD based at the University of the West of England. His thesis utilises some of the same materials studied here to investigate the effects of haloclasty and temperature cycles on conflict damaged stone. As a result, Oliver Campbell has co-authored additional publications with Oscar Gilbert related to the work of this thesis (Gilbert et al., 2019, 2020).

Chapter 2

Methodology

2.1 Target Materials

2.1.1 Huesca Sandstone

A cube of sandstone (14.7 × 14.7 × 14.7 cm) was quarried from the Huesca region of Northern Spain because of its analogous properties to heritage stones in the Middle East, such as the Umm Ishrin sandstones at Petra in Jordan, which have sustained historical damage (Sancho et al., 2003; Franchi et al., 2009). The Umm Ishrin is a well-sorted, medium-coarse-grained sandstone comprised of quartz grains and varying amounts of calcite and clay cement (Franchi et al., 2009). The Huesca sandstone (HS) is a well-consolidated, medium-grained sandstone with an average pore size of 40–70 µm. X-ray diffraction (XRD) analysis reveals a composition of quartz and calcite,with lithic fragments and matrix comprised of clay minerals (muscovite, kaolinite and clinochlore) (Table 2.1) (Mol & Green, 2015). Thin section observations of undamaged HS show no inherent fractures and no apparent anisotropy at the scale of the sample (Figure 2.1a).

Phase	**Percentage (%)**
Quartz	48
Gypsum	17
Calcite	13
Muscovite	13
Kaolinite	6
Clinochore	3

Table 2.1: Mineral composition of Huesca sandstone, derived from X-Ray diffraction analysis (Mol & Green, 2015).

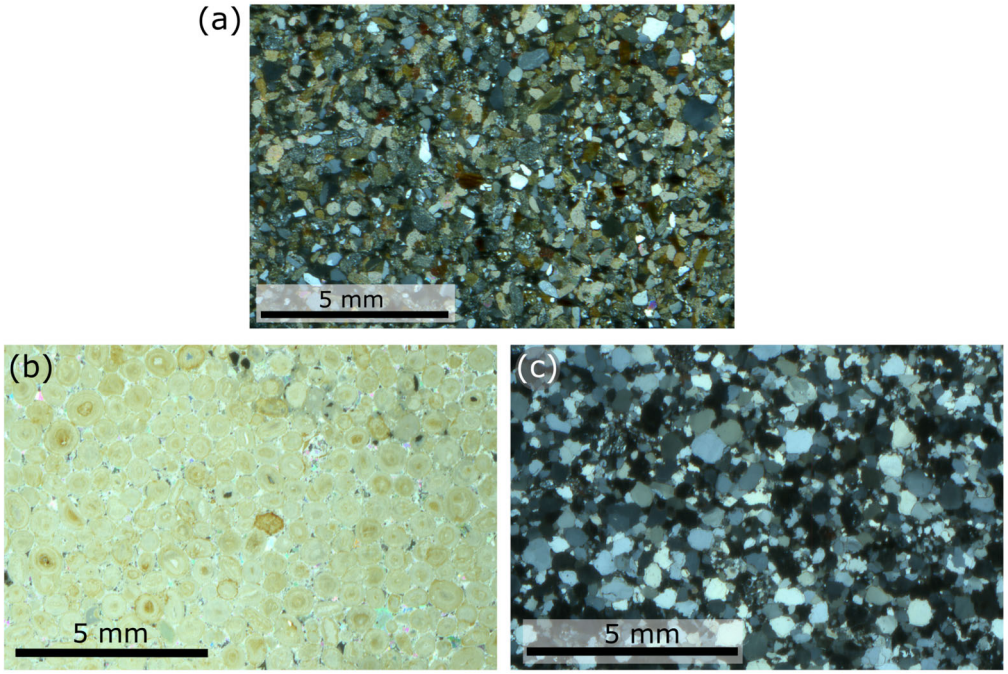

Figure 2.1: (a) Thin section photomicrograph of undamaged Huesca Sandstone under cross polarised light. It is a well consolidated, medium grained sandstone with average pore sizes of 40-70 µm. (b) Thin section photomicrograph of undamaged Cotswold Hill Cream Limestone under cross polarised light. Spherical ooids can be seen tightly packed, with most pore space filled with sparry calcite crystals. (c) Thin section photomicrograph of undamaged Stoneraise Red Sandstone under cross polarised light. Grains are predominantly quartz, with many exhibiting orange brown Fe-oxidation rims that have been subsequently overgrown.

2.1.2 Costwold Hill Cream Limestone

Freshly quarried cubes (15 × 15 × 15 cm) of Cotswold Hill Cream Limestone (CHCL) were selected as analogous to the Mokattam Limestones of Egypt, but also has common properties with other U.K origin limestones used in the construction of heritage. CHCL is an oolitic grainstone from the Middle Jurassic Inferior Oolite (quarried near Ford, U.K.). The average grain size is 0.5 mm and has a porosity of ∼20% (Figure 2.1b). It has an average block density of 2.20 $\mathrm{g\,cm^{-3}}$.

2.1.3 Stoneraise Red Sandstone

Freshly quarried cubes (15 × 15 × 15 cm) of Stoneraise Red Sandstone (SRS) were selected for controlled firearms experiments. SRS is a fine-medium (0.125-0.5 mm), quartz rich sandstone from

the Permian New Red Sandstones (quarried near Penrith, U.K) (Figure 2.1c). With a porosity of ∼11%, it generally has no internal layering, though some target blocks exhibit visible beds of coarser grains (∼1 mm). It has an average block density of 2.48 g cm^{-3}. The density of each block studied was determined by measuring the dry mass and dividing by the volume (3375 cm^3).

2.1.4 Mechanical properties

Uniaxial loading experiments were conducted to determine the uniaxial compressive strength (UCS) (ASTM D3967-16) and the indirect tensile strength (ASTM D7012-14) of SRS and CHCL targets. Cylindrical cores (20 mm diameter x 40 mm length) were drilled perpendicular and parallel to bedding. Cores were loaded at a constant rate of 0.005 mm s^{-1} using a Zwick/Roell Z050 static testing machine. The standard force, deformation, and time step were recorded using the TestXpert III software (version 1.5). The UCS (σ_u) was calculated using the equation:

$$\sigma_u = P/A_c \tag{2.1}$$

where P is the failure load and A_c is the cross sectional area of the core. Further cylindrical cores (30 mm diameter) were cut parallel to bedding, and then sliced into 15 mm thick disks for Brazilian disk tests. The prepared disks were mounted on their thin edge between flat plates and loaded perpendicular to bedding at a constant rate of 0.005 mm s^{-1}. The indirect tensile strength (σ_t) was calculated using:

$$\sigma_t = 2P/(\pi t D_d) \tag{2.2}$$

where P is the failure load, t is the thickness of the disk and D_d is the disk diameter. Linear regression was carried out on straight sections of the stress-strain curves to find the axial Young's modulus parallel and perpendicular to bedding for each stone type. The ultrapulse velocity (UPV) was measured in twelve undamaged blocks of each stone type using a Proceq Pundit 200 with 54 kHz exponential transducers (pulse voltage = 200 V, receiver gain = x1, frequency = 20 Hz). UPV was measured in each of the three orthogonal directions by placing the transducers on opposite faces. A bulk UPV value was calculated by averaging the three orthogonal directions.

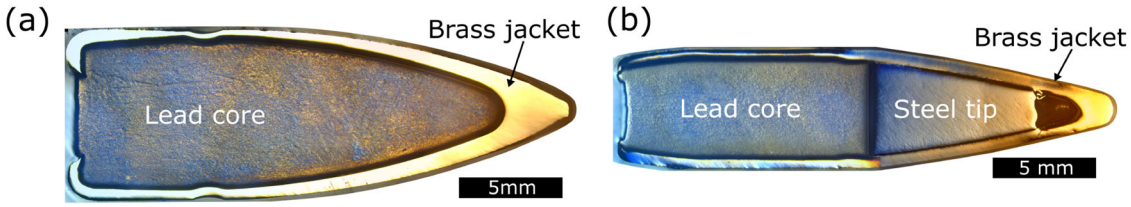

Figure 2.2: (a) Cross section of a 7.62 x 29 mm bullet head consisting of an ogival shaped brass jacket and lead core. (b) Cross section of a 5.56 × 45 mm NATO bullet head with an ogival shaped brass jacket containing a lead core and steel tip.

2.2 Controlled Impact Experiments

2.2.1 Preliminary Experiments

A block of Huesca sandstone (14.7 × 14.7 × 14.7 cm) was shot with 7.62 × 39 mm ammunition, typical of many Kalashnikov (AK) variant rifles, including the well-known AK-47 used widely in past and contemporary conflicts. It was fired from an AK-103 rifle at a range of 200 m, resulting in a velocity (v_i) of ∼540 $\mathrm{m\,s^{-1}}$ at the point of impact. The projectile is constructed from a brass jacket and lead core, with a spitzer ogive-nose shape and has a mass (m) of 7.95 g (123 grains), resulting in a kinetic energy ($K_E = 0.5mv_i{}^2$) upon impact of 1,168 J (Figure 2.2a).

2.2.2 Full Experimental Regime

Controlled firearm experiments were carried out at Cranfield Ordnance Test and Evaluation Centre (Gore Cross, UK) to simulate conflict damage to stone. This provided samples for both non-destructive and destructive testing methods. Two different ammunition types used in contemporary and past conflicts were fired from remote operated proof barrels at incident angles of 45° and 90° to the target face. 5.56 × 45 mm NATO (abbreviated henceforth as NATO) is a standardised cartridge used in the British standard issue SA80 service rifle, American M16-pattern rifles, as well as many other military issue rifles around the world. The second ammunition type is 7.62 × 39 mm (abbreviated henceforth as AK-47). Both cartridges have a spitzer ogive nosed projectile comprised of a brass jacket and lead core (Figure 2.2). The NATO projectile has an additional steel tip inside the brass jacket and a mass of 4.04 g (63 grains), whilst the AK-47 projectile has a mass of 7.95 g (123 grains).

The velocity of the projectile was measured using a Weibel SL-525P Doppler radar system operating at 0.4 W and a frequency of 10.525 GHz. The kinetic energy (E_k) of the projectile at

the point of impact was calculated using:

$$E_k = \frac{1}{2} m v_i^2 \tag{2.3}$$

where m is the projectile mass and v_i is projectile velocity at the point of impact. Test shots were conducted on an open range at standard propellant load to measure the velocity decay of each projectile, providing desired velocities for simulated engagement distances. Both cartridges were remotely fired from mounted proof barrels 14 m from the targets, with propellant loads adjusted to reduce velocity and simulate impacts at distances of 200 m (∼540 $\mathrm{m\,s^{-1}}$ for AK-47 and ∼700 $\mathrm{m\,s^{-1}}$ for NATO projectiles). Average engagement distances of urban firefights during the Iraq War ranged from 26 m to over 126 m between combatants, and most soldiers are trained for engagement distances of 0 – 600 m, so 200 m represents a reasonable distance for simulating impacts in both urban and open scenarios (Fitzsimmons, 2015; MOD-UK, 2018). Additional adjustments were made to the AK-47 and NATO cartridges to simulate a range of 400 m (∼430 $\mathrm{m\,s^{-1}}$ and ∼600 $\mathrm{m\,s^{-1}}$ respectively), as well as one shot conducted at standard propellant load (impact at muzzle velocities of ∼730 $\mathrm{m\,s^{-1}}$ and ∼930 $\mathrm{m\,s^{-1}}$ respectively). The kinetic energy of the projectile at impact will be in the range 734–2118 J for the AK-47 projectile and 727-1747 J for the NATO projectile. Concrete blocks were placed on all faces, except the target face, for confinement. Target blocks with visible bedding were oriented so that foliations were parallel to the target face. Natural stone is typically strongest when loaded perpendicular to bedding, and a consistent orientation relative to the target face means any influence of internal bedding will be consistent across experiments.

2.3 Quantifying Damage Morphology

2.3.1 Reference Scheme

A 3D coordinate scheme adapted from Tikoff et al. (2019) was implemented to retain the spatial position of observations and measurements. The target face of the sample is the XY plane and the Z axis is orthogonal to this and negative into the block. The crater centre is used as the reference point for all distance measurements and is defined as the point on the current crater floor that is directly below the point of impact.

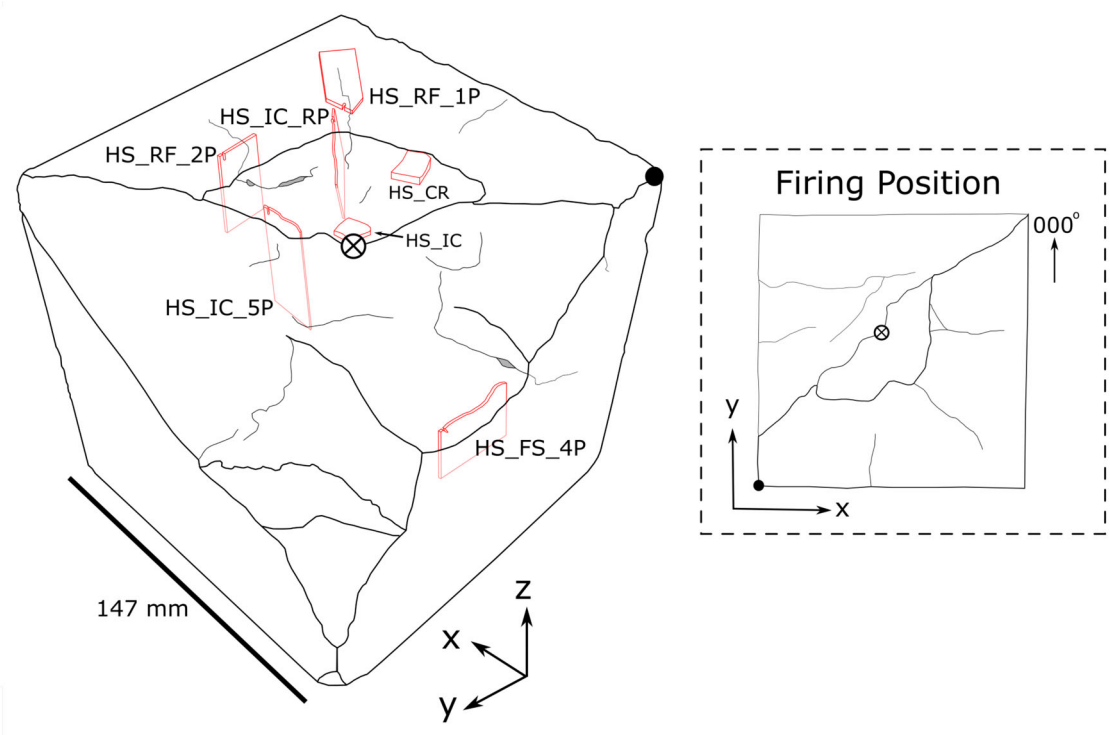

Figure 2.3: Schematic of Huesca Sandstone target block showing the location of thin sections and scanning election microscope (SEM) stubs. Black circle indicates the reference corner (adapted from Tikoff et al., 2019). Inset shows block in its firing position, with the XY plane as the target face and an azimuth of 000° assigned to the positive Y direction.

2.3.2 Photogrammetry

A 14-megapixel Fujifilm Finepix S3400 digital camera was used to photograph samples through a 360° rotation at three overlapping camera positions. Samples were then overturned and the process repeated. The camera was fixed on a tripod ∼1 m from the sample and its optical zoom (equivalent focal lengths 24-672 mm) used to ensure sufficient detail was captured. Additional images were taken of the damaged surface to ensure adequate capture of the morphology. Images were imported into Meshroom (version 2020.1.1), a free and open-source structure from motion (SfM) pipeline developed by AliceVision®(Jancosek & Pajdla, 2011; Moulon et al., 2012). The resulting 3D meshes were scaled and oriented in 3D space using CloudCompare (version 2.11.3), with the target face horizontal and an azimuth direction of 000° directed towards the top edge of the target face in it's firing position.

2.3.3 Surface Facets and Fractures

The FACETS plugin for CloudCompare (CloudCompare, 2020) was used to summarise the morphology of impact damage to the Huesca Sandstone during preliminary tests. A Kd-tree algorithm was selected to summarise the model because of its faster processing time and better representation of geometry than the alternative fast-marching algorithm. The following Kd-tree settings were applied: max angular difference = 5°, max relative distance = 1.00, max distance at 99% = 0.2, min points per facet = 10, and max edge length = 0.30. These settings represent the damage adequately and within workable processing time frames (minutes vs hours). A smaller angular difference would have represented the morphology with a greater number of facets and complexity, but the increased processing time and larger data set had a negligible influence on the clustering observed in the stereonet. Facets representing undamaged areas of the block were manually removed.

The Compass plugin was used to digitise surface fracture traces and measure their orientations (Thiele et al., 2017). The 3D mesh and digitised fractures were then imported into Blender (version 2.92.0) to estimate the minimum internal surface area of the fractures. In order to compare these values with the areas of damage at the surface, the scaled and oriented model was imported into Meshlab where the area of exposed fracture surfaces was calculated (Cignoni et al., 2008; Ranzuglia et al., 2013). The volume of material removed from the damaged block was also calculated in Meshlab. Fracture planes from manual tracing (n = 24) and facet extraction (n = 674) are presented on standard equal area lower hemisphere projections. Facet data was contoured using a modified Kamb contour method with exponential smoothing (Kamb, 1959; Vollmer, 1995). The Kamb contour method was chosen over alternatives, such as the 1% area, because it is independent of sample size.

2.3.4 Crater Morphology

Crater volumes were calculated from photogrammetry models of damaged SRS and CHCL target blocks in CloudCompare , while depth maps and cross section profiles were extracted in Python (version 3.8.11). Crater outlines were digitised from plan view photographs in QGIS (version 3.16.0). The edge of the crater was defined visually as the transition from a depression, not including open radial fractures, to undamaged target face. Outlines were analysed in ImageJ (version 1.53) to measure various shape parameters, such as crater area (A), which was then used

to calculate an area equivalent diameter (D_{eq}) using:

$$D_{eq} = 2\sqrt{A/\pi} \tag{2.4}$$

Cross section profiles, centered on the deepest point of the crater, were measured at 10° intervals and averaged to obtain a mean crater profile. The capture of digital imagery may not be possible in all situations, so crater profiles were measured using an analogue Barton comb method. A 150 mm Barton comb was inserted into the crater and teeth adjusted to fit the crater profile. Four profiles were taken at 45° intervals, starting at 000°, to be compared to profiles from the digital model taken in the same orientation (Figure 2.4a). The photographed comb profile was digitised in QGIS. The Root Mean-Square (RMS) difference between the comb profile (P_c) and digital profile (P_d) was calculated using Equation 2.5.

$$RMS_{difference} = \sqrt{\frac{\sum_{i=1}^{n}(P_c i - P_d i)^2}{n}} \tag{2.5}$$

The RMS difference for each sample was normalised (RMS_N) to the maximum profile depth (d_{max}), as measured by the comb profile, to enable comparison between samples:

$$RMS_N = \frac{RMS_{difference}}{d_{max}} \tag{2.6}$$

Crater volumes measured from the digital models were compared to the volumes of three simplified geometries (see Table 2.2) derived from just crater depth (d) and radius ($r = 0.5D_{eq}$) measurements. The simplified geometries selected have previously been used to describe crater geometries in hypervelocity experiments: simple cone (Hörz, 1969; Kenkmann et al., 2011; Dufresne et al., 2013), spherical cap (Güttler et al., 2012), and a parabaloid, typically representing the transient crater (Kenkmann et al., 2011).

Geometry	**Volume Equation**
Simple Cone	$V = \frac{1}{3}\pi r^2 d$
Spherical Cap	$V = \frac{1}{6}\pi d(3r^2 + d)$
Paraboloid	$V = \frac{1}{2}\pi r^2 d$

Table 2.2: Simplified crater geometries and volume equations. $r = 0.5D_{eq}$ and d=crater depth.

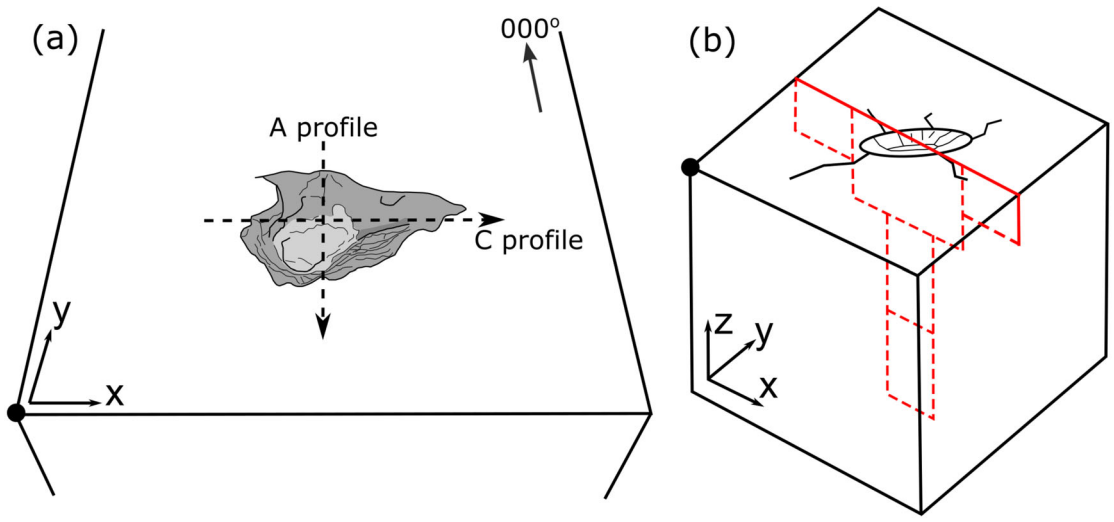

Figure 2.4: (a) Schematic of damaged target face showing the orientation of two Barton comb profiles. (b) Schematic of thin section locations cut through the impact crater parallel to the XZ plane. Black circle represents the reference corner of the 3D coordinate scheme adapted from Tikoff et al. (2019).

2.3.5 Microscale Damage

Huesca Sandstone

Two stubs (~10 × 10 mm) were cut from the impact crater of the HS block and coated with a 30 nm thick Au-Pd coating for use in a scanning electron microscope (SEM). Backscatter electron (BSE) images were obtained using an FEI Quanta FEG 650 with an Oxford Instruments Xmax^n EDS detector. Images were captured at pressure with a spot size of 5.0, a working voltage of 5.00 kV, and a working distance of 8.5 - 11.6 mm. Thin sections (28 × 48 mm) were cut from different regions of the damaged HS block, with section planes oriented perpendicular to visible fractures (Figure 2.3). Thin sections were scanned using an Epson Perfection 3170 photo scanner at 6400 dpi under plane and cross polarised light. Fractures were digitised in QGIS (version 3.16.0) as a single polyline to preserve fracture geometry and characteristics.

Stoneraise Red Sandstone and Cotswold Hill Cream Limestone

For the damaged SRS and CHCL target blocks, polished thin sections (a combination of 75 × 50 mm and 28 × 48 mm) were cut through the centre of the impact crater parallel to the XZ plane (Figure 2.4b). Thin sections were scanned using an Epson Perfection 3170 photo scanner at

6400 dpi under plane and cross polarised light. Reflected light photo micrographs of each section were taken at 1x magnification using a Leica DM750P optical microscope fitted with a MC190HD camera. Microsoft ICE (Image Composite Editor)(version 2.0.3.0) was used to create a photo-mosaic of full sections. Complete photo-mosaics and thin section scans were georeferenced and fractures manually digitised in QGIS. Closed fractures were digitised as a single polyline and open fractures as a polygon. The fracture map was thresholded into a binary image and NetworkGT's (a QGIS plugin) automatic fracture digitisation tool used to generate a fracture network of polylines for analysis. This automatic digitisation approach ensures a consistent interpretation of fracture geometries and fracture characteristics across samples.

Fracture Analysis

Important characteristics of fracture networks, such as length and orientation, can differ between interpretations conducted by different investigators (Sanderson & Nixon, 2015; Andrews et al., 2019). Analysing fracture branches instead of full traces reduces this bias, as well as mitigating any censoring effects of the sample region because the intersection with the edge now only affects a single branch, instead of the full fracture trace (Sanderson & Nixon, 2015). The NetworkGT plugin for QGIS was used to calculate P_{xy} values for each thin section (Nyberg et al., 2018). P_{xy} values characterise fracture frequencies, intensities, and volumes, where x represents the dimension of the sampling region and y is the dimension of measurement (Dershowitz & Einstein, 1988; Dershowitz & Herda, 1992). For example, P_{21} is a measure of fracture length (L) per section area (A_s):

$$P_{21} = \sum L/A_s \tag{2.7}$$

Dimensionless intensity values are those where the dimension of measurement and sampling are the same (e.g., P_{22}) (Sanderson & Nixon, 2015). P_{22} values are calculated by the equation:

$$P_{22} = P_{21} \cdot L_c \tag{2.8}$$

where L_c is the characteristic length, defined simply as the arithmetic mean of branch lengths (Sanderson & Nixon, 2015).

P_{xy} values were calculated using the digitised fracture maps and QGIS's NetworkGT plugin. For all samples, the centre of the crater is used as the reference location from which intra-sample distances are measured from. For HS sections, topology parameters (inc. P_{xy} values) were cal-

culated using the NetworkGT plugin for each full thin section. The calculated value was then assigned to the mid point of the section and its distance to the crater centre measured. For SRS and CHCL thin sections, a grid sampling for the calculation of topology parameters was undertaken. A sample grid (spacing = 0.25 mm, sampling radius 0.75 mm) was constrained to section outlines (excluding areas lost to sectioning) and a distance to the crater centre for each grid point obtained. The orientation of fractures was weighted for fracture length and displayed on equal area rose diagrams.

Uncertainty Calculation

Uncertainty in the distance from the crater centre measurements for all targets is estimated to be ± 2 mm, based on the contribution of several factors: (i) The measurement of section locations during the cutting process. (ii) The possible loss of material at the edges of thin sections during production, though every effort was made to minimise this. (iii) The scaling of the 3D model (for the HS target). (iv) The measurement of points on the 3D model (for the HS target). (v) Geo-referencing of thin sections and photo mosaics. The digitisation in QGIS was the primary source of uncertainties in the calculation of fracture intensities. The thin section scans used for digitisation are limited in their resolution, despite a very high resolution of scanning (6400 dpi). Fracture apertures narrow to the point they become indistinguishable from adjacent grain boundaries (pixelation distance). In this situation, fracture trace was terminated if there was no distinguishable aperture when it reached grain boundaries, or there was no clear continuation of the fracture beyond that grain. For the lateral placement of polylines in the HS thin sections, important in determining the sample area, this uncertainty was individually estimated for each section, with values between 0.029 and 0.033 mm. The perimeter of the measured sample area was then expanded and contracted by these uncertainties to determine the maximum and minimum sample areas respectively. A fracture length uncertainty for HS sections of 0.1 mm was deemed appropriate as it is approximately 3 - 4 times the measured pixelation distances at boundary locations, so represents an average combined uncertainty where multiple grains are in contact. A minimum and maximum fracture trace network for HS sections was calculated by decreasing and increasing the length at all isolated tips ('I' nodes) by this uncertainty. The maximum P_{21} and P_{22} values were calculated using the minimum sample area and maximum trace length map. Minimum P_{21} and P_{22} were calculated using the maximum area and minimum fracture trace length map. Another source of uncertainty in mapping fracture intensities with distance from the crater is that one value represents a 2D area, covering a range of distances from the crater centre. The range

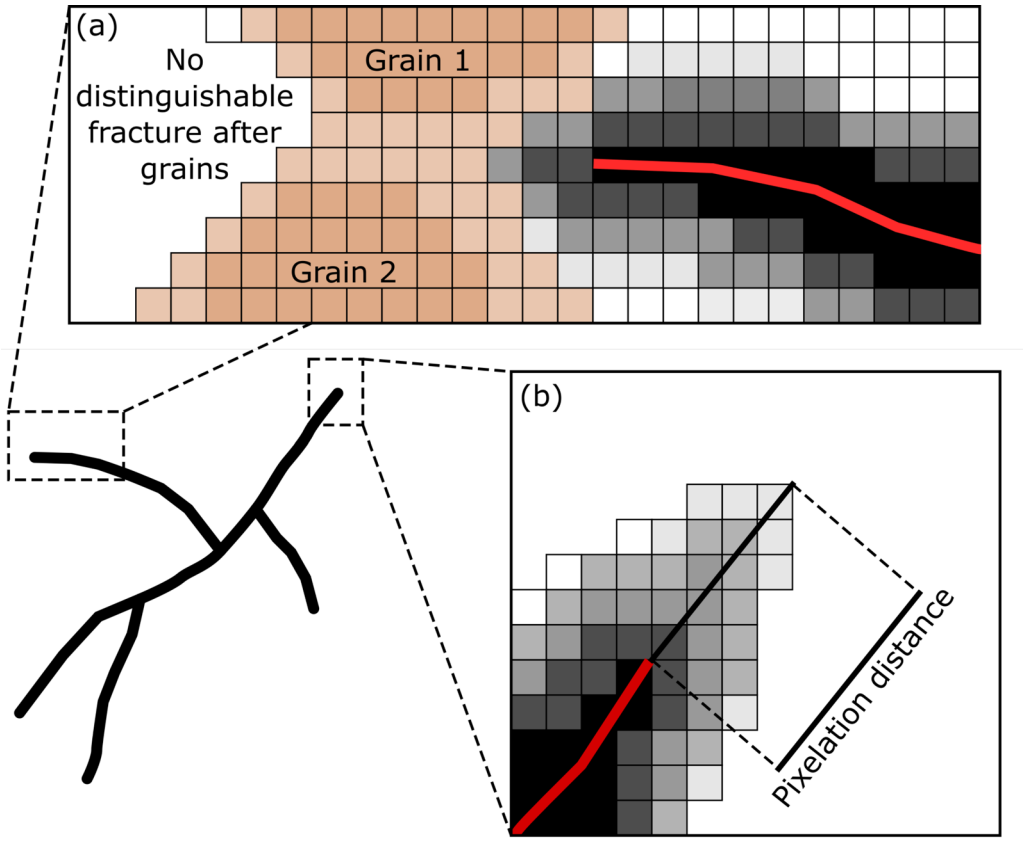

Figure 2.5: (a) Diagram showing how fracture traces were terminated when there was no distinguishable fracture aperture after it reached grain boundaries. (b) Diagram showing how fracture tips ('I' nodes) have a range of pixels instead of a sharp boundary. Fractures were digitised conservatively, terminating at the last pixel identifiable as the fracture (red line). The pixelation distance was measured for each section and used as the uncertainty when calculating fracture topology parameters.

of distances that a section covers depends on its orientation relative to the impact. Thin section planes that are roughly concentric to the crater centre have a smaller range of distances (∼8 mm) than those oriented radially (up to 50 mm).

SRS and CHCL fracture maps were digitised conservatively, i.e. fractures were plotted to the last pixel identifiable as part of the fracture, resulting in a minimum extent fracture map. The fracture length uncertainty for each sample was measured: 0.031 mm for SRS sections and 0.026 mm for CHCL sections. 'I' nodes were extended by this uncertainty and new topology parameters calculated using the same sample grid spacing and sample radius.

Chapter 3

Damage Caused by Bullet Impacts into Sandstone

3.1 Abstract

The shift of armed conflicts to more urbanised environments has increased the risk to cultural heritage sites. Small arms impacts are ubiquitous in these circumstances, yet the effects and mechanisms of damage caused are not well known. A sandstone target was shot under controlled conditions to investigate surface and subsurface damage caused by bullet impacts. A 3D model of the damaged block, created by structure from motion photogrammetry, shows that internal fracturing was at least as extensive as the visible surface fractures. Backscatter electron imaging of the damaged surface shows a shift from intragranular fracturing and grain size reduction at $<$ 5 mm from the impact point to primarily circumgranular fracturing and grain 'plucking' at 20 mm from the impact point. Internal fracture intensity decreased with distance from the centre of the crater. Volumes around the impact point are therefore at greater risk of subsequent weathering deterioration, but significant damage extends to the periphery of the target, rendering whole blocks vulnerable. The surface crater, despite being one of the most conspicuous aspects of conflict damage, has many times less area than internal and surface fractures.

Author Contributions

This chapter is based on a published manuscript: Campbell, O., Blenkinsop, T., Gilbert, O. and Mol, L. (2021). Surface and Subsurface Damage Caused by Bullet Impacts into Sandstone. *Geosciences*, 11, 395. https://doi.org/10.3390/ geosciences11090395

Oliver Campbell is the main author of this work and undertook the creation of the photogrammetry model, characterisation of morphology, microstructural fracture analysis, and wrote the manuscript. Lisa Mol organised the controlled firearms experiments. Tom Blenkinsop and Lisa Mol provided supervision during the writing of the manuscript. Oliver Campbell and Oscar Gilbert performed the Scanning Electron Microscopy. Three anonymous colleagues provided feedback on early drafts of the manuscript, and two anonymous reviewers provided constructive reviews that improved it further.

3.2 Introduction

In situ measurement of stone properties are highly desirable for heritage conservation efforts but is generally restricted to non-destructive testing (Pope et al., 2002; Jo & Lee, 2011; Allen et al., 2018; Hatır et al., 2021). Impacts cause compaction and grain size reduction near the point of contact and increased surface permeability, suggesting greater susceptibility to the ingress of weathering agents such as moisture and salt (Mol & Gomez-Heras, 2018; Gilbert et al., 2019, 2020). The development of fracture networks increases the depth within the stone to which weathering processes can extend, expanding the region at risk of deterioration (Lebedeva & Brantley, 2017). Measurement of such effects is vital in assessing portions of heritage at the highest risk of further deterioration. Field instruments such as surface hardness probes, permeameters, ultrapulse velocity meters, moisture probes, and infra-red scanners can provide valuable information on stone conditions, but the non-destructive nature of these methods precludes direct observation of subsurface damage, for which alternative methods are required.

This chapter therefore presents a pilot experiment conducted to simulate conflict damage to stone buildings. It begins to address a gap in the literature, of which there is little in the way of quantitative studies using bullets and natural stone under conditions comparable to conflict situations. It furthers advances the work of Gilbert et al. (2019) by characterising the surface morphology of impact damage and quantifying macro-scale fracture networks using 3D models generated by photogrammetry. It describes the microscale surface damage within the crater using scanning electron microscopy and highlights links to subsurface damage observed through thin section microscopy and fracture intensity analysis.

3.3 Methods Summary

To avoid repetition, only a brief summary of methods is presented here (full details and description is available in Chapter 2). A cube of Huesca sandstone (14.7 × 14.7 × 14.7 cm) was shot with 7.62 × 39 mm ammunition to simulate damage to stone heritage in a conflict situation. A 3D model of the damaged target block was generated using one hundred and forty-two images (142No.) in Meshroom and FACET analysis was conducted in CloudCompare. A series of stubs and thin sections were produced for microscale analysis using scanning electron (SEM) and optical microscopy techniques.

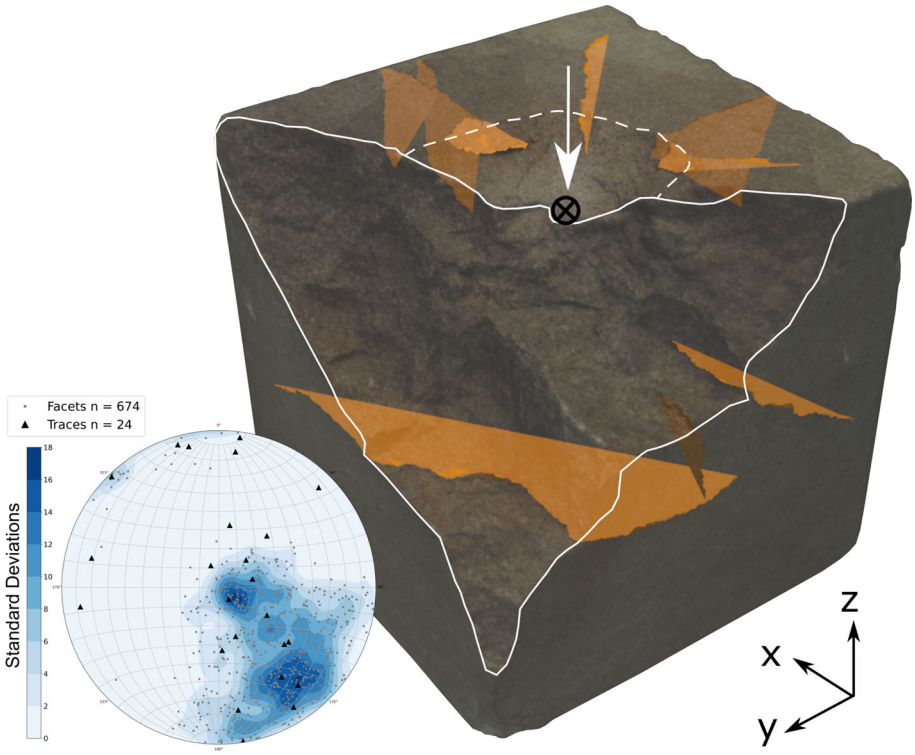

Figure 3.1: Summary of data measured from the 3D model of Huesca sandstone shot with 7.62 × 39 mm ammunition. A rendering of the block is visible with the minimum extent of internal fracturing estimated from surface traces shown in orange. Note the large fracture just below the centre of the model that is sub-parallel to the target face. The stepped damage region is outlined by a solid white line, and the impact crater by a dashed white line. The white arrow shows the bullet trajectory and black crossed circle marks the crater centre. (inset) A lower hemisphere equal area projection of the poles to fracture planes estimated from surface traces (black triangles), and the orientation of facets (grey circles) representing the stepped morphology of the damage surface. Facet orientation data is contoured in blue using a modified Kamb contour, indicating two distinct clusters of orientations: A steep NW dipping set and sub-horizontal set.

3.4 Results

Surface damage from the impact consists of a shallow, bowl-shaped impact crater which is truncated by material loss along a stepped surface from one corner of the block. The loss of material is substantial: 3.812×10^5 mm^3, ~12 % of the block's initial volume (outlined in Figure 3.1). Surface fracture traces with macroscopic apertures are present on the remaining stone, with radially oriented traces centred on the crater, and traces sub-parallel to the target face (XY plane) up to 80 mm from the crater centre (Figure 3.1). Most radial fractures intersect the edge of the

block and are visible on adjacent sides. The damaged surface, excluding the crater, has a stepped morphology with distinct steeply and gently dipping surfaces (Figures 3.1c and 3.1). The facet data shows two distinct orientations, one dipping steeply towards (X_{min}, Y_{max}) and the other sub-parallel to the XY plane. The degree of clustering of poles to fractures ranges from 10 σ to 18 σ, where σ is the number of standard deviations from sampling a random distribution.

The impact resulted in a shallow, bowl-shaped crater directly below the impact (Figure 3.1). The crater has a deep central pit surrounded by a shallow dipping region separated by a change of slope. The floor of the crater has a lighter colouration than surrounding damage as a result of the comminuted material and grain fracturing. Back-Scatter Electron (BSE) imaging from within 5 mm of the crater centre display fractures going through and around grains, conchoidal quartz fracture surfaces, and comminuted material (Figure 3.2). The fractures observed can be seen penetrating the stone surface, where they have apertures < 20 µm. Around 20 mm from the crater centre, circumgranular, and to a lesser extent intragranular, fracturing is visible within the shallower spall zone. The majority of fracturing is however circumgranular, separating grains from the clay matrix and leading to distinct oval-shaped depressions where grains have been 'plucked' from the surface (Figure 3.2b). Some fractures visible in BSE images cut across clay minerals at a high angle to mineral cleavage, similarly observed in thin sections from below the surface (Figures 3.2bii and 3.3i).

Radial fractures appear as a single trace at the macro scale (e.g. HS_RF_1P), but at the microscale are multiple shorter branches that overlap or join together (Figure 3.3). Aperture varies along the fracture length, narrowing at the fracture tips and overlap zones, and widening in the middle. Fracture paths are both circum- and intragranular. Sections close to the impact crater have open, curved fractures sub-parallel to the crater floor, linked by occasional short fractures with an approximately radial orientation. Fracture paths are again indiscriminately both within grains and along grain-matrix boundaries. Fracture mode changes with increasing distance from the crater centre. As distance increases, fracture networks tend towards circumgranular paths and intragranular fractures are less common, particularly those traversing quartz grains.

Quantification of the fracture networks suggests that fracture intensity (P_{21} and P_{22}) decreases linearly with increasing distance from the crater centre (Figure 3.4). The P_{21} value of sample HS_RF_1P appears to differ from this trend and has a lower value (0.117 vs 0.193) than sample HS_FS_4P which is 25 ($\pm$2) mm further from the crater. With the exception of HS_RF_2P, the characteristic branch length of samples (L_c) is approximately 1 mm (Figure 3.4). The impact has generated a combined 312,980 mm^2 of new internal and external surface area. The minimum

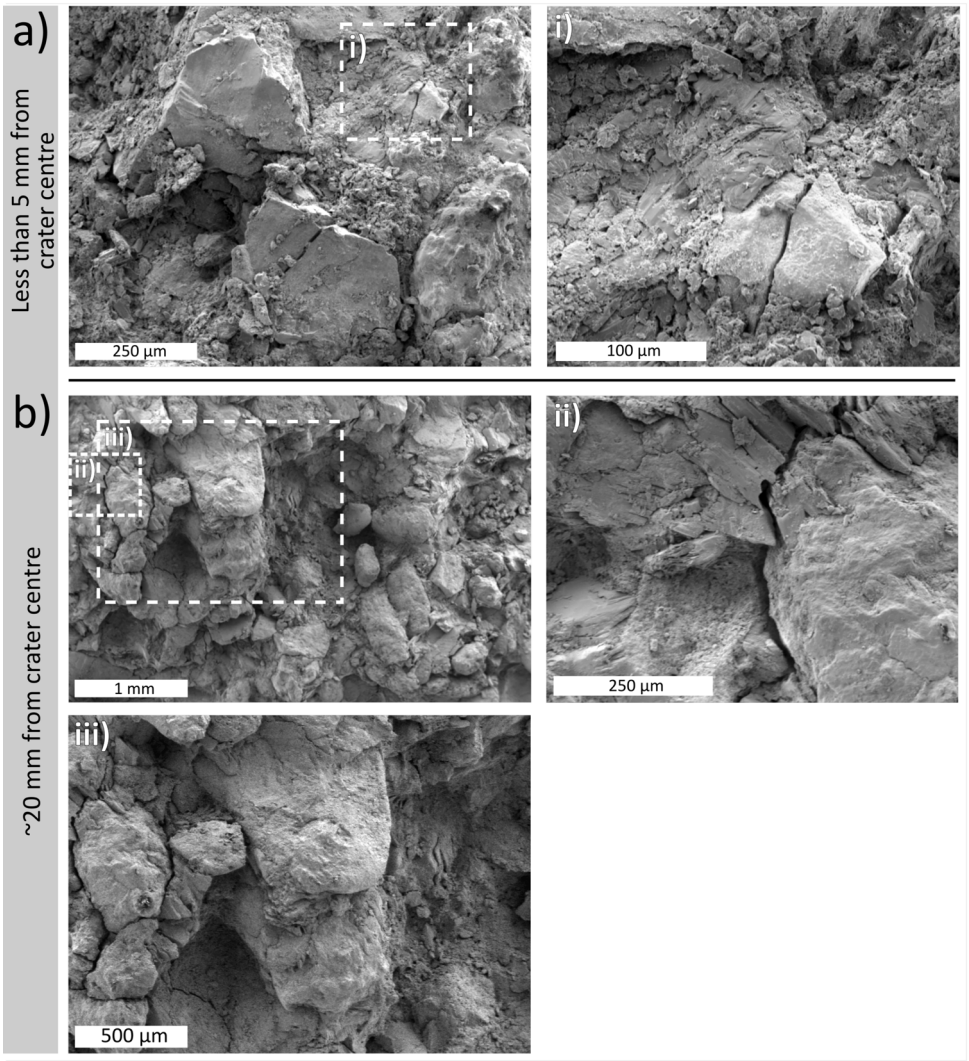

Figure 3.2: Backscatter electron (BSE) image of surface damage within the impact crater. (a) HS_IC is sampling the crater centre, showing heavily comminuted material, conchoidal fracture surfaces on quartz grains, and intragranular fracture paths (i). (b) Sample HS_CR from the spall zone of the impact crater shows grain plucking, less comminution, fracturing of clay minerals at a high angle to cleavage (ii), and a larger proportion of fractures having circumgranular paths around grains (iii).

estimate of the internal area is half that of external fracture surfaces (Table 3.1). The impact crater comprises a relatively small proportion of the overall induced damage, with the majority of the newly generated surface area related to internal and external fracturing, with a minimum estimate of 0.110 for P_{32} intensity.

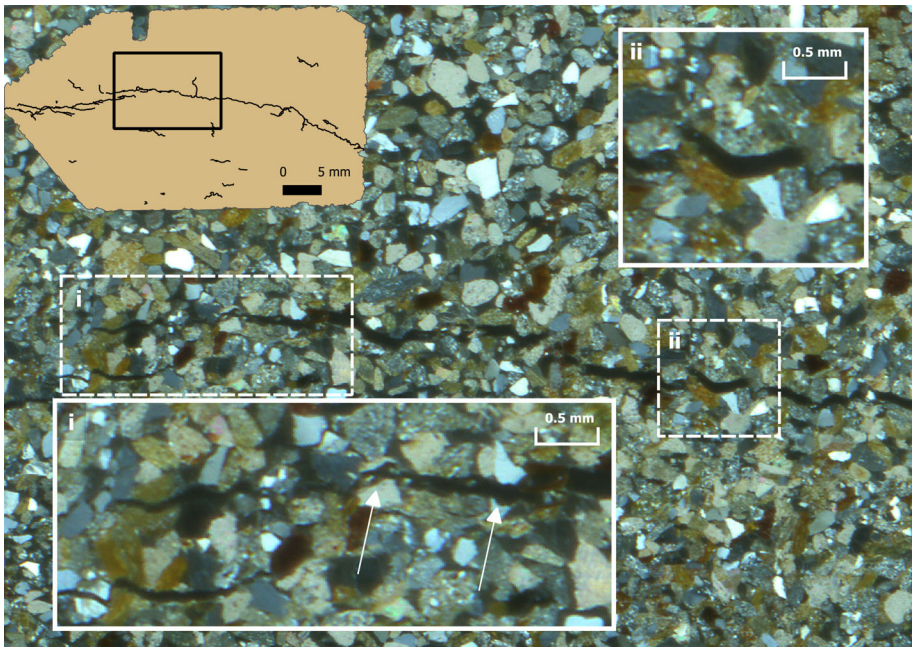

Figure 3.3: Thin section micrograph under cross polarised light of sample HS_RF_1P showing the path of radially oriented fracture. The fracture path is both circum- and intragranular as seen in inset (i) and (ii) respectively. White arrows indicate intragranular fracturing. Note the fractures cutting across clay minerals at a high angle to cleavage in the lower left of (i), as well as the zone of overlap between the shorter fracture strands that make up the macro-scale radial fracture.

Region	**Area** (mm^2)
External of damaged block includes:	122,510
- Impact Crater	2,520
- Stepped Region	17,850
Internal fractures (min. estimate)	10,470
Total surface area (min. estimate)	132,980

Table 3.1: Surface area measurements obtained from the 3D model of the damaged Huesca Sandstone.

3.5 Discussion

The surface damage represented by the impact crater and stepped region is linked to a network of subsurface fractures, which consists of circum- and intragranular fracture paths of varying aper-

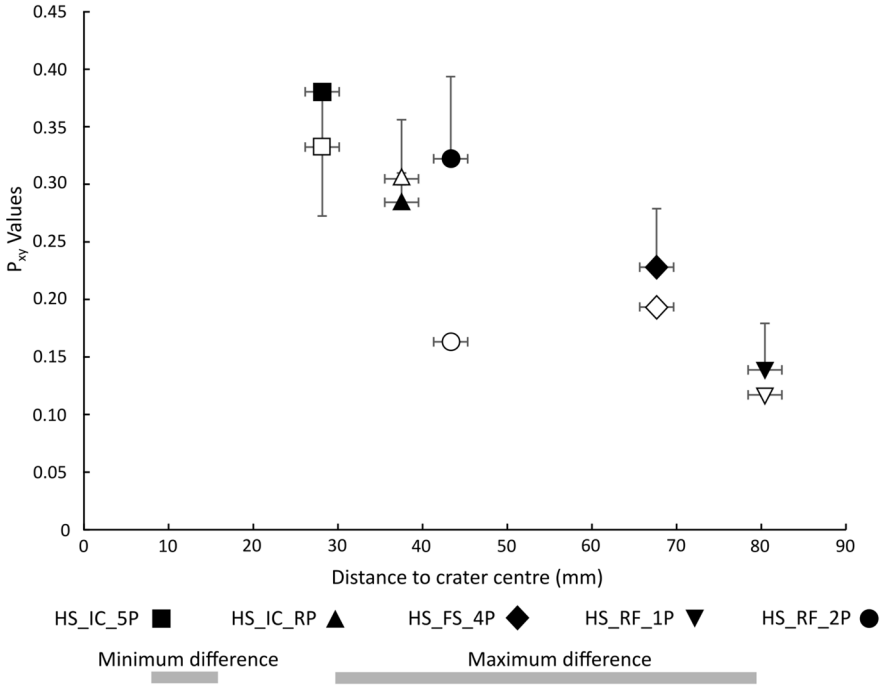

Figure 3.4: Graph showing the decrease in P_{21} (hollow symbols) and P_{22} (filled symbols) values with distance from the point of impact. The minimum and maximum differences show how much distance a section can represent in a single value.

tures that decay in intensity with increasing distance from the crater centre. Surface observations within the impact crater and spall zone show a shift of fracturing towards circumgranular pathways with increased distance from the impact, which is also seen throughout the subsurface sections and reflected in the fracture intensity plots. The micro-fractures provide evidence to support Gilbert et al.'s (2019) suggestion that increased permeability and decreased surface hardness associated with the impact crater is related to micro-fracturing, as well as mirroring observations of grain fracture proximal to impact by Mol et al. (2017). Gilbert et al. (2019) observed a light powdery appearance on the crater floor and a smaller surface hardness reduction relative to other areas of the impact damage. This is indicative of grain crushing and compaction directly below the impact, an observation made in hypervelocity impact experiments and supported by this study's SEM observations of fractured grains and comminuted material. Zones of pervasive fracturing and crushing are evidenced as impact breccia beneath natural craters (Kumar, 2005) and as heavily comminuted grains in experimental samples (Polanskey & Ahrens, 1990; Buhl, Poelchau, et al., 2013). Further similarities to hypervelocity experiments are the bowl-shaped crater, the shallow

surrounding spall zone, and the penetrative radial fractures (Lange et al., 1984; Polanskey & Ahrens, 1990; Buhl, Kowitz, et al., 2013). Greater fracture intensity values closer to the crater centre, and direct observation of surface and subsurface fractures support observations of a decreasing degree of grain size reduction with distance from the impact by Buhl et al. (2013). The irregular fracture paths present across grains and along grain boundaries are similar to dynamic fractures where propagation stabilises at high velocities, resulting in rough and irregular fracture surfaces (Ravi-Chandar, 1998; Buhl, Kowitz, et al., 2013).

During the dynamic fracture caused by impacts, higher strain rates tend to result in higher fracture intensity, as more flaws are required to fail in order to accommodate the high strain rate (Lawn, 1993). Buhl et al. (2013) measured axial strain, and the axial strain rate, below hypervelocity impacts in sandstone where they observed a very high strain rate directly beneath the impact, which rapidly decayed within 4-5 projectile diameters (∼8 mm in their study). For this study, 4-5 projectile diameter would equate to a distance of 30-38 mm (using the widest diameter of the projectile). Because stubs were removed from the crater centre, fracture analysis could not be performed closer than 28 mm from the crater centre, so these results may only represent a small portion of the sample that experienced the highest strain. As such, inferences of damage directly below the impact are drawn with care. However, direct observation of grain comminution and micro-fracturing on the surface suggest that fracture intensities may be higher in this region, especially when taken together with the clear relationship between fracture intensity and distance from the crater centre. The decrease in fracture intensity values with distance is similar to the decay in strain rate observed beyond 8 mm by Buhl et al. (2013).

Fractures are an important control of the mechanical properties of masonry and the long term susceptibility of heritage to weathering. They provide new pathways for moisture ingress, and their influence on stone properties (surface area, porosity and pore size distribution, compressive strength, and modulus of compressibility) facilitates further deterioration through salt crystallisation and frost cycles, potentially resulting in the loss of large fragments of material (Theoulakis & Moropoulou, 1997; McCabe et al., 2010). This link between fracture damage and deterioration was explored further by Lebedeva and Brantley (2017), who found weathering fronts advanced faster in stone with smaller fracture spacing (greater intensities). This would suggest that regions proximal to the impact may experience the fastest advance of weathering deterioration, and should therefore have a higher priority in terms of conservation strategies.

Structure from Motion (SfM) is a relatively quick and easy field method for capturing morphology without imposing additional deterioration or damage. SfM requires minimal investment,

needing only a digital camera and computer, whereas other methods of 3D model generation such as terrestrial laser or structure from light scanning may require specialist equipment and proprietary software. SfM has been useful in cataloguing heritage as a whole, and SfM from drone-based cameras has proven archaeological applications, including the study of inaccessible sites such as high walls (Fernández-Hernandez et al., 2015). The quality of SfM models produced in this study was sufficient to characterise impact damage morphology and quantify fracture areas. The estimation of internal fracture area relies on fracture traces being present across changing relief on the model (e.g. on different sides of the block). Limited relief, e.g. when fragments are held in place by adjacent blocks, or where visual observation of block sides is obscured, will result in underestimates of fracture surface area. However, models still provide valuable information for conservation work with regard to fracture orientations and length. Radial fractures are observed reaching the edge of the block, and can travel along mortar bonds and destabilise larger sections of masonry beyond the impacted block (Tolch & Bushkovitch, 1947).

The size and shape of the target block appears to influence the resultant damage. The initial compressive stress wave at impact can reflect from free surfaces as a tensile wave of equal magnitude, which can interact with the secondary tensile stress wave and lead to tensile stresses exceeding the target's strength (Melosh, 1984). The magnitude of the stress waves is proportional to the distance from impact, so greater distances to a free surface (i.e. a larger target) will result in lower maximum stresses during the interaction of stress waves. The lower ratio of projectile size to target dimensions in this experiment compared to hypervelocity experiments (Polanskey & Ahrens, 1990; Kenkmann et al., 2018) may explain why a relatively larger proportion (12%) of the volume loss. Mol and Gomez Heras (2018) observed greater impact damage to the detailing on stone statues where the distance from the impact point to a free surface was relatively small.

Even within the same calibre, ammunition can be highly variable, depending on its purpose (e.g. armour piercing), which affects characteristics such as shape (e.g. spitzer, round nose, hollow point), and composition. These variables influence the damage caused by impact. Hypervelocity experiments (Poelchau et al., 2013) suggest that variables resulting in greater kinetic energy lead to larger crater volumes. The angle of impact also influences the amount of kinetic energy transferred to the target, and where peak pressures are experienced. Pierazzo and Melosh (Pierazzo & Melosh, 2000b) showed that shallower angles of impact generate peak pressures further down trajectory and closer to the surface than perpendicular impacts. The likelihood of perpendicular impacts in a conflict scenario is small, and conclusions drawn in this study may need modification to deal with oblique impacts, for which the impacts described here are a baseline in ongoing investigations.

Microscale observations through SEM and thin section samples have demonstrated a link between damage visible on the surface and damage within the subsurface. Thin sections enable the relationship between subsurface fracturing and the impact to be quantified, supporting previous suggestions and observations that damage is greater closer to the impact point (Buhl, Kowitz, et al., 2013; Mol & Gomez-Heras, 2018; Gilbert et al., 2019). The negative trend of P_{xy} values with distance from the crater centre suggest negligible fracture intensities 115-120 mm from the crater centre, approximately 80% of the block's dimensions. Further experiments are needed to investigate if this value is a constant.

3.6 Conclusions

This study has shown that an experimental impact into natural stone results in substantial material loss from cratering and from the expansion of a macro-scale fracture network intersecting the edge of the target block. The stepped surface of the fracture network has two distinct orientations: one sub-parallel to the target face and the other steeply inclined towards one corner. The crater is surrounded by penetrative radial fractures that reach adjacent sides, and fractures parallel to the target face up to 80 mm from the crater floor. The total crater area is substantially less than that of the stepped region, and indeed of the internal fractures. Surface cratering, which is commonly the most apparent feature of conflict damage, may not be the most important expression of damage, with fractures accounting for ∼4-7 times as much damage by area.

On the micro scale, open aperture and grain boundary fractures are visible in thin sections on both the surface and within the target block. Directly below the crater floor sub-parallel open aperture fractures traverse grains and grain boundaries, transitioning to fractures primarily along grain boundaries with increasing distance from the crater floor. Fracture intensities measured from the sections show a decrease from $P_{21} = 0.33$ close to the impact to $P_{21} = 0.12$ further away, with values that become negligible towards the margins of the block. Subsequent weathering poses a greater risk to regions proximal to the impact than those further away. Integrating scales of observation and non-destructive testing has shown surface and subsurface fracture damage to be linked throughout the block, meaning surface damage provides a foundation for understanding the internal damage caused by bullet impacts. Therefore, by analysing the surface damage, inferences on the extent and degree of subsurface damage can be made without the need for destructive analysis methods.

Chapter 4

Bullet Impacts in Stone: Formation of Near-Conical Craters with a Close Control of Target Material

4.1 Abstract

Bullet impacts are a ubiquitous form of damage to the built environment resulting from armed conflicts. Bullet impacts into stone buildings result in surface cratering, fracturing, and changes to material properties, such as permeability and surface hardness. Controlled experiments into two different sedimentary stones were conducted to characterise surface damage and to investigate the relationship between the impact energy (a function of engagement distance) and crater volumes. Simplified geometries of crater volume using only depth and diameter measurements showed that the volume of a simple cone provides the best approximation (within 5%) to crater volume measured from photogrammetry models. This result suggests a quick and efficient method of estimating crater volumes during field assessments of damage. Over the engagement distances studied (100-400 m), there is little consistent effect on crater volume, but different target materials result in an order of magnitude variation in measured crater volumes. Bullet impacts in the experiments are similar in appearance to damage caused by hypervelocity experiments, but crater excavation

is driven by momentum transfer to the target rather than a hemispherical shock wave. Target material plays the dominant role in controlling damage, not projectile energy as predicted by some impact scaling relationships.

Author Contributions

This chapter is based on a published manuscript: Campbell, O., Blenkinsop, T., Gilbert, O. and Mol, L. (2022). Bullet impacts in building stone excavate approximately conical craters, with dimensions that are controlled by target material. *Scientific Reports*. 12(1). pp. 1-11. https://doi.org/10.1038/s41598-022-22624-z

Oliver Campbell is the main author of this work and undertook the creation of the photogrammetry models, characterisation of morphology, mechanical testing, data processing, data analysis and wrote the manuscript. Oliver Campbell and Oscar Gilbert performed the controlled firearm experiments. Oscar Gilbert conducted the ultrapulse velocity testing. Tom Blenkinsop and Lisa Mol provided supervision during the writing of the manuscript. Two anonymous reviewers provided constructive comments that helped further improve the submitted manuscript.

4.2 Introduction

Chapter 3 has shown that fracture damage can extend deep into the target material and generate 4-7 times more new surface area than the impact crater alone. It used 3D photogrammetry models to investigate the morphology of surface damage for a single bullet impact in sandstone.

This chapter investigates a simpler approach: can crater volumes be estimated using just depth and diameter measurements and simplified volume geometries? A simple approach for estimating crater volumes is invaluable for surveys of heritage damage in conflict zones, where factors such as safety or accessibility can limit effective time on site. In the latter part of the chapter, accurate crater volume estimates from photogrammetry are used to compare the damage and scaling relationships of bullet impacts with those of hypervelocity experiments. The comparison yields insights into cratering mechanics.

4.3 Methods Summary

Freshly quarried cubes (15 x 15 x 15 cm) of Stoneraise Red Sandstone (SRS) and Cotswold Hill Cream Limestone (CHCL) were selected as target materials for controlled impact experiments . Photogrammetry methods were used to generate 3D models of impact craters, from which cross section profiles and crater volume were extracted. Quasi-static compression experiments were undertaken to measure the uniaxial compressive and indirect tensile strengths of each stone type. Full details of these methods are provided in Chapter 2.

4.4 Results

4.4.1 Target Properties

Compression tests show that the sandstone targets have higher compressive and tensile strengths than the limestone targets (Table 4.1). Reported strengths are the average value of the n number of cores measured ± one standard deviation. The uniaxial compressive strength perpendicular and parallel to bedding for the Stoneraise Red Sandstone (SRS) ($n = 9$) is 40.0 ± 5.9 MPa and 44.0 ± 13.1 MPa respectively, while the Cotswold Hill Cream Limestone (CHCL) ($n = 9$) values are 10.6 ± 1.5 MPa and 8.8 ± 2.1 MPa respectively. The indirect tensile strength parallel to bedding (i.e. loading direction perpendicular to bedding) for the SRS ($n = 10$) is 5.0 ± 0.3 MPa and 2.2 ± 0.2 MPa for the CHCL ($n = 12$). SRS ($n = 9$) samples have a higher axial Young's Modulus with 2.6

± 0.4 GPa and 3.0 ± 0.6 GPa parallel and perpendicular to bedding respectively. CHCL (n = 9) has values of 1.5 ± 0.3 GPa and 1.1 ± 0.5 GPa for the same orientations. SRS (n = 12) has an average Ultrapulse Velocity (UPV) of 833 $\mathrm{m\,s^{-1}}$, faster than the average of 569 $\mathrm{m\,s^{-1}}$ in CHCL (n = 12) targets.

		Sandstone		n	**Limestone**		n
	Bulk UPV ($\mathrm{m\,s^{-1}}$)	833		12	569		12
Perpendicular to bedding	UCS (MPa)	40.0	± 5.9	9	10.6	± 1.5	9
	Axial Young's Modulus (GPa)	2.6	± 0.4	9	1.5	± 0.3	9
Parallel to bedding	UCS (MPa)	44.0	± 13.1	9	8.8	± 2.1	9
	Tensile (MPa)	5.0	± 0.3	10	2.2	± 0.2	12
	Axial Young's Modulus (GPa)	3.0	± 0.6	9	1.1	± 0.5	9

Table 4.1: Summary of the mechanical properties of Stoneraise Red Sandstone (SRS) and Cotswold Hill Cream Limestone (CHCL). Bulk UPV is the average value of ultrapulse velocities (UPV) measured in each orthogonal direction. n = number of samples tested to give average value.

4.4.2 Surface Damage

All experiments resulted in the formation of an impact crater and material loss. The floor of the impact craters have a fine grained, powdery appearance with a pale discolouration. Damage varies with lithology and projectile type. Sandstone targets impacted with AK-47 projectiles

	Sandstone		**Limestone**	
	AK-47	NATO [a]	AK-47 [b]	NATO
d (mm)	4.6	12.5	14.0	23.3
D_{eq} (mm)	33.8	47.3	59.8	65.1
V ($\mathrm{cm^3}$)	1.9	8.3	14.1	24.7
d/D_{eq}	0.13	0.23	0.23	0.35
Number of samples	4	5	3	4

Table 4.2: Summary of average depth (d), diameter (D_{eq}), measured volume (V), and depth/diameter ratio for targets of Stoneraise Red Sandstone and Cotswold Hill Cream Limestone shot with 7.62 × 39 mm (AK-47) and 5.56 × 45 mm NATO projectiles.
[a]Averages do not include sample SRS_23 which had an impact velocity significantly faster than other samples. For SRS_23: d = 17.5 mm, D_{eq} = 68.5 mm, V = 24.6 $\mathrm{cm^3}$, d/D_{eq} = 0.25.
[b]Averages do not include sample CHCL_09 which had an impact velocity significantly faster than other samples. For CHCL_09: d = 42.5 mm, D_{eq} = 102.2 mm, V = 107.6 $\mathrm{cm^3}$, d/D_{eq} = 0.42.

exhibit shallow, cone-shaped craters with average depths of 4.6 mm, diameters of 33.8 mm, and volumes of 1.9 cm^3 (Table 4.2). There are few visible surface fractures surrounding the impact crater and where present they are short and have closed apertures. Some samples have a dark grey discolouration in and around the impact crater from the lead core of the projectile (Figure 4.1). Limestone targets have a more complex, two-part structure of a deep central depression surrounded by a shallow dipping spall region (Figure 4.1). Of the four samples, three had impact velocities of 429 $\pm$ 5 $m\,s^{-1}$ and one of 532 $m\,s^{-1}$. The slower impacts had average depth and diameter measurements of 14.0 mm and 59.8 mm respectively. The faster impact had had larger values of 42.5 mm and 101.9 mm respectively. The crater volumes, measured from photogrammetry models, show the difference in dimensions between the slower and faster impacts, with the three slow impacts having an average volume of 14.1 cm^3 and the fast impact 107.6 cm^3.

The NATO projectile, excluding the test conducted at full propellant load, produced deeper (12.5 mm), wider (47.3 mm), and larger volume (8.3 cm^3) craters in the sandstone targets than the AK-47 projectiles. The test conducted at full propellant load had the largest diameter (68.5 mm) and volume (24.6 cm^3) of the six samples, but it was not the deepest crater. The steel tip of the NATO projectile remained embedded in the floor of the impact crater in five out of six experiments. Crater profiles are more complex than the simple cone-shaped craters created by AK-47 projectiles, with a shallow spall zone surrounding a steep sided central excavation. Fractures with open apertures radiate from the impact crater, and can reach the edge of the target face. Limestone targets have more radial fractures with wider apertures than impacts into sandstone targets. The craters have a two-part structure of steep sided central excavation and shallow dipping spall zone. NATO impacts into limestone targets caused craters with an average depth of 23.3 mm and diameter of 65.1 mm. Crater volumes are over twice as large (24.7 vs. 11.0 cm^3) as comparable impacts into sandstone targets. For the studied engagement distances (i.e. simulated distance between firearm and target), the impact energy does not appear to have a strong influence on crater volume. For near identical impact energy, there can be up to an order of magnitude difference in crater volume (Figure 4.2).

Of the studied simplified crater geometries, the simple cone provides the closest estimate to the volume of the crater measured by photogrammetry, with sandstone craters underestimated 4.9% on average and limestone craters slightly overestimated by 1.4%. These values are substantially smaller than the overestimation for sandstone and limestone craters by the spherical cap (52.8% and 80.2% respectively) and paraboloid (42.6 and 52.1% respectively) geometries (Table 4.3, Figure 4.3a). The simple cone geometry was also applied to asymmetric craters created by oblique impacts.

The geometry estimates crater volumes within 6.3% of the photogrammetry values, almost as accurate as for the perpendicular impacts (4.9%).

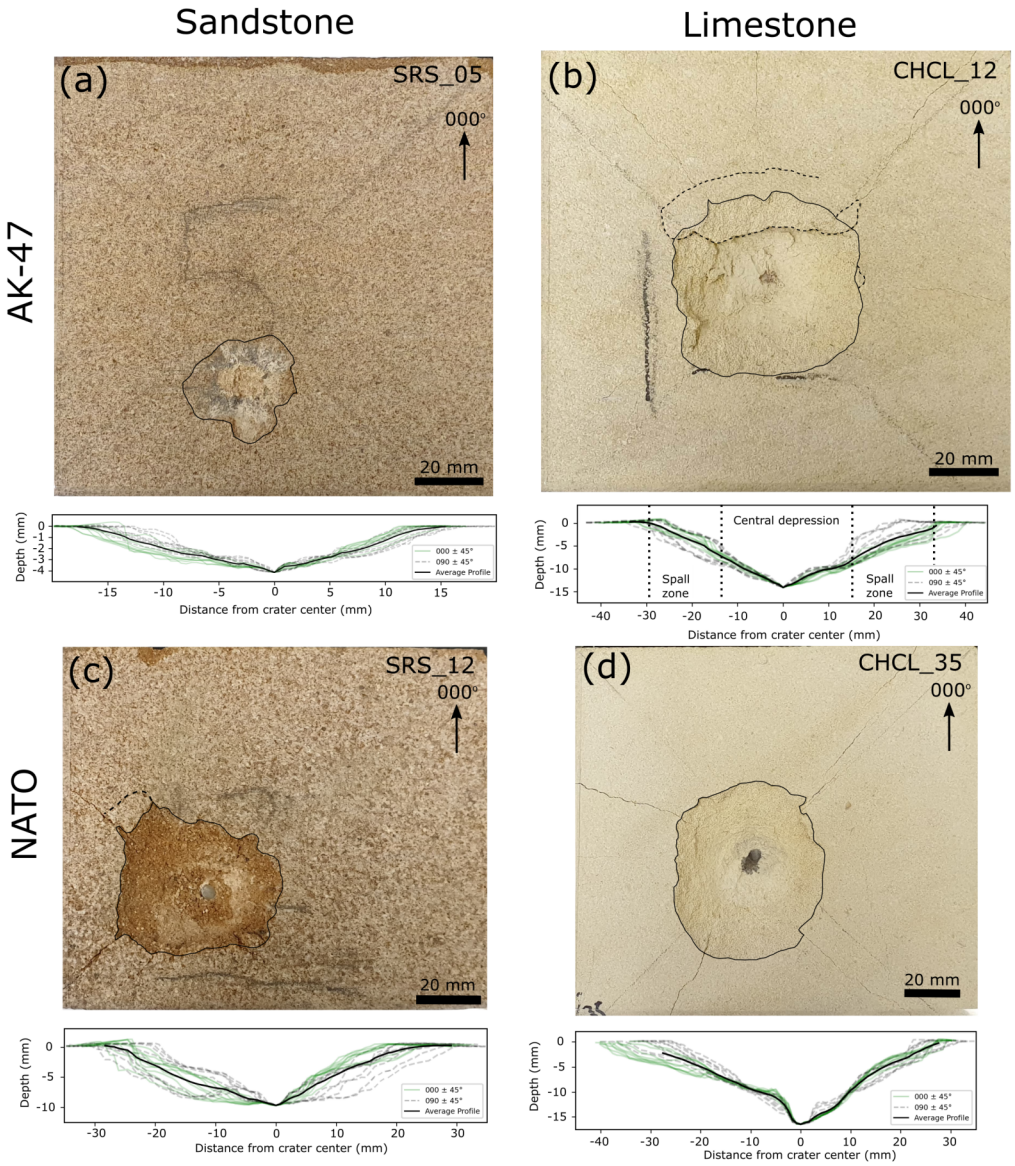

Figure 4.1: Photographs of impact craters and summary of 18 cross section profiles caused by 7.62 × 39 mm (AK-47) (a-b) and 5.56 × 45 mm NATO (c-d) projectiles. An azimuth direction of 000° points towards the top edge of the target block in its firing position. Profiles oriented between 000° ± 045° are coloured green, while profiles oriented 45° either side of 090° are dashed grey. The crater outline is marked with a solid black line and incipient spall fragments by a dashed black line. Fractures can be seen radiating from the impact crater to the edge of the target block. The steel tip of the NATO projectile can be seen embedded in the target block (c-d).

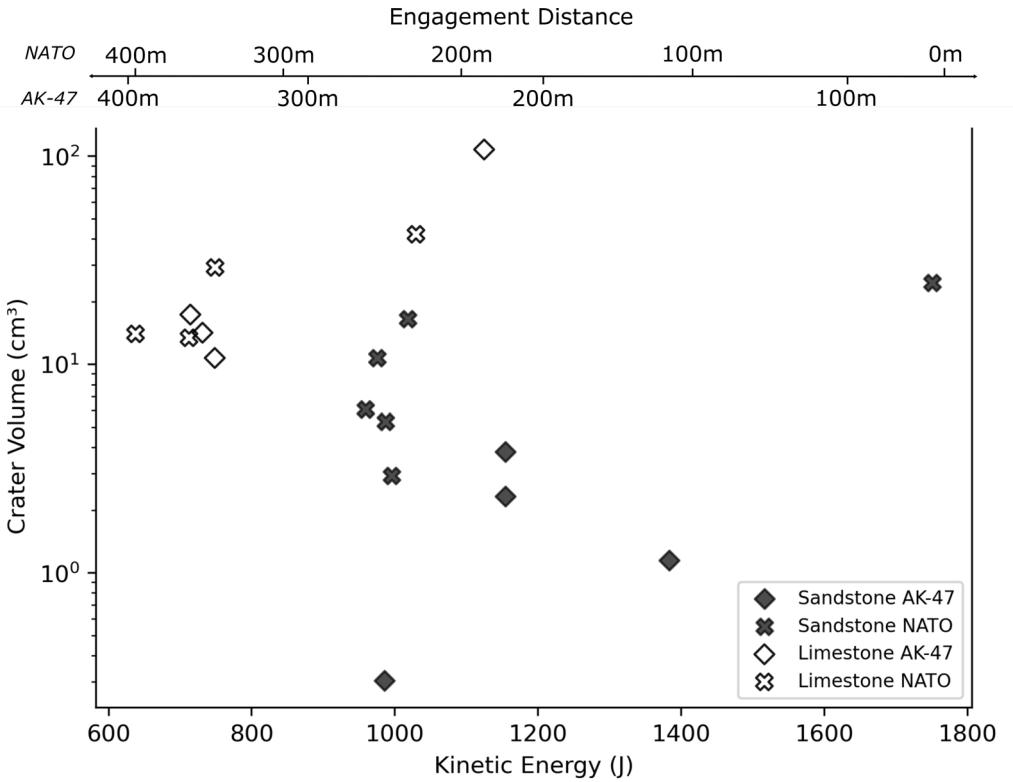

Figure 4.2: Photogrammetric crater volume against the kinetic energy of projectiles, 7.62 × 39 mm (AK-47) and 5.56 × 45 mm NATO, at impact. Engagement distance is derived from the projectile velocity for a given kinetic energy.

Geometry	**Sandstone**	**Limestone**
Simple Cone	-4.9 ± 12.0	1.4 ± 18.2
Spherical Cap	52.8 ± 23.2	80.2 ± 61.2
Paraboloid	42.6 ± 17.9	52.1 ± 27.4

Table 4.3: Average differences (as a %) between estimated and measured crater volumes. Positive values represent an overestimation of measured volume. Data is only grouped into lithology type because further separation into projectile type adds little to the discussion.

4.5 Discussion

For both the simple cone-shaped crater and the more complex two-part structures, radial fractures centred on the impact crater, and crushed target material on the crater floor, resemble damage resulting from hypervelocity experiments (Lange et al., 1984; Polanskey & Ahrens, 1990; Dufresne

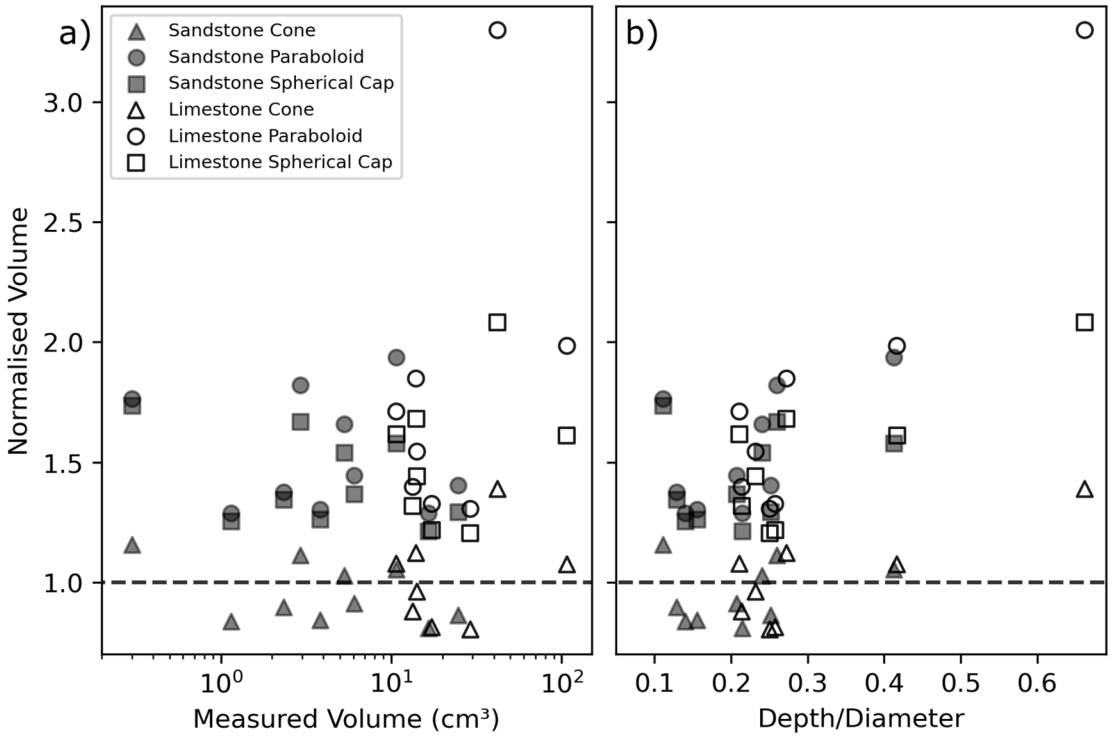

Figure 4.3: (a) Estimated crater volumes normalised to the crater volume measured from photogrammetry models plotted against photogrammetric volume. Sandstone targets (filled markers) have smaller crater volumes than limestone targets (hollow markers). The simple cone geometry (triangle marker) provides the closest estimate to the measured volume (dashed line). (b) Estimated crater volumes normalised to the crater volume measured from photogrammetry models plotted against depth/diameter ratio. There is a statistically significant, though weak, trend of increasing overestimation with increasing depth/diameter ratio.

et al., 2013). In this study, relatively undeformed projectile material (steel tip of NATO projectile) is embedded in the floor of the crater, unlike most hypervelocity experiments in which the projectile is melted and/or ejected (Baldwin et al., 2007; Ebert et al., 2013). The embedded projectile material here lies at the base of short, cylindrical penetration channels, akin to observations made from experiments investigating the penetration of rigid steel rods into concrete (Rajput & Iqbal, 2017). Corrosion of the projectile's steel tip when exposed to the elements over some time after impact may locally exacerbate fractures, similar to the deterioration seen in reinforced concrete due to corrosion of rebar, except on a much smaller scale (Li, 2003). There is no evidence of any AK-47 projectiles penetrating into targets, only smearing of lead material around or in the impact crater.

The simple cone geometry provides the best estimation (within 5%) of the measured crater volume using depth and diameter measurements. The spherical cap and paraboloid geometries substantially overestimate the measured crater volume. This overestimation stems from the morphological differences of the geometries, visualised in Figure 4.4. The concave down form of crater walls, created by the two part structure of a deep central pit and surrounding spall zone, diverges from the simplified geometries (cone, spherical cap, paraboloid) which have straight or concave up crater walls. This effect is more prominent in the spherical cap and paraboloid geometries, which is reflected in over estimations of 50 - 80%. Additional geometry measurements, such as the width and depth of the central excavation or spall zone, may provide better estimates of crater volume, but the extra time and effort required in measuring these values would compromise the goal of a

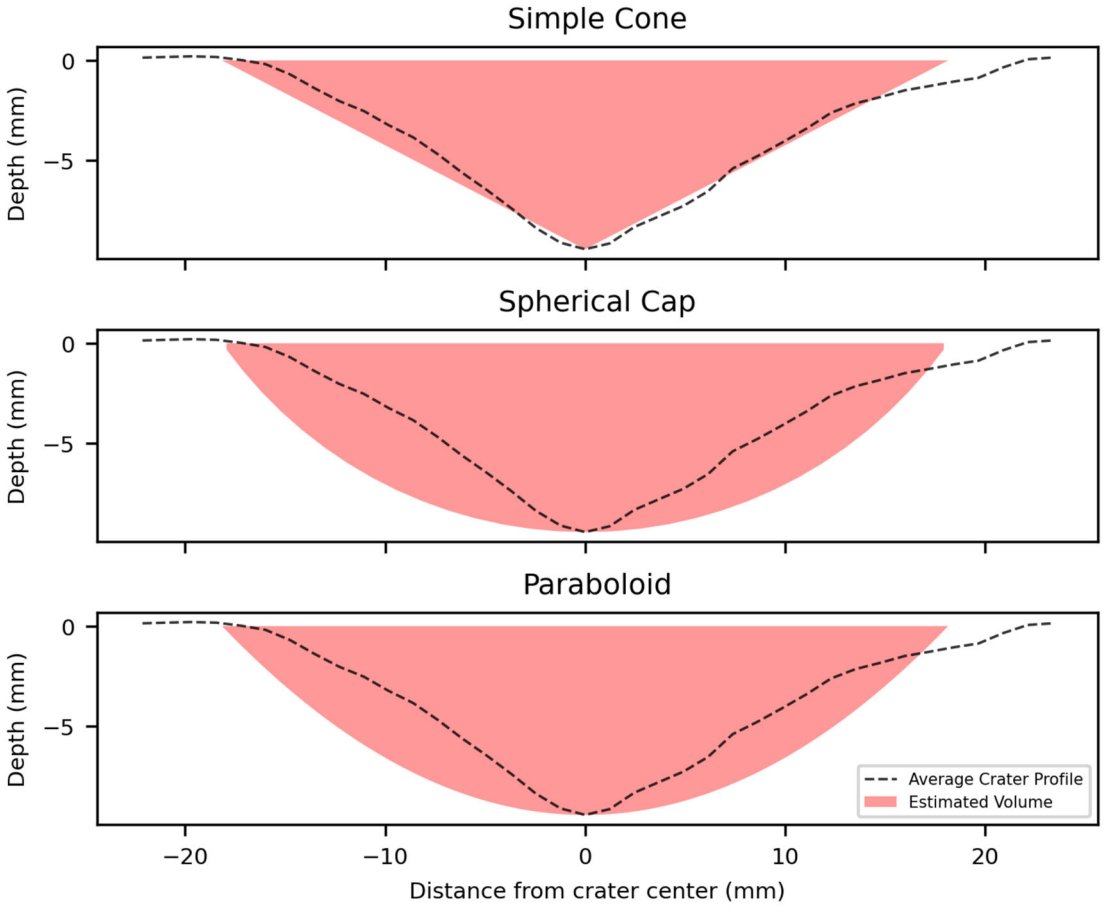

Figure 4.4: Average cross section profile of sample SRS_14 and cross section through the simplified crater geometries that use the max depth and D_{eq}.

quick and efficient field method.

Simplifying crater geometries to estimate volume from two rapidly acquired measurements allows many impacts to be studied in a shorter time than photogrammetry. Measurements of depth and diameter are possible with simple analogue tools such as calipers and depth gauges. Although this study took a digital approach to these measurements, it is unlikely the substitution with analogue values will affect the overall conclusions, as Chapter 6 shows reasonable agreement between analogue crater profiles obtained using a Barton comb and profiles measured from photogrammetry models. Volumes can be estimated in the field with the simplified geometry, providing an overview of crater volume distribution while investigators are on site, supporting first-response assessments of conflict damage to heritage. Imaging of a site for photogrammetry models can be done relatively quickly (minutes per impact), but the post-field production and analysis of models (hours to tens of hours) lengthens the overall method time. Smartphones cameras, and the Light Detection and Ranging (LiDAR) capability of new generation iPhones or hand-held scanners, are increasingly able to generate 3D SfM models approaching the precision of those using digital cameras and SfM software, or those derived from terrestrial laser scanning (TLS) (Luetzenburg et al., 2021; Riquelme et al., 2021). The LiDAR sensors in iPhones were developed to enhance photographs, and not to produce surface coordinates like traditional TLS. However, downloadable applications have been developed to utilise the iPhone hardware to produce models that are of comparable precision to SfM and TLS methodologies (Luetzenburg et al., 2021). At present, the measurement of crater volumes and fracture orientations from 3D models in the field is still limited by the need for computers with appropriate software. Analogue field measurements remain the simplest and most accessible means of initial damage assessment.

Photogrammetry and simplified volume estimations could be viewed as complimentary methods. Volume estimation from depth and diameter measurements provides a good first order method of quantifying impact damage and its distribution, enabling on site testing of hypotheses and targeted data collection towards areas at highest risk of future deterioration. If the situation permits, imaging of the site for SfM photogrammetry models provides a more accurate quantification of the damage, as well as digitally preserving heritage sites in a way that can be used as a baseline to track changes over time (Westoby et al., 2012; Mol & Clarke, 2019).

The three simplified geometries presented here show an increasing overestimation of crater volume with increasing depth/diameter ratio (Figure 4.3b). This is likely the result of the deeper central pits, causing divergence of crater wall morphology from the straight or concave up profile of the simplified geometries. Therefore care should therefore be taken when estimating the volume of

craters with higher depth/diameter ratios. This method has been developed for impact craters with good rotational symmetry (created by perpendicular impacts), however the simple cone geometry does suitably estimate the volume of craters created by oblique impacts (within 6.3%).

In hypervelocity experiments, crater volume is linked to the kinetic energy of the projectile (i.e. impact energy). The greater the amount of energy available, the larger the peak pressures experienced by the target, and the greater the material failure (Rinehart, 1968; Holsapple, 1993; Zhang et al., 2000). Hypervelocity experiments exhibit well established correlations between increasing impact energy and crater volume (Figure 4.5). Impact energies and crater volumes presented here are of a similar magnitude to some hypervelocity experiments. However, for the range of impact energies of this study (approximating engagement distances of 100 - 400 m) , the crater volumes

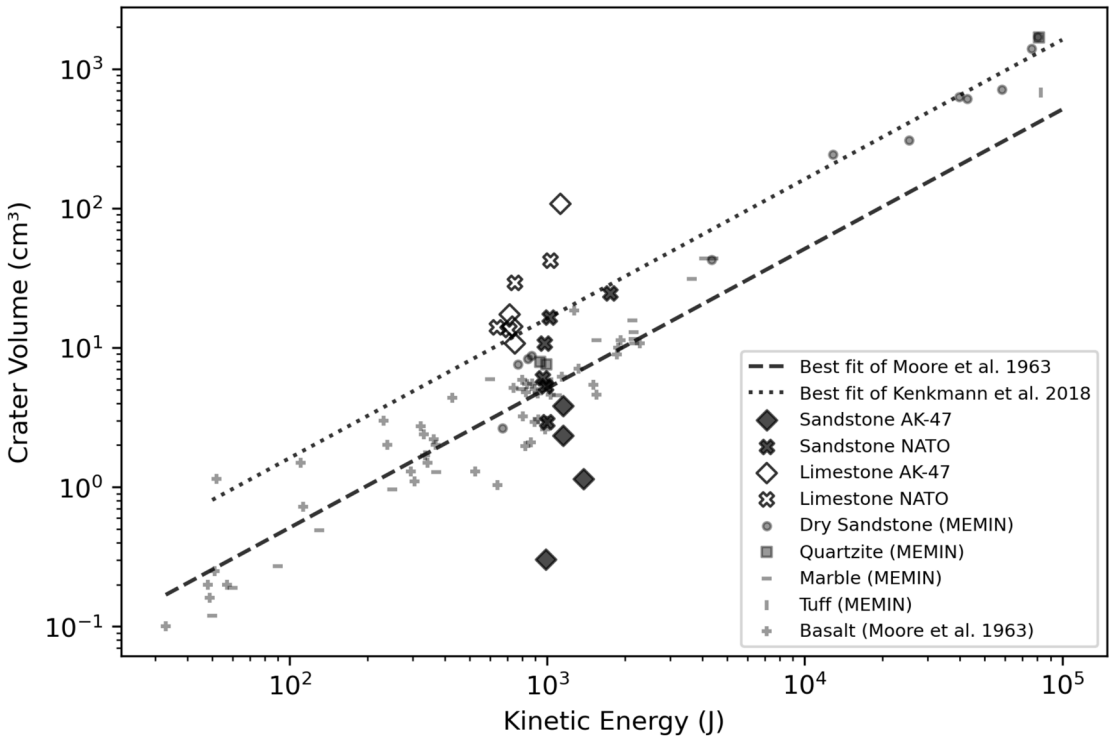

Figure 4.5: Plot showing the trend of increasing crater volume with increasing kinetic energy (at impact) displayed by hypervelocity experiments from Moore et al. (1963) and the Multidisciplinary Experimental and Modelling Impact Crater Research Network (MEMIN) (Kenkmann et al., 2018). The results of this study have a wider range of crater volumes for the narrow range of impact energies studied, particularly impacts into sandstone with 7.62 × 39 mm (AK-47) projectiles. NATO = 5.56 × 45 mm NATO projectile.

do not follow the relationship with impact energies observed in the MEMIN (Multidisciplinary Experimental and Modelling Impact Research Network (Kenkmann et al., 2018)) or Moore et al.'s (1963) hypervelocity studies. For a given impact energy, limestone targets from this study have larger crater volumes than hypervelocity experiments, whereas sandstone targets impacted by AK-47 projectiles have smaller volumes. No systematic relationship between crater volume and impact energy is evident.

To compare impact experiments into targets with different properties, it is useful to use dimensionless parameters. Holsapple 1993 gave a generalised equation for crater volume in strength-dominated (i.e. the scale of impact means crater formation processes are governed by material strength), non-porous materials:

$$V \propto \frac{m}{\rho_t} * (\frac{\rho_t v_i^2}{Y})^{\frac{3\mu}{2}} * \frac{\rho_t}{\rho_p}^{1-3v} \tag{4.1}$$

where V is the crater volume, m, ρ_p and v_i are the projectile mass, density and velocity, ρ_t is the target density, Y is the measure of target strength, and μ and v are scaling exponents (Poelchau et al., 2014). For strength controlled craters, V increases at a rate somewhere between momentum scaling ($V \propto mv_i$) and energy scaling ($V \propto mv_i^2$), imposing limits for μ of: $1/3 < \mu < 2/3$ (Holsapple & Schmidt, 1982; Poelchau et al., 2014). Equation 8 can also be written using three scaling parameters (pi-scaling): cratering efficiency (π_v), a strength term (π_3), and a density term (π_4):

$$\pi_v \propto \pi_3^{\frac{-3\mu}{2}} * \pi_4^{1-3v} \tag{4.2}$$

Multiple linear regression of the experiments conducted here failed to produce values for μ and v of any statistical significance and within the limits for μ. The creation of the generalised equation for non-porous materials poses the question of its applicability to the porous targets of this study. However, hypervelocity impact experiments with a range of non-zero porosities could be used to calcualte values of μ and v (Moore et al., 1963; Gault & Wedekind, 1978; Kenkmann et al., 2018), whilst numerical models found no change in μ for target porosities 0-35% (Wünnemann et al., 2011). This suggests that target porosity is not the sole reason for the failure to obtain values of μ and v in this study.

The use of pi-scaling assumes that the impact causes a shock wave that is equivalent to an explosion at depth, and assumes a point source (Gault & Wedekind, 1978). The validity of this assumption may be why hypervelocity impact craters remain relatively circular except at very

low impact angles (Gault & Wedekind, 1978). A condition of the point source assumption is that impact velocity far exceeds the target sound speed (Housen & Holsapple, 2011). The impact velocities of the experiments reported here are similar or below the UPV (i.e. sound speed) values of the target lithology, so these experiments may not produce a shock wave at impact. Without a shock wave, crater excavation is instead driven by momentum transfer from the projectile to the target, a process influenced by the strength of both the target and projectile materials. Limestone targets in this study had compressive and tensile strengths 75-80% and 50% weaker respectively than the sandstone targets, resulting in greater crater volumes than sandstone impacts, even at lower impact energies (Figure 4.2 & 4.5).

The strengths of each target lithology were measured under quasi-static strain rates ($< 10\ s^{-1}$), but rock strength is strain rate dependent, increasing rapidly after a critical threshold strain rate (Zhang & Zhao, 2014). Rae et al. (2020, 2021) show that at stain rates $> 10^2\ s^{-1}$, the dynamic compressive strength of rocks can be double the quasi-static strength. Cho et al. 2003 show that dynamic tensile strength is greater than the static strength at strain rates 10^0 - $10^1\ s^{-1}$. They suggest that microcrack formation relieves the stress on adjacent microcrack tips, arresting the formation of a defined fracture plane. With increasing strain rate and frequency of microcracks, increasing stress is accommodated without fracture plane formation, resulting in a high dynamic tensile strength (Cho et al., 2003). The free surface at the block surface may influence the stress field around microcracks in a similar way, relieving stress and arresting fracture plane formation. Bullet impacts exhibit strain rates of 10^3 – $10^6\ s^{-1}$, varying due to quantities such as target and projectile material, impact energy, impact trajectory, and projectile shape (Clifton, 1980; Walley, 2010; Rosenberg & Dekel, 2016). The target strengths used here are therefore a minimum value. The clear correlation between target strength and crater volume indicates that any increase in strength due to strain rate may be comparable between the two lithologies.

The projectile strength in these experiments appears to have an influence on damage, with the harder steel tip of the NATO projectile resulting in larger impact craters than comparable impacts using the lead cored AK-47 projectiles. The steel tip of the NATO projectiles remains relatively undeformed and embedded in the crater floor, likely experiencing a greater interaction time with the target. Barnouin-Jha et al.'s (Barnouin-Jha et al., 2007) low velocity (85 – 250 $m\,s^{-1}$) experiments yielded results incompatible with proposed crater scaling relationships, which was suggested to have been due to increased interaction time between projectile and target. They propose that the penetration time is critical to the cratering process, and that depth/diameter ratios will be larger than expected for impacts at much higher velocities. Kenkmann et al., (2018)

reported depth/diameter ratios ranging from 0.1 to 0.56 for impact velocities of 2,500 – 7,850 $m\,s^{-1}$. Average depth/diameter ratios of experiments here (0.13- 0.35) fall within this range of values for much lower impact velocities, so do not initially appear to support Barnouin-Jha et al., 2007 suggestion. The ogival shape of the projectiles in this study is different from the spherical projectiles used in both the hyper- and low velocity experiments discussed, possibly increasing penetration potential and reducing the direct comparability between the sets of experiments.

Target lithology is a greater factor determining final crater volume than impact energy, despite the scatter observed here (Figure 4.5). This could be used in conjunction with knowledge of heritage construction materials to prioritise post-conflict efforts on weaker materials. Any process that reduces stone strength, such as mechanical damage during construction or chemical and physical weathering, will make these particular regions of monuments more susceptible to greater damage. Conversely, processes that may increase the strength of the stone, such as confining pressure from the surrounding structure, could reduce the amount of damage experienced in these regions. There is up to an order of magnitude variation amongst the crater volumes measured from photogrammetry models for the same impact energy (see NATO projectile into sandstone targets in Figure 4.2). The cause of this variability in impact geometry under very similar impact conditions may be the result of internal variations within target lithologies. Despite target blocks being quarried from the same beds and oriented in the same way with respect to internal foliation, natural sedimentary stone has inherent variability that may result in variable crater volumes for the same conditions. There is similar inherent variability in hypervelocity experiments (e.g. MEMIN (Kenkmann et al., 2018) and Moore et al.'s (1963) data, Figure 4.5), for which scaling relationships could still be derived. Some different form of scaling relationships might exist for the ordnance velocity experiments presented here, which additional experiments at a greater range of impact energies could help to derive.

4.6 Conclusions

Bullet impacts into limestone produce wider, deeper, and more voluminous impact craters than the same projectiles impacting sandstone targets. Limestone targets also have tensile strength 50% lower, and compressive strength values 75% lower than sandstone targets. Sandstone targets impacted with 7.62 × 39 mm (AK-47) projectiles have shallow, cone-shaped craters. Targets impacted with 5.56 × 45 mm NATO projectiles, and impacts of both projectiles into limestone targets, have a two part-structure consisting of steep sided central excavation pit surrounded by

a shallow dipping spall zone. Radial fractures are centred around the impact and reach the edge of the target block, providing conduits and entry points for weathering agents such as salt and moisture.

The volume of a simple cone, calculated from two simple measurements of crater depth and diameter, estimates crater volume within 5% of the accurate value determined from photogrammetry models. This result allows for a quick and efficient method for initial assessment of heritage sites damaged in armed conflict.

Impact craters generated here are similar in size and morphology to craters generated by hypervelocity experiments. However, projectile velocities below the sound speed of the target, penetration of the projectile, and the lack of scaling between crater size and impact energy, imply that damage is not governed by a shock wave. Crater excavation is instead controlled by momentum transfer, strongly influenced by target and projectile properties. Thus over the range of impact energies studied, engagement distance has little consistent effect, but target material typically creates an order of magnitude variation in crater volume. This suggests that heritage sites built of stone with lower strength values are at risk of greater damage from conflict.

Chapter 5

Subsurface Fracture Damage Caused by Bullet Impacts in Stone

5.1 Abstract

The immovable nature of built heritage means that it is particularly vulnerable during times of armed conflict. Although impacts from small arms and shrapnel leave relatively inconspicuous impact scars, they may elevate the risk of future stone deterioration. This study investigates the subsurface damage caused by bullet impacts, which is not apparent from surface inspection, in order to better understand the geometry and mechanics of this form of conflict damage to heritage. Controlled firearm experiments were conducted to simulate conflict damage to sandstone and limestone buildings. The bullet impacts created conical fractures or zones of increased fracture intensity below the impact, radial fractures and spallation, in addition to a crater. Dynamic fracture distinguishes the formation of these features from quasi static cone crack experiments, while the lack of a shockwave differentiates these bullet impacts from hypervelocity experiments. Damage was created by momentum transfer from the bullet, so that differences in target properties had large effects on the nature of the damage. The crater in the limestone target was almost an order of magnitude deeper than the sandstone crater, and large open fractures formed in the limestone below the crater floor, compared with zones of increased fracture intensity in the sandstone target. Microstructural analysis of subsurface damage showed that fracture intensity decreased with increasing distance from the impact centre, suggesting that regions proximal to the impact are at increased risk of future deterioration. Conical subsurface fractures dipping away from the

impact beneath multiple impact craters could link up, creating a continuous fracture network. By providing pathways for moisture and other weathering agents, fractures enlarge the region at increased risk of deterioration. Their lack of surface expression makes understanding their formation a vital part of future surveying and post conflict assessments.

Author Contributions

This chapter is based on a submitted manuscript: Campbell, O., Blenkinsop, T., Gilbert, O. and Mol, L. (in press). Subsurface fracturing of sedimentary stones caused by bullet impacts. *PLOS One* (PREPRINT) doi: https://doi.org/10.31223/X5RD3H

Oliver Campbell is the main author of this work and undertook the microstructural analysis, data processing, and wrote the manuscript. Oliver Campbell and Oscar Gilbert performed the controlled firearms experiments. Tom Blenkinsop and Lisa Mol provided supervision during the writing of the manuscript.

5.2 Introduction

Chapter 3 showed that the surface damage and internal fracturing were intrinsically linked, so this chapter aims to characterise and quantify the subsurface damage caused by modern rifle bullets in greater detail. This will further the understanding of damage mechanisms, and aid in linking the damage to potential deterioration of built heritage. Observations of fracture morphology from thin sections studied under optical microscopy are combined with fracture intensity analysis of digitised fracture maps to examine how subsurface damage changes with distance to the crater centre.

5.3 Methods Summary

Freshly quarried cubes (15 x 15 x 15 cm) of Stoneraise Red Sandstone (SRS) and Cotswold Hill Cream Limestone (CHCL) were selected as targets for controlled firearm experiments to produce damaged stone blocks, as detailed in Chapter 2. Targets were shot with 7.62 × 39 mm ammunition, with propellant loads modified to reduce projectile velocity and simulate impacts from a distance of 200 m. Impact velocities of 521 $\mathrm{m\,s^{-1}}$ for the CHCL target and 539 $\mathrm{m\,s^{-1}}$ for the SRS target resulted in projectile kinetic energies of ∼1125 J and ∼1154 J respectively. The crater centre is defined as the point a the centre of the crater floor, typically the deepest point, and is used as the reference point from which distances to fractures and features of damage are measured within the sample. Polished thin sections were cut through the middle of the impact crater, parallel to the XZ plane, as described in Chapter 2. Fracture intensity analysis was carried out for both samples following the methodology described in Chapter 2.

5.4 Results

5.4.1 Sandstone Target

The SRS sample (SRS_09) has a shallow, roughly conical shaped crater with an area equivalent diameter of 40 mm and a maximum depth of 5.1 mm (Campbell et al., 2022b). 15 mm directly below the crater floor is an open (< 1.5 mm) fracture that is approximately 16 mm in length, but does not reach the edge of the section (Figure 5.1). 80 mm directly below the crater centre there is an open fracture with a minimum aperture of 1.4 mm. Maximum aperture cannot be determined because the upper fracture wall shows evidence of material loss from sectioning (Figure 5.1a,b).

Both of these open fractures are sub-parallel to the orientation of the beds defined by grain size changes, ∼5° from the target face (95°/275° relative to the assigned 'North' of the thin sections). Two relatively dominant orientations of fractures become apparent from the rose diagram : the first are, as described above, sub-parallel to the orientation of internal bedding (95°/275°), while the second group is approximately orthogonal to this with orientations 0°/180° (Figure 5.1c).

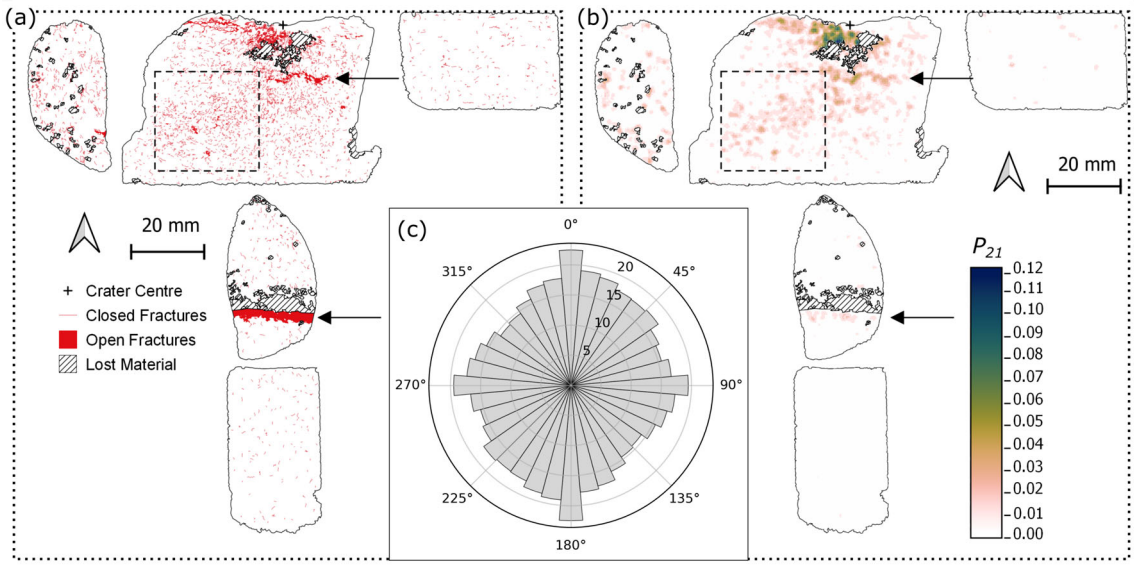

Figure 5.1: Fracture map (a) through the centre plane (XZ) of a Stoneraise Red Sandstone sample (SRS_09). Open fractures (solid red regions) are visible oriented sub-parallel to the target surface close to the impact crater, at a depth of 20 mm and ∼80 mm below the crater (black arrows). There is a high number of closed (red line) fractures within a 7 mm radius of the crater centre. (b) Map of P_{21} fracture intensity values across the thin sections. The highest values (dark blue) are within 7 mm of the crater centre. There is a region of relatively higher fracture intensity (dashed square) with an approximate orientation of 35°/215°. For both maps impact direction is top to bottom and the original block outline is shown as a dotted line. (c) Equal area rose diagram showing the orientation of all fractures, weighted for fracture length, mapped within the sandstone sample. Radial scale is the square root of the weighted frequency.

Directly below the crater centre is a zone of primarily intra- and trans-granular fractures, forming a zone of intense fracturing that extends to a depth of ∼7 mm below the crater floor (Figure 5.2a-e). The highest P_{21} fracture intensity value calculated (0.124) is in this region, 5.9 mm away from the crater centre (Figure 5.1b, 5.2d). The largest negative and positive uncertainties for P_{21} values are -0.0101 mm^{-1} and $+0.0720$ mm^{-1} respectively, with an average uncertainty of $+0.0004$ mm^{-1}. Many grains exhibit multiple closed fractures that originate at contact points with

adjacent grains, forming connected networks across multiple grains. Open, extensional fractures are visible just beneath the crater floor, traversing from the crater centre towards the crater rim (Figure 5.2f-g). These fractures have both inter- and trans-granular pathways, with no measurable lateral displacement between fracture walls. They are primarily sub parallel to the target face of the samples (Figure 5.2h). In the top central section there appears to be a band of damage stretching from the southwest (SW) corner of the section to an area of material loss directly below the crater centre (Figure 5.2i-k). The band has an approximate orientation of 35°/215°. There are few fractures in the thin sections beyond the large open fractures 80 mm below the crater floor. The few fractures present are short, intra-granular fractures, typically confined to a single grain. This is visible in the peak in P_{21} intensity at 80 mm below the crater centre (Figure 5.3), followed by very low intensity values moving further from the crater centre.

There are few fractures in the thin sections beyond the large open fractures 80 mm below the crater floor. The few fractures present are short, intra-granular fractures, typically confined to a single grain. This is visible in the peak in P_{21} intensity at 80 mm below the crater centre (Figure 5.3), followed by very low intensity values moving further from the crater centre.

Figure 5.2: (*Figure Overleaf.*) (a) Fracture map of the thin section through the impact crater in Stoneraise Red Sandstone (SRS_09), showing closed and open fractures (red). Dashed box shows the location of panels (b-e). Solid black box outlines the location of panels (f-h). Grey box shows the location of panels (i-k). (b) Reflected light photomicrograph showing substantial grain crushing (top of frame) at the crater floor and a high number of trans- and intergranular fractures in the region beneath. Interconnected fracture pathways are seen in the fracture map in panel (c). The highest fracture intensity value (0.124) is observed in the lower right of the P_{21} intensity map (d), 5.9 mm from the crater centre (out of frame towards the top right). Topology parameters were calculated using the branch network (black lines) interpreted by the NetworkGT plugin based on a threshold image of the digitised fractures (red lines). The orientations of the digitised fracture network show a slight predominance in orientation around 45°/225° and 90°/270°. (f-g) Reflected light micrograph and corresponding fracture map of open, extensional fractures directly below the crater edges. Fractures are oriented sub-parallel to the target face as seen in the rose diagram for the region (h). (i) Reflected light photo micrograph and fracture network showing a region of fracturing from below the crater to the SW corner of the central section. (j) P_{21} fracture intensities and NetworkGT branch map for the same region. There appears to be a slight trend of fracture orientations from 45°/225° (k), though the dominant orientation for the region is perpendicular to the target face. All rose diagrams (e, h, k) are plotted as equal area diagrams, orientation frequency is weighted for fracture length, and the radial scale is the square root of the weighted frequency.

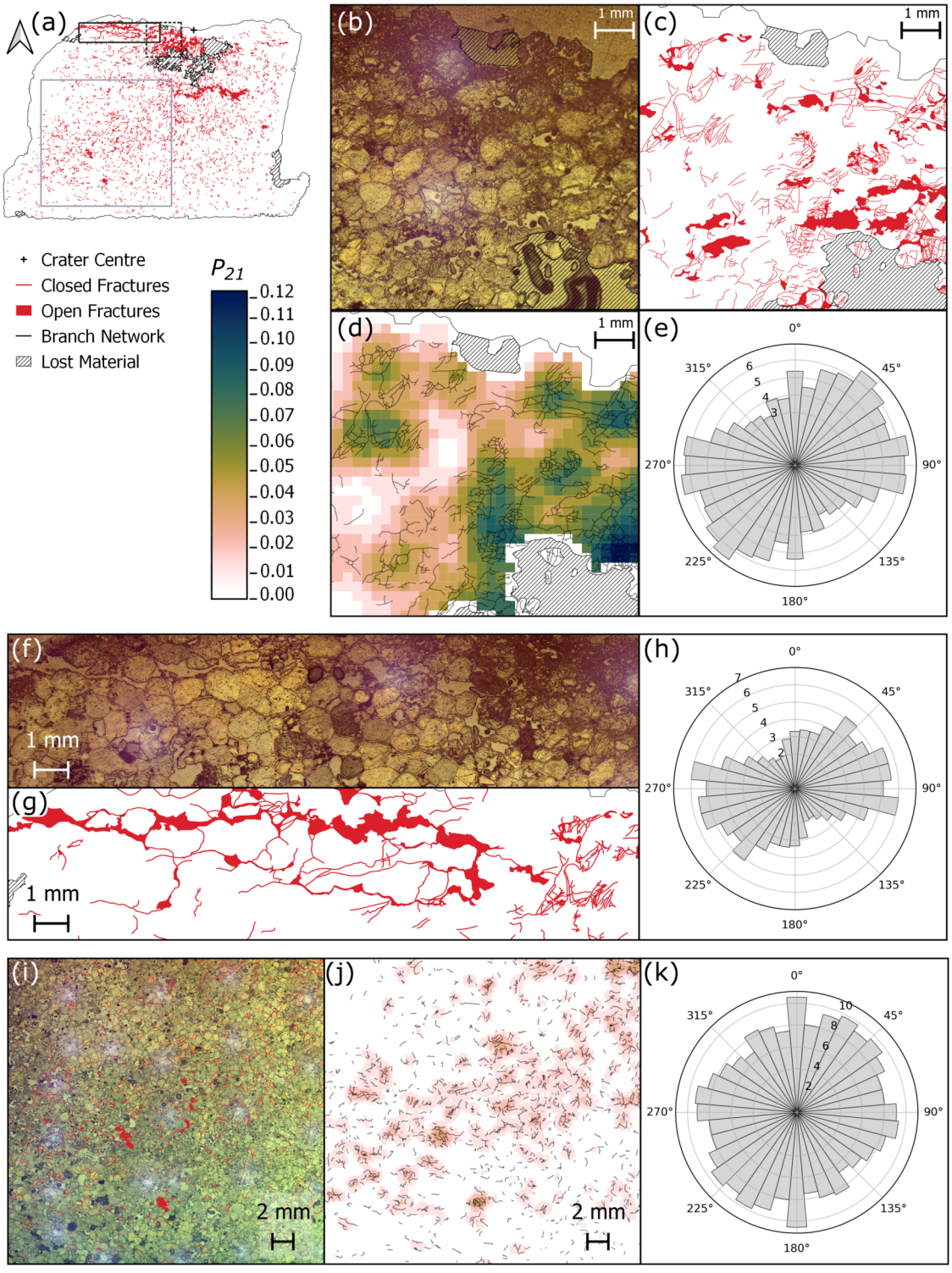

Figure 5.2: *Caption on previous page.*

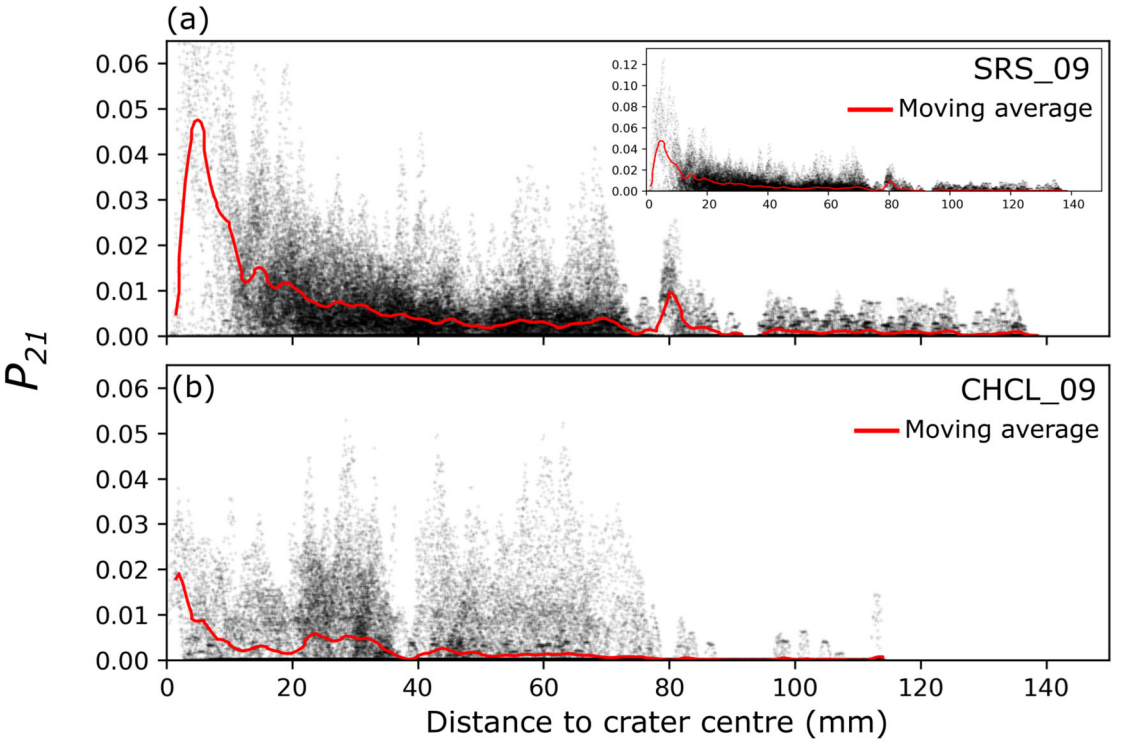

Figure 5.3: P_{21} fracture intensity with increasing distance from the crater centre for the sandstone (a) and limestone (b) target blocks. Red line is a 2 mm moving average of P_{21} intensity with distance from crater centre. Inset shows the full extent of P_{21} values in the sandstone target.

5.4.2 Limestone Target

The limestone target (CHCL_09) has a wider (101.9 mm) and deeper (42.5 mm) crater than the sandstone sample (Campbell et al., 2022b). The crater has a two-part structure of shallow dipping outer spall zone surrounding a deeper, flat bottomed pit. The inflection point between these two regions on the crater edges forms an overhang with the upper wall of large open fractures. The open fractures have a gently convex up shape across multiple thin sections, reaching the edge of the target block (Figure 5.4a). It was noted during thin section production that these fractures have surface exposure on the faces adjacent to the impacted face. The exposure in thin section represents a 2D profile through an axis-symmetric, conical shaped fracture plan with its apex at the impact crater. The aperture of the open fracture is at its widest (∼13 mm) where it intersects the crater, narrowing to ∼1.5 - 2 mm near the edge of the target block. This fracture forms a wedge of incipient material (incipient wedge) that appears to be unconnected to the rest of the

target block in the plane of observation. Peak P_{21} values in the limestone target are lower than those in the sandstone (0.053 vs. 0.124, with high P_{21} values localised in the near surface region of the spall zone in the top right section, beneath the crater floor, and around the open fractures (Figure 5.4b). The largest negative and positive uncertainties for P_{21} values are -0.178 mm^{-1} and $+0.0005$ mm^{-1}.

Fractures throughout the sample are generally sub-parallel to the target face (Figure 5.4c), although there is another group of fracture with an orientation 50°/230°. Material below the spall zone surface is highly fractured, with grain sizes beyond the scale of observation in optical sections (Figure 5.5a-c). The top surface of the incipient wedge is the floor of the spall zone surrounding the central excavation, and has an orientation of approximately 45°/225°. Some fractures within the wedge, particularly those close to the spall surface, are oriented parallel to the spall surface, while other fractures throughout the wedge have an orientation perpendicular to this surface (Figure 5.5c). Higher P_{21} values are localised around these fractures and their intersections (Figure 5.5d). This orthogonal pair of fractures is bisected by a third group, with orientations of approximately 100°/280° (Figure 5.5e).

Clasts of wall rock are present within the aperture of large open fractures that traverse multiple sections. there are several narrower (> 15 mm) open fractures sub parallel to, but distinct from, the large fractures (Figure 5.5f). Up to 2 mm beneath the floor of the central excavation there is a

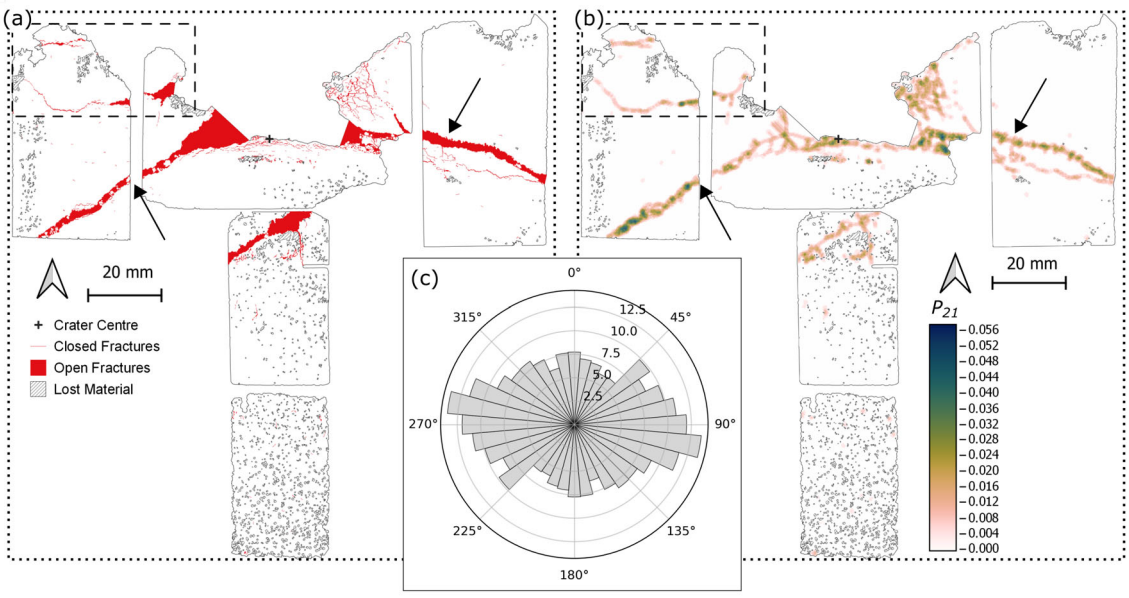

Figure 5.4: *Caption overleaf.*

Figure 5.4: (*Figure on previous page.*) Fracture map (a) through the centre plane (XZ) of the Cotswold Hill Cream Limestone (CHCL) sample (CHCL_09). An open fracture (black arrows) is present across multiple thin sections, intersecting the edges of the target block and the crater. Open fractures are visible sub-parallel to the target face and forming incipient spall fragments (dashed rectangle). There are crater floor parallel, closed fractures (red line) directly below the crater centre. (b) Map of P_{21} fracture intensity values across the thin sections. The highest values (dark blue) are localised along the wide open fracture (black arrows) and around the crater centre. For both maps impact direction is top to bottom and the original block outline is shown with a dotted line. (c) Equal area rose diagram showing the orientation of all fractures, weighted for fracture length, mapped within the limestone sample. The fractures are predominantly sub-parallel to the target face. Radial scale is the square root of the weighted frequency.

set of open fractures < 0.2 mm wide and parallel to the crater floor. 6 mm below the crater floor is a zone of crushed ooids and very fine-grained material, much of it below the scale of observation (Figure 5.5g). There is another large open fracture (0.6-5.5 mm wide) starting at least 20 mm below the crater floor and oriented towards the lower left of the block (in section view) before intersecting the edge of the section area at a depth of 30 mm below the crater floor (central thin section in Figure 5.5a).

5.5 Discussion

5.5.1 Damage Mechanics

The experiments conducted here were carried out at conditions between hypervelocity and quasi-static experiments (Table 5.1), with potentially some overlap between the conditions for these ordnance impacts and those of hypervelocity impacts. Strain rates of 10^3-10^6 s^{-1} here compare with 10^4-10^4 s^{-1} for hypervelocity experiments and $<10^3$ s^{-1} for quasi-static experiments. Another way to compare the experimental conditions is the ratio of impact velocity to P wave velocity in the target: these experiments have values of 0.66 to 0.94 compared to values of 0.9 to 2.9 for hypervelocity and $\sim 10^{10}$ for quasi-static experiments. Despite these considerable differences, there are several features in common between the different experiments (Table 5.1).

The open fracture observed in the limestone sample dipping away from the crater resembles the 'near surface' fractures observed below hypervelocity impacts into gabbro (Figure 5.6) (Polanskey & Ahrens, 1990). Polanskey and Ahrens (1990) suggest that the fractures form along the boundary between a near surface region, as defined by Melosh (1984), and deeper regions of the target. In

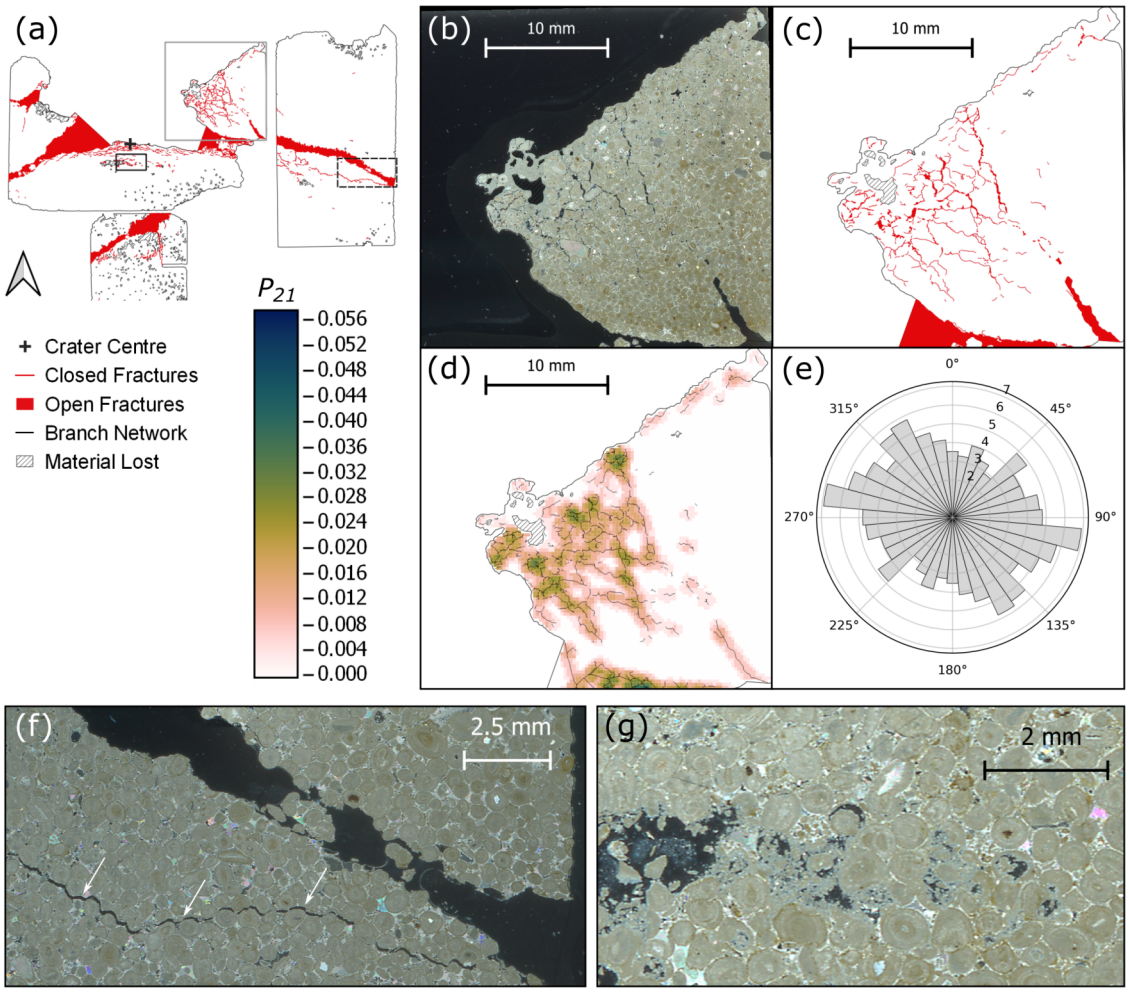

Figure 5.5: (a) Fracture map of the top central and right thin sections of sample CHCL_09 showing closed (red line) and open (solid red) fractures. Grey box indicates the location of panels (b-e), dashed black box indicates location of panel f and solid black box panel g. (b) Photomicrograph taken under cross polarised light (XPL) of an incipient wedge formed at the edge of the crater. (c) Fracture map showing multiple orientations of open and closed fractures in the wedge, corresponding to increased P_{21} intensity, as shown in panel d. (e) Equal area rose diagram of length weighted fracture orientations in panels b-d. Radial scale is the square root of the weighted frequency. (f) Photomicrograph under cross polarised light of a large open fracture present across several sections that intersects the edge of the target block. The fracture contains clasts of wall rock and has narrower fractures sub-parallel to it but several mm away (white arrows). (g) Photomicrograph under XPL highlighting a region of crushed ooids and carbonate material 6 mm below the crater floor.

the near surface region, target material experiences reduced peak compressive stress due to the reflection at a free surface of compressive stress waves as tensile waves of equal magnitude. As rock is generally weaker in tension than compression, these tensile waves can overcome rock strength and result in extensional fracturing, i.e. spallation. Polanskey and Ahrens (Polanskey & Ahrens, 1990) show good correlation of both location and orientation between the boundary of the near surface zone and 'near surface' fractures below hypervelocity impacts. Calculation of the near surface boundary for the experiments conducted here, as defined in Melosh (1984) (Equation 5.1), resulted in a depth below target surface (Z_p) of 4.2 – 9.3 mm for the limestone experiment (Figure 5.7a) and 4.1 – 14.2 mm for the sandstone experiment (Figure 5.7b).

$$Z_p = \frac{C_L T}{2}\left(\frac{4(d^2+s^2)}{4d^2 - C_L^2 T^2}\right)^{\frac{1}{2}} \tag{5.1}$$

Where C_L is the target sound speed, T is the rise time of the stress pulse (and $T \approx a/U$) where a is the projectile diameter and U is its impact velocity, d is the depth of burst, and s is the distance along the surface (X axis) from the impact point. The depth of burst is the effective centre of the spherical stress wave that diverges from the impact site and defined here as $d \approx 2a(\rho_p/\rho_t)^{\frac{1}{2}}$ with

	Hypervelocity Impact	**Ordnance Velocity Impact (This Study)**	**Quasi-Static Indentation**
Strain Rate (s^{-1})	10^4 - 10^9	10^3-10^6	$< 10^3$
v_i/C_L	0.9 – 2.9	0.66 – 0.94	$\sim 10^{10}$
Spall fractures	✓	✓	-
Conical fractures or zones of fracture	At the boundary of the near surface zone	5-10× the depth of the near surface zone	Cone cracks
Radial Fractures	✓	✓	✓
Concentric fractures	✓	✓	✓
Crater Mechanics	A point source equivalent to an explosion at depth	Momentum transfer	Quasi-static crack growth
References	i	ii	iii

Table 5.1: Summary of the similarities and differences in damage appearance and mechanisms for hypervelocity impacts, ordnance velocity impacts, and quasi-static indentation experiments. v_i = impact velocity, C_L = P-wave velocity. [i](Buhl, Kowitz, et al., 2013; Kenkmann et al., 2018; Veysset et al., 2021), [ii](Clifton, 1980; Walley, 1994; Rosenberg & Dekel, 2016), [iii](Chaudhri & Kurkjian, 1986; Bourne & Rosenberg, 1996; Grujicic et al., 2009; Veysset et al., 2021)

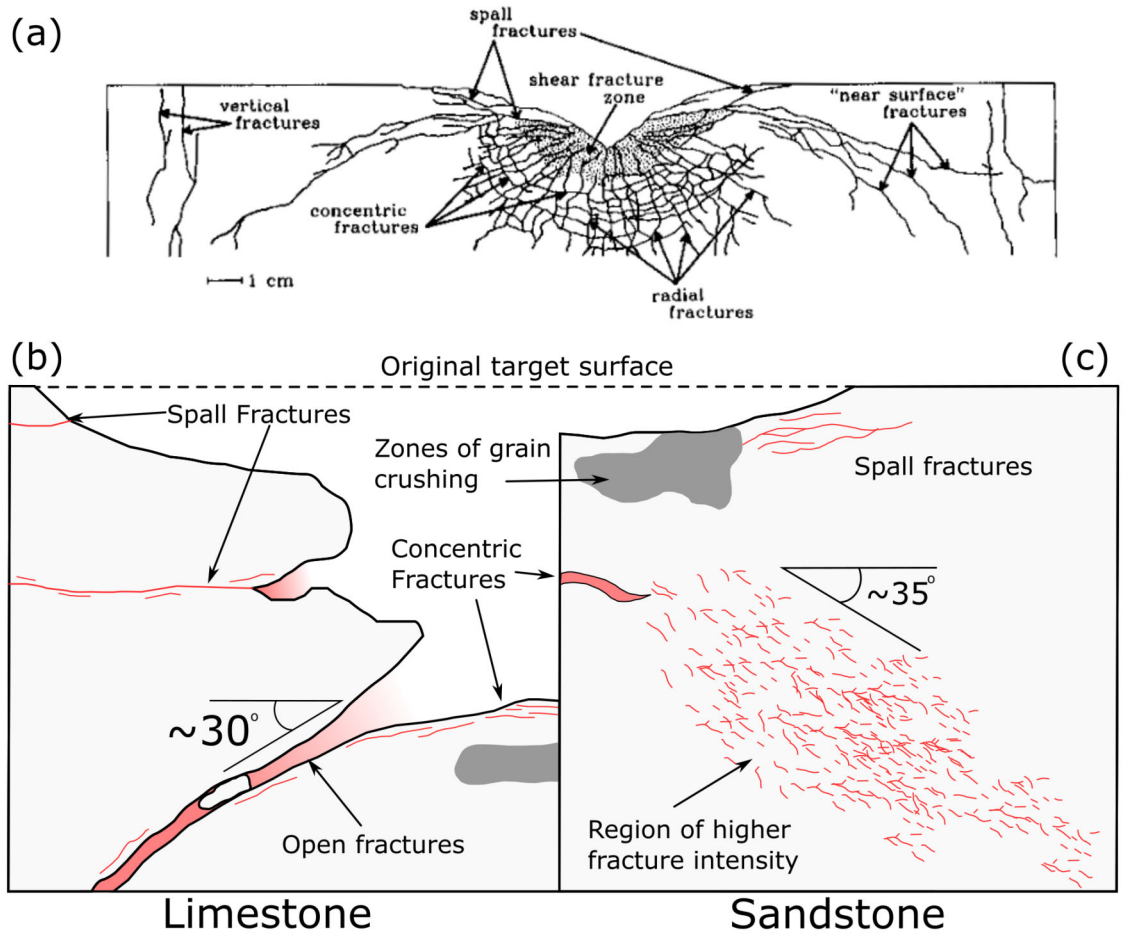

Figure 5.6: (a) Summary sketch of damage to San Marcos Gabbro during a hypervelocity impact (Polanskey & Ahrens, 1990). Schematics (not to scale) of damage observed in limestone (b) and sandstone (c) targets shot with 7.62 × 39 mm ammunition.

ρ_p the projectile density and ρ_t the target density (Melosh, 1984). In this equation d is similar to, but not the same as the 'depth of burst' for an explosion that produces a crater the same size as the impact, a common reference depth used in hypervelocity experiments. The value of d (38.8 mm) for the limestone target is similar to the maximum crater depth (42.5 mm), a similarity not observed in the sandstone target (36.6 vs. 5.1 mm). For both targets in this study, the theoretical hyperbola of the near surface boundary does not have a strong correlation with the observed subsurface fracturing (Figure 5.6). Fractures are present in the near surface zone of the sandstone target, but they are parallel to the crater floor or target surface, comparable to those labelled 'spall fractures' by Polanskey and Ahrens (1990) (Figure 5.6a). One experiment of Polanskey and Ahrens

(1990), using a commercial lead bullet fired as 890 $\mathrm{m\,s^{-1}}$, created near surface fractures with a steeper inclination than predicted by their theoretical near surface parabolas. The results of this experiment resemble the orientation of the increased fracture intensity zone in the sandstone target of this study. Winkler et al. (2018) observed localised shear zones below hypervelocity impacts into quartzites that dip away radially from the crater centre, some of which have orientations similar to those observed in the sandstone target of this study. The shape of the near surface zone is strongly controlled by the stress pulse caused by the impact (Melosh, 1984; Polanskey & Ahrens, 1990). The model discussed above assumes the rise time remains constant as shock/stress propagates (Melosh, 1984), which is unlikely for the ogive nose shape of the projectile in this study.

The conical form of the subsurface fractures in the target lithologies presented here also resemble conical cracks below indentation and contact loading studies into glass and ceramic targets (Cook & Pharr, 1990; Chen et al., 1995; Latella et al., 1997; Lawn, 1998; Chaudhri, 2015). Cone fractures, also known as Hertzian cracks, form initially as a ring crack around an indentor, before propagating in a conical form with continued load. It is conventionally assumed that the angle of the cone crack matches the pre-existing stress field with an angle of approximately 30° to the surface (Kocer & Collins, 1998), which is similar to the angle of the fracture in the limestone target and zone of increased fracture intensity in the sandstone target. Cone cracks are considered to propagate stably, requiring quasi-static conditions (Yoffe, 1982; Walley, 2010; Tumbajoy-Spinel et al., 2013; Küpferle et al., 2017). However, impact induced fracturing is generally thought to be a dynamic process, leading to multiple flaws propagating unstably instead of a single, stable fracture (Lawn & Wilshaw, 1975; Lange et al., 1984; Buhl, Kowitz, et al., 2013). Furthermore, the cone crack experiments use target materials with no porosity, contrasting with the relatively porous (11-20%) targets presented here. Chen et al. (2016) observed radial fractures around an indentor for target porosities between 5% and 45%, but no Hertzian cone cracks. They suggest this was due to the small radius of the indentor and relatively low target hardness resulting in plastic deformation before the critical load for cone crack formation could be reached. Impacts of flat ended projectiles into granite tiles at velocities of 207-537 $\mathrm{m\,s^{-1}}$ by Hogan et al. (2011) created conical cracks that reached the rear face of the target tiles. Other experiments impacting spherical projectiles into fused-silica and Pyrex targets, at velocities up to 340 $\mathrm{m\,s^{-1}}$, also resulted in conical cracks below the impact (Chaudhri, 2015). Similar impacts in the same study, but into soda-lime glass targets, produced an array of splinter cracks that resemble dynamic fracturing more than stable propagation, suggesting that target material has an influence on cone crack formation from impacts (Chaudhri, 2015). The loading rate (25 $\mathrm{\mu m\,s^{-1}}$) of Chen et al.'s (2016) indentation experiments

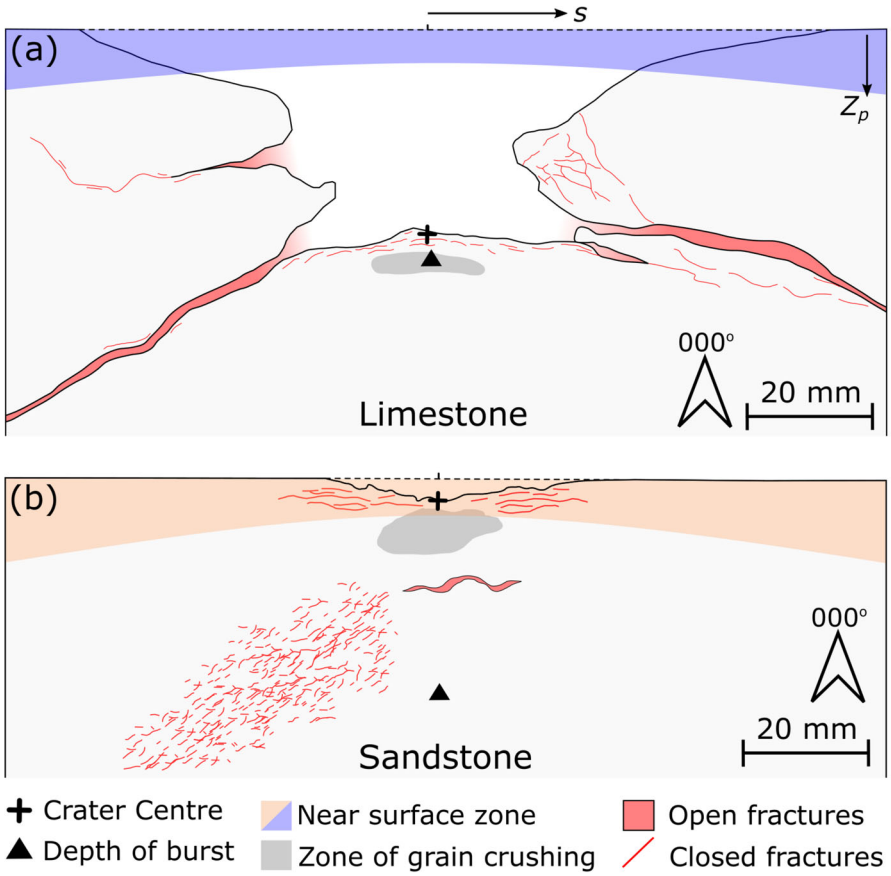

Figure 5.7: (a) Summary diagram of damage to Cotswold Hill Cream Limestone. The predicted depth of burst (d) (triangle) and crater centre are a similar distance below the original target face (dashed line). Z_p is the depth of the near surface zone parabola at lateral distance (s) from the impact point. The theoretical near surface zone is shaded blue. (b) Summary diagram of damage to Stoneraise Red Sandstone. The predicted depth of burst (d) (triangle) is substantially deeper in the target than the crater centre. Z_p is the depth of the near surface zone parabola at lateral distance (s) from the impact point. The theoretical near surface zone is shaded orange. Vertical and horizontal scales are the same.

is orders of magnitudes lower than experienced by the experiments of Chaudhri (2015), Hogan et al. (2011), and those presented here. Both Chaudhri (2015) and Hogan et al. (2011) described these conical fractures as Hertzian cone cracks, but their similarity to the experiments here, the limestone target in particular, suggests an alternative dynamic mechanism.

The propagation of radial fractures is observed in the hypervelocity, ordnance velocity, and quasi-static indentation experiments. Radial fractures form due to the tensile stress perpendicular

to the spherical compressive stress (or shock) wave caused by contact loading or impact into a target (Arakawa et al., 2000). Chen et al. (2016) observed four radial fractures in glass targets at orthogonal orientations around the indentor. They suggest the propagation of fractures in these orientations relieves stress in the interim regions, meaning that growth of the four fractures accommodates the increasing indentation load. The radial fractures observed in hyper- and ordnance velocity experiments are more numerous and have less regularity in their spacing. Impact loading creates far greater strain rates (Table 5.1) compared to those in Chen et al.'s (2016) experiments, possibly exceeded the ability of only a few orthogonally oriented and radial fractures to accommodate strain, resulting in new fractures forming in the interim areas. The propagation of multiple fracture strands at once is indicative of dynamic fracturing, observed by Chaudhri (2015) and Hogan et al. (2011).

Both target lithologies of this study exhibit extensional fractures parallel to the crater floor, resembling observations of concentric fractures below hypervelocity impacts (Polanskey & Ahrens, 1990; Kenkmann et al., 2011; Chen et al., 2016; Kenkmann et al., 2018) (Figure 5.6a, c). Similarly concentric fractures are also present beneath point loading experiments in glass and ceramics. However the fractures beneath the point loading experiments are thought to be caused during the unloading phase, as the load on the compressive zone below the indentor is released (Azeggagh et al., 2015; Chen et al., 2016).

Both hypervelocity and ordnance velocity impacts exhibit spall fractures at the edge of the crater. Where not directly visible in the subsurface, the presence of spallation is evident in the shallow dipping region surrounding the central excavation (Polanskey & Ahrens, 1990; Kenkmann et al., 2018; Campbell et al., 2022a). The spall fractures form when the initial compressive stress wave reaches the free surface of the target face and reflects back as tensile wave of equal magnitude (Melosh, 1984). Spall fractures are typically found close to the target face because the radial decay function causes wave energy to drop below the failure strength of the target material (Melosh, 1984; Polanskey & Ahrens, 1990; Poelchau et al., 2014). There are no spall fractures in quasi-static indentation experiments because the loading rates do not produce a stress wave of substantial magnitude. Instead the continual loading increases compressive stresses in the region directly below the loading.

The observations in this study have some similarities to those in both the near surface zone of hypervelocity experiments and Hertzian cone cracks, but different mechanisms involved in these ordnance velocity impacts preclude either the hypervelocity or cone crack mechanics from fully explaining the observations made here. The formation of spall fractures parallel to the target face

and crater floor show that tensile stress waves formed when the initial compressive stress wave was reflected at the surface. The interaction of these waves reflecting from the impacted face and adjacent sides of the target block may have caused regions of tensile failure, similar to the formation of the near surface zone in the hypervelocity experiments. However, the mechanics of the ordnance impacts, involving momentum transfer and longer interaction time between the projectile and target, and the geometry of the target blocks has resulted in a sufficiently different expression of subsurface damage that the theoretical near surface zone is not applicable. The hypervelocity (>1500 $\mathrm{m\,s^{-1}}$) experiments used spherical projectiles and cratering in these experiments was primarily controlled by the generation of a shock wave originating at some depth below the surface, but these conditions and processes may not be applicable to experiments presented here. Campbell et al. (2022a) found that bullet impacts with velocities of 400-900 $\mathrm{m\,s^{-1}}$ did not follow crater scaling relationships found in hypervelocity impacts. They also found that impact craters had identifiable crater asymmetry when impact trajectories were oblique (Campbell et al., 2022b). This asymmetry is not observed in hypervelocity impacts, except for those with very oblique trajectories (<15° to target face), because of the symmetrical nature of the point source model for hypervelocity cratering mechanics. Campbell et al. (2022b) suggest they observed crater asymmetry in their experiments because the impact velocity was lower than, or similar to, the sound speed of the target materials, so no shockwave was generated upon impact. Cratering was instead controlled by momentum transfer from the projectile to the target. This invalidates the point source assumption critical to hypervelocity. The impact velocities in this study (532 $\mathrm{m\,s^{-1}}$ and 539 $\mathrm{m\,s^{-1}}$) are lower than the respective P-wave velocity of the limestone (569 $\mathrm{m\,s^{-1}}$) and sandstone (822 $\mathrm{m\,s^{-1}}$) targets, so the generation of a shock wave at impact is unlikely. The results presented here support the suggestions made by Campbell et al. (2022a) that bullet impacts into stone are predominantly controlled by target properties, primarily material strength. Although there are some similarities between the damage created by hypervelocity experiments and this study, such as the near-surface fractures, spalling, and grain crushing below the impact, the damage mechanisms in each case are probably different.

5.5.2 Implications for Conservation

Fractures play a fundamental role in the transport of moisture and weathering agents by increasing porosity and linking together isolated pores within the stone (Cueto et al., 2009; Tiab & Donaldson, 2015). Both stone types have increased fracture intensity in the regions proximal to the bullet impact, as well as regions of increased fracture intensity or open fractures dipping

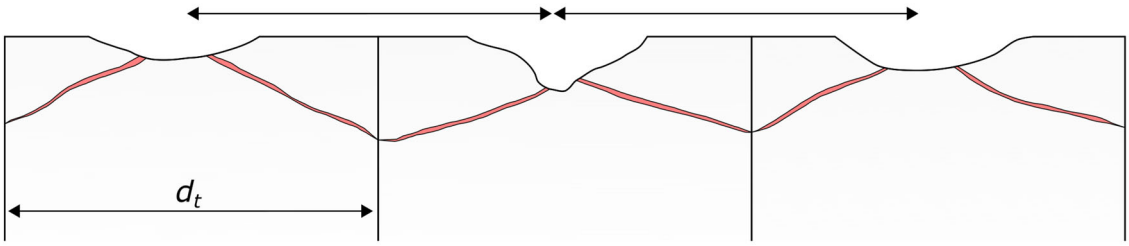

Figure 5.8: For impacts with a spacing less than the diameter of the impacted block d_t, subsurface conical fracture and damage zones can form an interconnected network that affects a greater region than suggested by the surface damage alone.

away from the impact crater at about 30°. Fracture width and intensity play a substantial role in influencing fracture capacity and transmissivity, with fracture intensity strongly correlated to overall permeability (Zhang & Sanderson, 1995; Tiab & Donaldson, 2015). The pattern of higher fracture intensities closer to the crater centre suggests that regions directly surrounding the impact will have the highest induced porosity and permeability, and may therefore be at the highest risk of weathering from moisture related processes. Higher surface permeability surrounding impact craters has been observed in historic and experimental impacts (Mol & Gomez-Heras, 2018; Gilbert et al., 2019). The large open fractures present in the limestone target creates localised areas of high fracture intensity that penetrate deep into the block. Higher fracture intensity has been linked to greater rates of weathering (Lebedeva & Brantley, 2017).

Because the open fracture dips away from the crater centre, most of the fracture is not visible from the surface. Hidden subsurface damage may affect a much larger region than visible surface damage. Fractures that intersect the sides of the impacted block can break along the mortar block boundary, or the mortar itself, possibly destabilising a wider region than just the impacted block (Tolch & Bushkovitch, 1947). Impact craters, particularly from shrapnel, commonly do not occur in isolation; structures typically have multiple impacts across their surface. If these impacts have subsurface damage zones similar to those in this study, there is the possibility they may link up in the subsurface. Figure 5.8 illustrates how multiple impacts with a spacing less than the impacted blocks diameter may form interconnect fracture networks below the surface that have greater footprint than the observable surface damage. The increased permeability and decreased stone strength resulting from the interconnected damage zones may lead to exacerbated material loss and greatly increase degree and rate of future deterioration. The interaction of subsurface damage from multiple impacts is an interesting and important avenue for future research.

The limestone target in this study has lower fracture intensities throughout, despite exhibiting greater surface damage than the sandstone sample. The P_{21} values of the limestone target do not a show a sharp increase within 10mm of the crater centre, as observed in the sandstone target. Energy above the requirement to exceed the target strength can be transferred as kinetic energy, causing material to be ejected from the impact site as ejecta, or the surrounding areas as spall fragments (Melosh, 1984). The lower tensile strength of the limestone compared to the sandstone may explain the larger crater dimensions in the limestone target, the maximum depth of the limestone crater is 42.5 mm, 8 times deeper than the crater in the sandstone. The region of highest fracture intensity in the limestone target may thus have been ejected.

The observations of impact induced fracturing in this study are important for conservator's post-conflict approaches to damaged heritage. Surface parallel spall fractures and interconnected subsurface conical fractures mean that regions with multiple impacts in close proximity may require rapid stabilisation to prevent substantial material loss. The increased permeability and porosity surrounding the impact mean these regions are at increased risk from moisture related deterioration (e.g. dissolution, salt crystallisation), so efforts for protecting against moisture, such as erecting temporary rain covers or shelters, can be prioritised where impacts are most numerous or exposed. Rapid observation of surface damage suggest where these priority actions should be focused for short term protection. Once a more detailed and comprehensive assessment of the damage and the risk of deterioration it poses, has been undertaken, then targeted and specific remediation efforts can be conducted. The results of this study support the results of (Mol & Gomez-Heras, 2018) and (Gilbert et al., 2019), further aiding the identification of priority regions for post conflict stabilisation

5.6 Conclusions

Apart from the visible surface crater, bullet impacts into stone create conical fractures or zones of increased fracture intensity below the impact, radial fractures, and spallation. Similar features are also seen in hypervelocity experiments and quasi-static indentation experiments that form cone cracks. However, the strain rates and impact velocities of bullet impacts are intermediate between the hypervelocity and quasi-static experiments, and the mechanisms causing damage are distinct from these experiments. Fracturing from the bullet impacts was dynamic (unlike cone crack experiments) but a shock wave did not form (as in hypervelocity experiments). Damage was caused by momentum transfer. The distinct conditions and damage mechanics in the bullet

impacts created differences in the details of the geometry of their damage compared to the faster and slower velocity impact experiments.

The subsurface damage caused by bullet impacts differs between target lithologies. Sandstone exhibits predominantly closed aperture inter- and intragranular fracturing, with some open fractures sub-parallel to the target face, as well as zone of grain size reduction and compaction directly below the crater. Limestone exhibits target surface parallel open fractures and open fractures curving away from the crater at angles of 30° and propped open by clasts of wall rock. These open fractures can intersect sides of the target block adjacent to the impacted face, potentially leading to the loss of large volumes of material.

P_{21} fracture intensity is highest closer to the crater centre in both lithologies and greatly decreases beyond 5-10 mm from the crater centre. This shows that the region directly surrounding the crater centre is at the greatest risk of deterioration from weathering. Regions at risk are not limited to the impact crater, open fractures and zones of higher fracture intensity adjacent to them provide conduits for moisture ingress and regions of increased susceptibility to weathering processes. These fractures have the potential to link up with subsurface fractures below adjacent impacts and exacerbate the risk of future deterioration from weathering processes across a much larger area. Small and apparently inconspicuous impact craters have subsurface damage that can extend up to 80 mm from the target face into the targeted block, but have little to no visible surface expression. This is important for proper surveying and post conflict risk assessments of heritage sites.

Chapter 6

Bullet-Induced Damage: Assessing Strain of Perpendicular vs. Oblique Impacts

6.1 Abstract

Controlled experiments were conducted to investigate the surface damage caused by perpendicular and oblique impacts of bullets into sandstone and limestone targets. Individual bullets fired under conditions simulating modern rifles, at typical combat distances, generated craters with diameters from 22 to 74 mm and depths from 3 to 24 mm. Craters in limestone targets were up to twice as large and deep as those in sandstone. Limestone craters showed a complex shape consisting of a central excavation surrounded by a shallow dish, compared to the simple bowl shape of most sandstone impacts. Radial fractures extending to the edge of the target block were common in limestone targets. Impacts at an angle of 45° to the surface in both rock types result in asymmetric craters. Two common types of cartridge (ammunition) were compared: the steel-tipped 5.56 × 45 mm NATO projectile, which generally produced larger and deeper craters than the 7.62 × 39 mm projectile that is commonly fired from AK-47 rifles, despite having approximately half the mass of the latter. These results characterise the magnitude and styles of damage that can be expected at many sites of cultural significance involved in contemporary conflict zones, and have important implications for their conservation: for example building stone with low tensile strength is likely

to sustain more damage and be at risk of greater deterioration.

Author Contributions

This chapter is based on a published manuscript: Campbell, O., Blenkinsop, T., Gilbert, O. and Mol, L. (2022). Surface Damage from Perpendicular and Oblique Bullet Impacts in Stone. *Royal Society Open Science*. 9:220029.
https://doi.org/10.1098/rsos.220029

Oliver Campbell is the main author of this work and undertook the creation of the photogrammetry models, characterisation of morphology, data processing, and wrote the manuscript. Oliver Campbell and Oscar Gilbert performed the controlled firearms experiments. Tom Blenkinsop and Lisa Mol provided supervision during the writing of the manuscript. Auriol Rae and an anonymous reviewer provided constructive comments that helped further improve the submitted manuscript.

6.2 Introduction

The aim of this chapter is to provide a quantitative assessment of damage caused by modern rifle bullets in scenarios typical of modern conflict, particularly to cultural heritage sites. Due to protections surrounding heritage, methods of study need to minimise additional damage or deterioration. Chapter 3 and Chapter 4 have shown that digital photogrammetry provides a means of capturing data from field sites for further analysis, and is a completely non-destructive approach. Such digital means have been useful in recording heritage and mapping decay (Jo & Lee, 2011; Fernández-Hernandez et al., 2015). This chapter applies the methods formulated in Chapter 3 to digital 3D models of experimental bullet damage into targets consisting of two different types of natural stone, with two different but commonly used types of ammunition. Up to this point, the thesis has focused predominantly on the damage caused by perpendicular impacts. This chapter compares crater morphology from perpendicular and 45° impacts, and suggests several criteria for differentiating them.

6.3 Methods Summary

Freshly quarried cubes (15 x 15 x 15 cm) of Stoneraise Red Sandstone (SRS)(18No.) and Cotswold Hill Cream Limestone (CHCL)(12No.) were selected as target stones. Controlled firearm experiments, as detailed in Chapter 2, were conducted to produce damaged blocks for analysis. Approximately 300-400 images for each damaged block were processed into 3D models using Meshroom. This number of images ensures the 'structure from motion' (SfM) software has enough common reference points of the entire target block to produce an accurate 3D mesh and texture file, facilitating additional observations of fractures on faces other than the target face. Digital cross sections obtained from the photogrammetry models were compared to manually measured Barton comb profiles.

6.4 Results

All samples experienced material loss and the formation of an impact crater on the target face which contained fine grained, powdery material and a pale discolouration in the central region. Crater size and morphology differs between lithology, angle of impact, and projectile type.

6.4.1 90° impact trajectory

Sandstone targets shot with AK-47 projectiles have shallow, bowl shaped craters with an average depth of 4.62 mm and an average diameter of 33.76 mm (Table 6.1). An average aspect ratio of 1.10 supports visual observations of a roughly circular shape. There are few visible surface fractures surrounding the craters, but if present, they are short and appear closed. Within and around some craters there is a dark grey discolouration from the lead core of the projectile. The cross section profiles through impacts have a rotational symmetry around the centre of the crater (Figure 6.1).

Limestone targets shot with the same projectile type have deeper (23.95 mm) and wider (73.97 mm) impact craters than sandstone targets. The crater morphology is composed of two regions, a steep sided central region, and surrounding that a shallower dipping spall region separated by a change in slope (arrows in Figure 6.2c). Some impacts have prominent radial fractures emanating from the crater edges, in some instances with apertures several mm wide and extending to adjacent faces. Other samples only have one or two radial fractures with narrow apertures (∼1 mm), which can also extend to the edge of the target face. Some samples have incipient spall fragments that are raised above the target face. They are bordered by very narrow aperture fractures that are roughly concentric to the crater edge.

Impacts into sandstone targets with NATO projectiles produced craters on average 2.9 times deeper (13.29 mm vs. 4.65 mm) and 1.5 times wider (50.82 mm vs. 33.76 mm) than AK-47 projectile impacts. Craters have a slightly higher aspect ratio of 1.17, and a crater outline that tends towards a square shape (Figure 6.3). Some craters have radial fractures with visible open apertures away from the crater. The steel tip from the projectile remains embedded in the crater floor. Crater profile morphology is more complex than the simple bowl craters observed in AK-47 projectile impacts. Profiles have a central region with steep sides and a shallow dipping outer spall region, similar to impacts of AK-47 projectiles into limestone targets.

Projectile	Target	Angle of Impact (°)	d (mm)	D_{eq} (mm)	Aspect Ratio	Fractures
5.56 × 45 mm NATO	Limestone	90	15.65	63.55	1.18	Radial, open fractures to the edge of the block.
		45	10.28	46.32	1.20	Open fractures mostly extend to edge of block.
	Sandstone	90	13.29	50.82	1.17	Radial open fractures in some samples.
		45	6.48	35.53	1.45	Few very short fractures with closed apertures.
7.62 × 39 mm (AK-47)	Limestone	90	23.95	73.97	1.08	Open radial fractures to the edge of the block. Spall fragments bordered by narrow fractures concentric with crater edge.
		45	8.99	41.22	1.21	One sample has open fractures to the edge of the block.
	Sandstone	90	4.62	33.76	1.10	Short fractures with closed apertures
		45	3.13	21.42	1.16	Narrow aperture fractures to the edge of the block in some samples.

Table 6.1: Summary of the average crater parameters for each firing condition and description of visible surface fractures on the target. d=max depth, D_{eq} = area equivalent diameter.

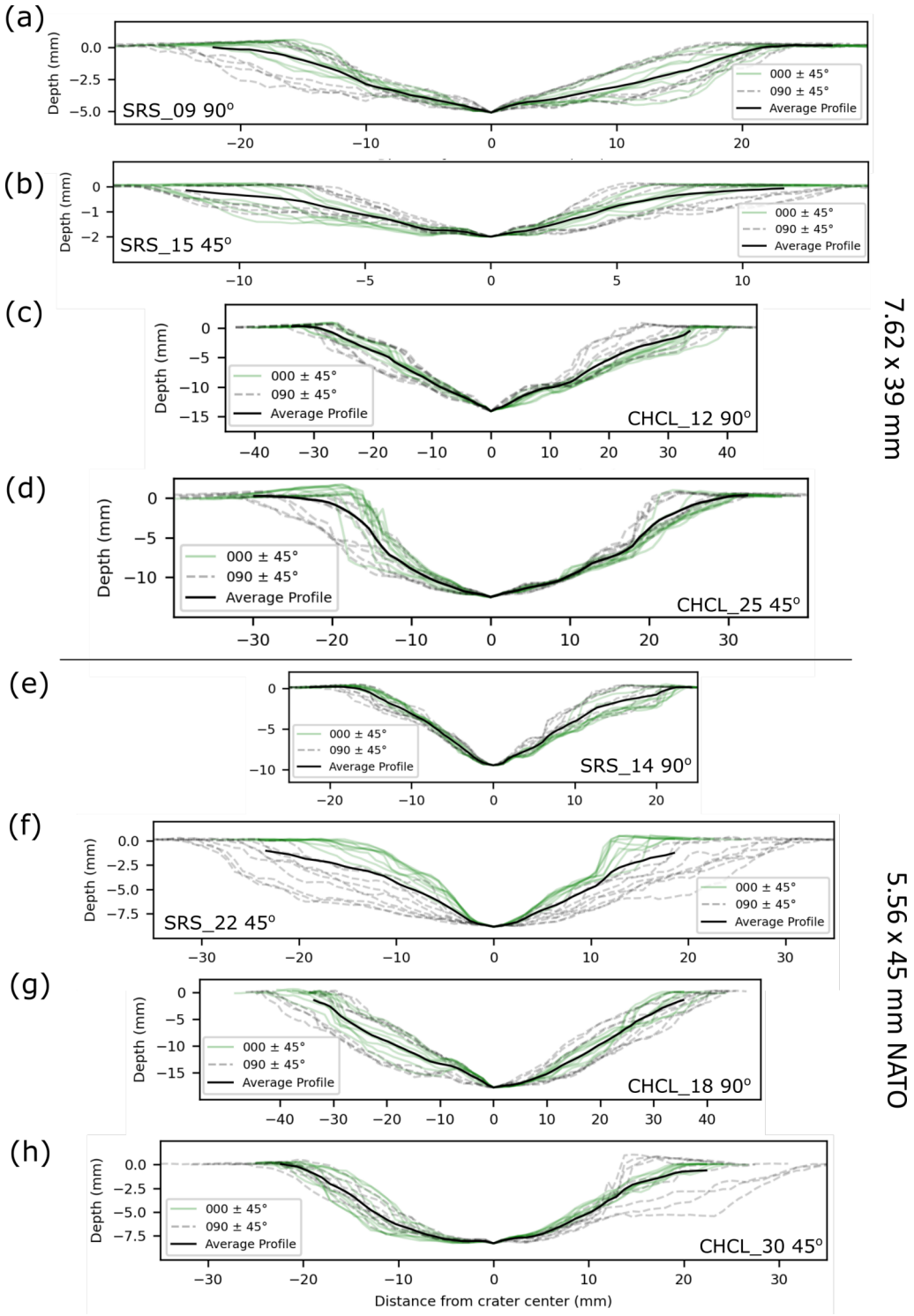

Figure 6.1: *Caption overleaf.*

Figure 6.1: (*Figure on previous page.*) Summary of 18 cross sections for each sample. Profiles ± 45° to 000° are coloured green, while profiles ± 45° to 090° are dashed grey. Note the asymmetry imposed by the 45° impact in sample SRS_22 (f). Profiles with similar azimuth to projectile trajectory (grey dash) have a wider diameter and shallower slopes, whilst profiles orthogonal to this (green) have steeper slopes and a narrow diameter. Other angled impacts show steeper dipping up-range sides and shallower dipping down-range ones (e.g. sample CHCL_25 (d) and CHCL_30 (h). Incipient spall fragments can be identified as areas raised above 0 mm depth on crater edges (e.g. between −20 and −10 mm on sample CHCL_25 (d) and +15 mm on sample CHCL_30 (h). Direction of projectile is left to right for 45° impacts.

Limestone targets shot with NATO projectiles have, on average, shallower (15.65 mm) and narrower (63.55 mm) craters than those shot with AK-47 projectiles. All craters have open radial fractures that extend to the edge of the block, though apertures are not as wide as seen in AK-47 projectile impacts. There are metal smears and grey lead deposits at the base of the craters, with the steel tip either embedded or absent, leaving a small central depression at the base of the crater. This depression is reflected in the cross sectional profiles as a vertical sided pit at the middle of the profile. Crater morphology is similar to other impacts in that it has a steep sided central region surrounded by a shallower dipping spall zone.

6.4.2 45° impact trajectory

Sandstone targets impacted with AK-47 projectiles at 45° have extremely shallow (3.13 mm) craters with an average diameter of 21.42 mm. Crater shape is still roughly circular with an aspect ratio of 1.16, though this is slightly larger than perpendicular impacts at the same conditions. Cross sections along the same axis as the projectile trajectory (C Profiles) show an asymmetry in morphology. They have a shorter, steeper wall on the up-range (towards 270°) side and a longer shallower wall on the down-trajectory side (towards 090°). The morphology of the orthogonal A profile is more symmetrical. Dark-grey lead residue is present on down-range regions of the crater edge and adjacent to the crater on the target face.

Limestone targets impacted by AK-47 projectiles at 45° have the highest aspect ratio (1.24) of all samples across both rock types impacted using this projectile. The impact craters are on average shallower (8.99 mm) and smaller in diameter (41.22 mm) than perpendicular impacts into the same target material. The two samples shot under these conditions, are quite different. One sample shot at 45° (CHCL_25) has incipient spall fragments at the crater edge, and open fractures that extend from the crater to the edge of the block. This differs from another sample (CHCL_28)

shot under the same conditions, which has no radial fractures around the crater and a greater difference between analogue and digital profiles (Table 6.2).

Projectile	**Target**	**Average RMS_N difference**
NATO	Limestone	6.0 %
		10.1 %
	Sandstone	9.2 %
		9.7 %
AK-47	Limestone	13.1 %
		15.7 %
	Sandstone	17.8 %
		14.2 %

Table 6.2: Average of normalised Root Mean-Square difference (RMS_N) between profiles obtained via the Barton comb method and from digital photogrammetry.

Oblique impacts of NATO projectiles into sandstone targets resulted in the most elongate craters of any conditions, with an average aspect ratio of 1.45. Crater depth averages 6.48 mm and average diameters 35.53 mm. These craters are larger than sandstone targets impacted by AK-47 projectiles at both angles of impact. The long axis of the crater is (sub-) parallel to the trajectory of the projectile. The cross section profiles reflect the higher aspect ratio, with profiles ± 45° of the A profile (000°) showing a narrower, steeper sided cross section, while profiles ± 45° of the C profile are wider with shallower dipping sides (Figure 6.1f).

Much like other angled impacts, NATO projectiles produce shallower (10.28 mm) and narrower (46.32 mm) impact craters in limestone targets than perpendicular impacts with the same projectile. Impact craters under these conditions generally fall into 2 groups based on crater morphology. The first group has many, open fractures radiating from the crater to the edge of the target block. Fracture orientations are predominantly between 000° and 180° i.e. in the down-range half of the block. This group also has multiple incipient spall fragments bordered by fractures concentric to the crater. The second group have fewer or no radial fractures visible, the occasional incipient spall fragment, and most have metal smears or traces of the projectile on the crater floor. Both groups show a distinct asymmetry in the C profile, with a short steep up-range wall and a longer shallow dipping down-range one (Figure 6.2).

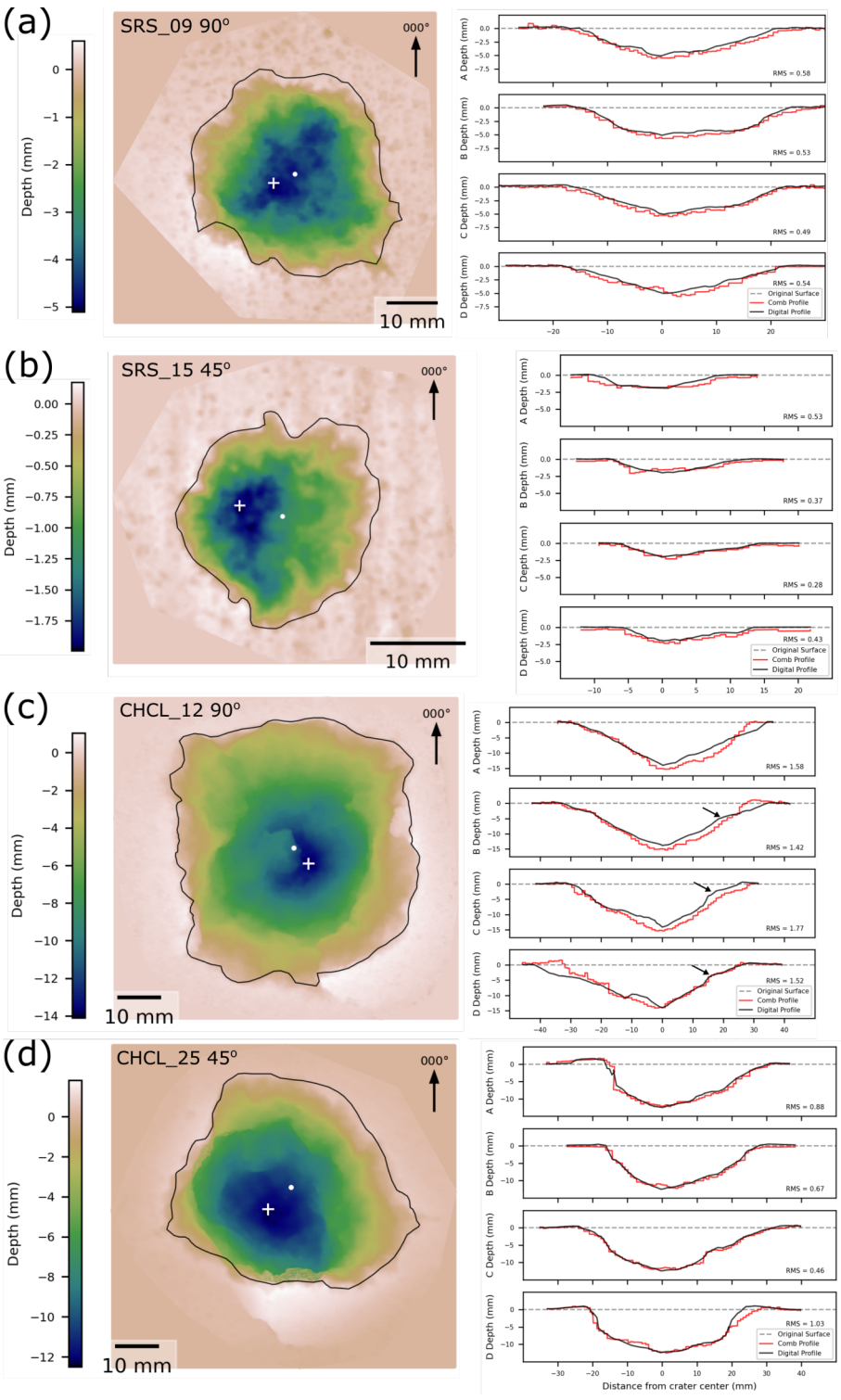

Figure 6.2: *Caption overleaf.*

Figure 6.2: (*Caption on previous page.*) Depth maps (left) of impact craters caused by 7.62 × 39 mm (AK-47) projectiles into blocks of Stoneraise Red Sandstone (SRS) (a-b) and Cotswold Hill Cream Limestone (CHCL) (c-d). Black line is the crater outline, the white cross (+) is the deepest point of the crater, and the white circle marks the geometric centre. Black arrows indicate the change of slope between central depression and outer spall zone. Direction of projectile is left to right for 45° impacts. Adjacent to each depth map (right) is a comparison of digital (black line) and analogue comb (red) profiles taken at 45° intervals starting at 000° (labelled A-D). The dashed grey line shows the original undamaged target face. Root Mean-Square difference (RMS) values are in mm. Profiles and depth maps of all samples can be found in supplementary data.

6.5 Discussion

There is a stark contrast in the crater morphology caused by AK-47 projectile impacts into sandstone and limestone targets. For perpendicular impacts, sandstone targets have simple, shallow, bowl-shaped craters, whereas limestone targets exhibit a two part structure of steep sided central pit and shallow dipping outer spall region (dish shaped). This two-part crater morphology is similarly observed during hypervelocity experiments into multiple target lithologies (Polanskey & Ahrens, 1990; Dufresne et al., 2013; Michikami et al., 2017). Reported strength values for similar rock types to this study (Mokattam Limestone vs. Umm Ishrin Sandstone), suggest the limestone targets have lower compressive (40 MPa vs. 105 MPa) and tensile strengths (1.3 MPa vs. 2.84 MPa) than the sandstone targets (El-Nahhas et al., 1990; Abdel-Mooty et al., 2013; Delmonaco et al., 2014). This difference in strength values based on lithology is dependent on its composition and microstructure, and a similar relationship may not apply for different lithologies. The restriction of spallation to the limestone targets, despite their higher porosity (and thus stress wave attenuation), is consistent with their lower tensile strength. Limestone targets have longer radial fractures with wider apertures than observed in sandstone targets, possibly linked to their greater porosity (20% vs. 11%) (Hatzor & Palchik, 1997).

All limestone targets had deeper and wider crater dimensions than in sandstone targets shot with the same conditions (Table 6.3). The different response of the two lithologies is due to the target properties, but pinpointing the exact variable is difficult from the experiments presented here. There is a paradoxical relationship in hypervelocity experiments between porosity, strength, and crater size. Increased porosity, when viewed independent of stone strength, acts to decrease crater size through the dissipation of energy during pore space collapse (Poelchau et al., 2013). Compressive strength of the target lithology has a similar effect on crater size: the stronger the

target material, the smaller the impact craters. However, increasing porosity decreases compressive strength, so while the decreased strength acts to increase crater size, the increased porosity acts to counter this (Palchik, 2006; Poelchau et al., 2013). The lower velocities (∼400-900 $\mathrm{m\,s^{-1}}$) of the experiments presented here may preclude a shockwave forming upon impact. In this case, momentum transfer from the projectile to the target controls crater excavation. Momentum transfer is influenced by both target and projectile properties. The steel tip of the NATO projectile is embedded, relatively intact, in the crater floor of some targets, because it is stronger than the all lead core of the AK-47 projectiles. The impact energy of both projectiles is similar, yet NATO projectiles result in larger crater volumes, suggesting projectile properties have caused greater momentum transfer to the target. The considerable differences between the damage caused in the two different rock types emphasises that consideration of target material properties, particularly the tensile strength, is a key aspect of evaluating and understanding bullet impact damage.

Angle	**7.62 × 39 (AK-47)**		**5.56 × 45 NATO**	
of Impact	d_{CHCL}/d_{SRS}	D_{CHCL}/D_{SRS}	d_{CHCL}/d_{SRS}	D_{CHCL}/D_{SRS}
90°	5.19	2.19	1.18	1.25
45°	2.87	1.92	1.59	1.30

Table 6.3: Ratios of the limestone (CHCL) to sandstone (SRS) crater dimensions show that for all conditions, limestone targets exhibit deeper and wider craters to sandstone counterparts. d=max depth, D = area equivalent diameter.

Oblique impacts can be distinguished from perpendicular impacts where stone type and projectile are the same. Perpendicular impacts are deeper and wider than comparable angled impacts, a pattern also observed in hypervelocity experiments with increasing obliquity (Michikami et al., 2017). This is due to perpendicular impacts transferring more kinetic energy to the target than oblique trajectories. Projectiles with oblique trajectories are more likely to ricochet, retaining

Figure 6.3: (*Figure overleaf.*) Depth maps (left) of impact craters caused by 5.56 × 45 mm NATO projectiles into Stoneraise Red Sandstone (a-b) and Cotswold Hill Cream Limestone (c-d). Black line is the crater outline, the white cross (+) is the deepest point of the crater, and the white circle marks the geometric centre. Direction of projectile is left to right for 45° impacts. Adjacent to each depth map (right) is a comparison of digital (black line) and analogue comb (red) profiles taken at 45° intervals starting at 000° (labelled A-D). The dashed grey line shows the original undamaged target face. Root Mean-Square difference (RMS) values are in mm. Profiles and depth maps of all samples can be found in supplementary data.

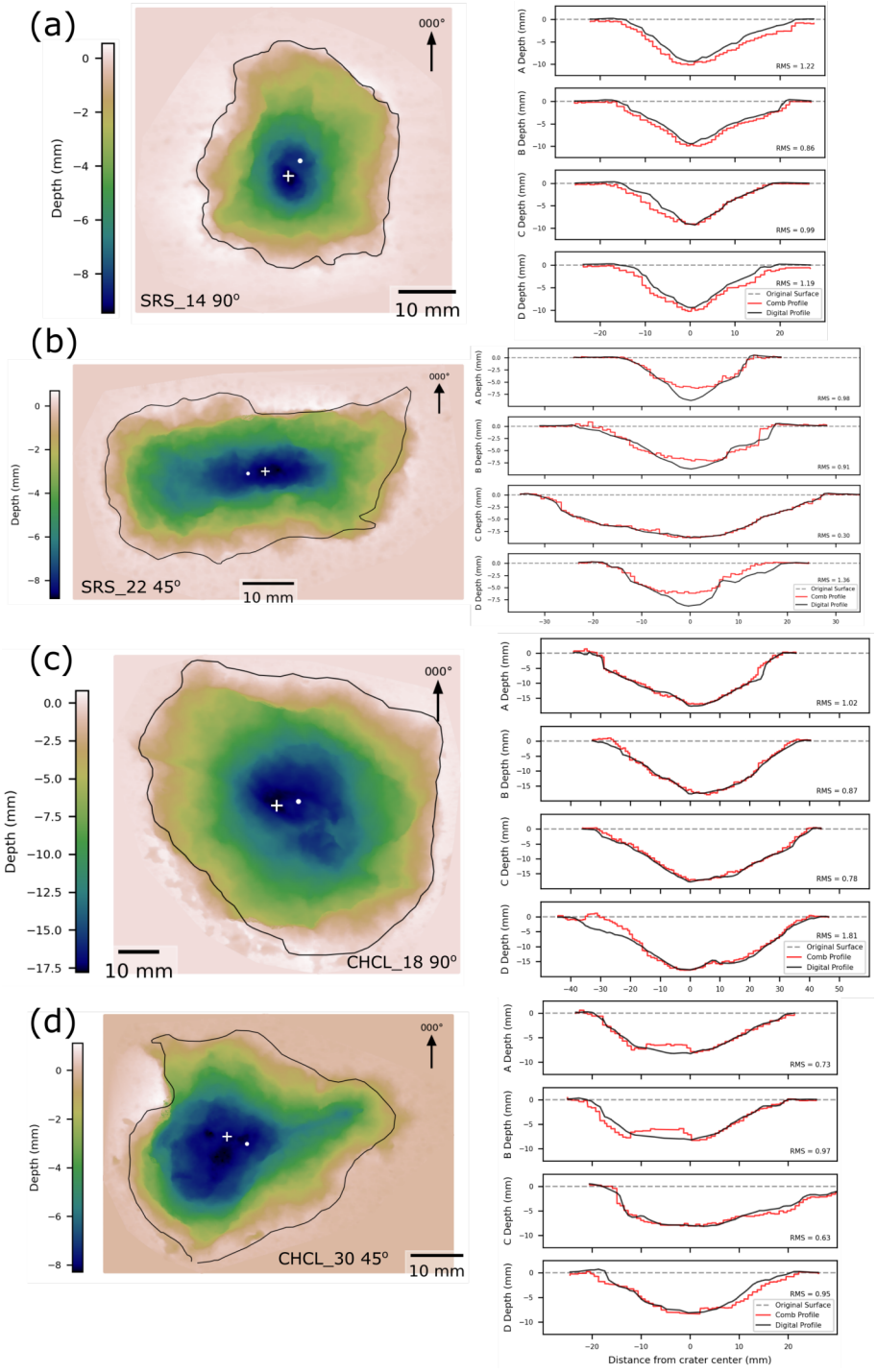

Figure 6.3: *Caption on previous page.*

kinetic energy that would otherwise be transferred to the target in a perpendicular impact (Gault & Wedekind, 1978). Crater size is also linked to the kinetic energy of the projectile, so with less energy transfer, the maximum stress values experienced in the target may not exceed its strength, resulting in less fracturing and smaller crater dimensions (Rinehart, 1968; Holsapple, 1993; Zhang et al., 2000).

All of the perpendicular impact craters have a broadly symmetrical distribution of damage around the point of impact, with no clear asymmetry in crater profiles. The planform crater shape is roughly circular, but spallation of plate-like clasts from crater edges has modified the crater outlines so that the aspect ratios diverge from 1 (perfectly circular) by average values up to 0.18. This modification has been observed in other impact experiments into natural stone (Dufresne et al., 2013). 45° impacts have higher aspect ratios than perpendicular impacts under similar conditions, but in many cases this difference is small, e.g. NATO projectiles into limestone targets (1.20 vs. 1.18) (Table 6.1). Threshold aspect ratios for characterising obliquity can be defined for given targets and projectiles (Table 6.1). NATO projectile impacts into sandstone targets have the highest aspect ratios, evident from the narrower diameters of the craters in A profiles compared to the C profiles (Figure 6.1).

In hypervelocity experiments involving granite targets, crater elongation does not occur until impact angles fall below 15°, and for loose sediment targets, less than 30° (Gault & Wedekind, 1978). This is due to hypervelocity impacts producing a hemispherical shock wave which drives the excavation of material from the crater (Braslau, 1970). The symmetry of the shock wave which drives the excavation of material results in circular impact craters except for very low incidence angles. The velocity range (∼400-900 $\mathrm{m\,s^{-1}}$) of the experiments presented here may be too slow to generate a hemispherical shock wave, so circularity may not occur in moderately inclined impact trajectories. Crater elongation is observed here for some conditions at impact angles of 45°, and cross section profiles in line with the impact trajectory (C profiles) show the same steep up range slope and shallow down range slope as very oblique hypervelocity experiments (Gault & Wedekind, 1978; Wallis et al., 2005). This may be the result of the asymmetric distribution of peak stresses down range of the impact point. Greater fracturing in this region may lead to increased excavation, and therefore increased crater diameter in this orientation, explaining the asymmetric aspect ratios observed. Wallis et al. (2005) show that subtle asymmetry is present in impacts with even a small degree of obliquity, though these impacts were into aluminium plates, which may not be directly comparable because of their ductile deformation. The Wallis et al. (2005) study does indicate that any obliquity can cause an asymmetric distribution of damage, suggesting that some regions of

stone surrounding the impact will be at risk of faster deterioration than others.

To properly combat future deterioration of impacted stone from weathering, it is important to understand the type of damage and its location. These experiments show that asymmetric cross section profiles, shallower and smaller craters, and higher aspect ratios characterise oblique projectile trajectories. Analogue measurement of profiles using a Barton comb is a simple and cheap way of collecting data in the field. This method can provide measurements of crater depth, diameter, and morphology, without additional processing. The method is however limited to sites and impact damage that are accessible to the researcher. Photogrammetry as an alternative is more versatile in terms of site accessibility and safety: aerial drones can successfully obtain imagery without direct access to a site (Fernández-Hernandez et al., 2015). Photogrammetry also preserves a digital record of the damage, that can be used to monitor change over time or measure additional variables (Kempa, 1993; Teza et al., 2019; Campbell et al., 2021). On the other hand, this method requires more post-collection processing to turn photographs into usable 3D models, which can be time consuming depending on the number of images and computing power available (Westoby et al., 2012). This study used between 300 and 400 images to generate 3D models of the target blocks in their entirety; this number could be reduced and still produce usable models. Gilbert et al. (2019) and Campbell et al. (2021) created and analysed a good-quality 3D model generated from only 142 images. Even fewer images could be used if only the impact crater was modelled.

Analogue collection methods for crater profiles allows the digital models to be 'ground-truthed' to damage observed in the field. The normalised Root Mean-Square difference (RMS_N) between the profiles produced by analogue and photogrammetric methods range from 6.0% to 17.8%. There are several factors to consider when evaluating the difference between analogue and digital profiles. Firstly, the Barton comb has a limited number ($\sim$150) of teeth with a set width ($\sim$1 mm), creating a stepped profile that can miss subtle changes in the crater morphology. The digital profile method interpolates between the point cloud data, allowing as many sample points along the profile as desired. This results in a much smoother profile, so even without any other source of difference, profiles from the two methods would not match perfectly. The normalised difference for deeper craters (e.g. those impacted with NATO projectiles) is consistently around 10%. Profiles from both methods are in reasonable agreement with each other, and therefore either method is a viable choice, depending on the specific research aims and conditions of the field site.

The use of non-destructive methods for assessing stone is invaluable for fragile and damaged heritage. For oblique impacts, internal damage, such as fracturing, may be more intense in a

downrange direction, as suggested by the shift in the location of peak pressures experienced with increasing obliquity (Pierazzo & Melosh, 2000a). The use of damage morphology to identify asymmetry and infer a possible downrange direction is a useful first approach to identify regions at risk. Following up with further non-destructive methods, such as surface hardness, ultra-pulse velocity, and surface permeability measurements can identify and corroborate damage surrounding impacts (Mol et al., 2017; Mol & Gomez-Heras, 2018; Gilbert et al., 2019). This would identify vulnerable regions at risk of increased capillary rise and salt-driven deterioration, allowing for more comprehensive and specific weathering risk assessments to be made. Such detailed assessments will prove invaluable to the conservation efforts of culturally important sites, especially those recently affected by armed conflict. In these areas, the opportunity for high resolution and highly technical investigations may be (temporarily) limited. This method could support relatively fast and inexpensive first-response documentation and interpretation of damage for those working *in situ*.

6.6 Conclusions

In experiments to investigate the surface damage caused by rifle bullets for conditions simulating modern conflicts, impacts excavated craters with diameters from 22 to 74 mm and depths from 3 to 24 mm. In all conditions, limestone targets had larger crater dimensions than sandstone targets. Limestone craters were from 1.2 to 5.1 times deeper than sandstone craters, and from 1.2 to 2.1 times greater in diameter. Limestone targets also exhibit a more complex, two part crater morphology consisting of a central excavation surrounding by a shallow dish shaped spall zone, compared to the simple bowl shape of the sandstone craters. Limestone targets had a higher occurrence of radial fractures extending from the crater to the edge of the block than sandstone targets. Target properties are a major factor in determining the extent and distribution of bullet and shrapnel damage, suggesting building stone with low tensile strengths are at greater risk of significant damage.

Impacts with an incident angle of 45° produced craters that were shallower and narrower than experiments shot at 90°. Oblique impacts also caused asymmetrical crater profiles, with a steep dipping up range slope and a shallower dipping down range one. Differences between perpendicular and oblique impact damage are quantifiable: for example, crater aspect ratios can distinguish perpendicular from oblique impacts for given target and projectile types. Of the two ammunition types, the 5.56 × 45 mm NATO projectiles produced larger and deeper craters than the 7.62 × 39 mm (AK-47) projectiles, as well as causing the most prominent asymmetry in crater profiles and

outlines for oblique impacts.

This characterisation of damage common to contemporary conflicts, with a focus on cultural heritage caught in the crossfire, is important for the conservation of affected sites.

Chapter 7

Conclusions and Further Work

The overall aim of this thesis was to understand the microstructures and deformation mechanisms of bullet impacts in stone, with a focus on its application to conflict damaged heritage by addressing the following questions:

1. To what extent does observable surface damage correlate with subsurface damage?
2. Can digital documentation effectively capture damage morphology?
3. How can we efficiently measure impact damage in the field?
4. What are the subsurface effects of bullet impacts in stone?
5. What influence does impact angle, target material, and projectile type, have on surface damage morphology?

The following section summarises the main findings of Chapters 3-5 to address these research questions. It then outlines conclusions summarising the main findings and suggests potential future work.

7.1 To what extent does observable surface damage correlate with subsurface damage?

Chapter 3 shows that fracture types visible on the surface of the crater floor under Scanning Electron Microscope (SEM) match fracture types just below the crater floor. Surface and subsurface observations show a shift from both circum-and intra-granular fracturing proximal to the

crater centre, to predominantly circumgranular fracturing further away. Visible surface damage is mostly localised around the point of impact as an excavated crater and surface fracturing, but some impacts have discrete radial fractures further away. In the subsurface, fracturing is more intense close to the crater centre, and decreases with increasing distance, with only larger open fractures penetrating deep into the target blocks (Chapter 5). Fractures intersecting the surface of the target, similar to the radial and surface parallel open fractures observed in the experiment documented in Chapter 3, were observed in the further experiments described in Chapter 5 to have open apertures in the subsurface, often propped open by clasts of wall rock. Mol and Gomez-Heras (2018) and Gilbert et al. (2019) measured increased surface permeability around impacts, with a good spatial relationship to impact craters and surface fracturing. The investigation of subsurface damage in Chapter 5 suggests that increased fracture intensity proximal to, and spall fracture around, the impact contributed towards the increased permeability measured by Mol and Gomez-Heras (2018) and Gilbert et al. (2019). Surface permeameters, like the TinyPerm III used in these studies, generally measure permeability in a shallow volume up to ∼10 mm from the probe (Mertz et al., 2016). The fracture intensity analysis undertaken in Chapter 5 showed that the highest P_{21} values are within ∼10 mm of the crater centre, and the spall fractures surrounding the crater are largely within 10 mm of the target face. These findings suggest that surface permeamters are a suitable method of identifying regions of increased fracturing around impacts during post-conflict assessment of damaged heritage. They also support a strong link between the observable and quantifiable surface damage and the unseen subsurface damage. The conical fracture, or zone of increased fracture intensity, dipping away from the crater centre which is reported in Chapter 5 shows that damage visible on, or in very close proximity to, the surface is intrinsically linked to damage at depth within the target.

7.2 Can digital documentation effectively capture damage morphology?

Digital photogrammetry is an effective tool in the conservation of heritage, whether it is creating 3D models of heritage to preserve them digitally, or using models for recording deterioration over time (Rizzi et al., 2007; Mol & Clarke, 2019; Teza & Pesci, 2019). The piolt study in Chapter 3 showed that the surface morphology of damage can be effectively captured and useful information extracted, such as the orientation of facets and estimates of the internal extent of

fractures. Chapter 6 showed that digital means can accurately capture crater morphology and resulting point clouds enable the measurement of many 3D variables, such as crater volume, or 2D variables such as cross section profiles. This supports other studies finding that Structure-from-Motion (SfM) photogrammetry is as accurate as other methods of modelling heritage, such as laser scanning (Koutsoudis et al., 2013; Brandolini & Patrucco, 2019). The photogrammetry models generated in this thesis show that subtle changes in the slope of crater walls are measurable, distinguishing between steeper angled central excavations and shallow dipping outer spall regions. The asymmetry of crater profiles can be quantified and its presence indicates oblique impact trajectories. 3D photogrammetry models provide greater flexibility for post processing analysis than analogue methods, where cross sections have to be individually measured by hand and crater volumes are difficult to measure in the field. Digital imagery offers several advantages over the collection of analogue measurements as a method of damage evaluation in heritage contexts. The capture of digital imagery is a 'hands-off' method that reduces the risk of causing additional damage or deterioration to potentially fragile stonework. Another advantage is the speed data can be collected in the field, and the greater number of options for post processing analysis.

Chapter 4 addresses this weakness in analogue methodologies, finding that the measurement of crater depth and diameter can be used to estimate crater volume in the field by simplifying crater geometry to a conical volume. This is an important finding for when site conditions prevent the capture of digital imagery suitable for SfM methods.

7.3 How can we efficiently measure impact damage in the field?

Non-destructive testing can require substantial time to collect sufficient measurements for reliable analysis, which may not always be possible in post-conflict assessment scenarios. As discussed, digital documentation provides an effective way of accurately capturing and analysing surface damage. The collection of images for generating 3D models is quick and requires little specialist equipment or training. This is advantageous over analogue methods where the measurement of multiple crater profiles and other crater geometries for each impact can take longer. However, in situations where a high number of impacts are to be studied, the use of SfM models has its limitations, primarily in the subsequent processing time required to generate a high number of models outweighing the time gains in the field. In these situations, simple volume approximations from

only two measurements of crater depth and diameter are a far more efficient means of investigating a high number of impacts. The use of simplified geometries can also be conducted in the field, meaning conservators can estimate crater volumes, as demonstrated in Chapter 45, for a site and tailor any further data collection based on those results.

7.4 What are the subsurface effects of bullet impacts in stone?

Fracture intensities are highest closest to the impact point, and decrease rapidly at approximately 10 mm from the impact (Chapter 3 and 5). This is observed for both sandstone and limestone targets, along with the transition in fracture type from circum- and transgranular fracturing close to the impact, to predominantly circumgranular fracturing further away (Chapter 5). Bullet impacts also cause conical fractures, or regions of increased fracture intensity, that dip away from the impact at about 30°. Fractures in close proximity to a free surface generally have orientations (sub) parallel to that surface as a result of tensile stress waves reflecting from that surface. Microstructural analysis suggests that the regions immediately surrounding the impact are at the most risk from future deterioration because they have the highest amount of fracturing, and therefore permeability and hardness reduction.

7.5 What influence does impact angle, target material, and projectile type, have on surface damage morphology?

As discussed in Chapters 6 and 4, impact cratering from bullets at ordnance velocities is primarily controlled by momentum transfer. The absence of a shockwave originating from a point source means that for oblique impact trajectories, the stress field during impact will not be symmetrical. Although the probability of exactly perpendicular impacts in conflict scenarios is low, the study of perpendicular impacts in this thesis has established a baseline of damage for future comparisons. This baseline showed that asymmetric crater morphology can be used to identify oblique impacts (Chapter 6). Oblique impacts result in asymmetric crater profiles, as well as smaller crater dimensions and volumes than for perpendicular impacts. Radial surface fractures also tend to have a down trajectory orientation, suggesting that alongside crater profiles, fracture damage is also asymmetrically distributed around the impact.

Gilbert et al. (2020) show relatively more deterioration from weathering across the target face for oblique impact than for perpendicular impacts, whilst perpendicular impacts experience greater weathering deterioration in the impact crater itself. They suggest that this is due to an increased intensity of shallow subsurface spall fractures in the oblique impacts, compared to increased fracture intensity surrounding the impact in perpendicular impacts. Fracture intensities created by perpendicular impacts are highest within 10 mm of the crater centre. This finding from Chapter 5 supports one aspect of this conclusion. Further studies are needed to determine how subsurface fracture intensities change with oblique impacts, and how different lithologies behave under subsequent weathering conditions.

Momentum transfer as the primary cratering mechanism means target properties play a substantial role in controlling the impact damage. Quantifying the exact effect of single target variables is difficult to achieve due to the complex nature of ballistic impacts, and the competing effect of different target properties on cratering mechanics, such as strength and porosity. In general, targets with greater porosity and lower tensile and compressive strengths produce deeper and wider impact craters than target materials that are less porous and have higher strength values. This is observed in Chapters 4 and 5 with limestone targets exhibiting wider, deeper, and more voluminous craters than sandstone targets under comparable impact conditions. The limestone targets were more porous than sandstone targets (20% versus 11% respectively) and have lower tensile (2.2 MPa versus 5.0 MPa) and compressive strengths (10.6 MPa versus. 40 MPa).

The properties of the projectile also have a strong influence on impact damage during momentum transfer. The stronger the projectile, the greater the amount of kinetic energy transferred to the target, and thus the greater the impact damage. This is observed in Chapters 4 and 5 with targets impacted by 5.56 $\times$ 45 mm NATO rounds with steel tips exhibiting larger craters than comparable experiments impacted by 7.62 $\times$ 39 mm rounds without steel tips. Targets impacted with 5.56 $\times$ 45 mm NATO often had short penetration tunnels at the crater centre, with the steel tip of the projectile remaining embedded and relatively underformed. Targets impacted with both projectile types showed little evidence of penetration by the lead or copper projectile material. These softer components likely deformed upon impact and ricocheted.

7.6 Conclusions

This thesis has investigated the microstructures and deformation mechanisms of bullet impacts in stone through a combination of digital photogrammetry models, analogue methods, and

microstructural analysis of impact damage generated during controlled firearm experiments. A pilot study proved the suitability of 3D photogrammetry methods and informed the design of a larger experimental campaign. The surface morphology of bullet impacts into stone were studied using 3D models of damage, analogue measurement of crater profiles, and simplified volume geometries. Subsurface damage was investigated using thin section samples from damaged targets. Microstructural observations and fracture intensity analysis show how impact damage beneath the target surface varies with distance from the point of impact. The main conclusions of this thesis are:

- Bullet impacts into stone cause an approximately conical crater, with a more complex two-part structure in limestone targets. Radial fractures are centred on the impact crater. Limestone targets have greater numbers, apertures, and lengths compared to similar impacts in sandstone targets.

- Bullet impact craters in limestone are 5× deeper, 2× wider, and more voluminous than comparable impacts into sandstone targets. Limestone targets also have a greater number of open radial fractures around the impact, some reaching faces adjacent to the target face .

- Impacts from 5.56 × 45 mm NATO projectiles produce deeper and larger volume craters in both target lithologies than 7.62 × 39 mm projectiles under comparable conditions . Impact craters from 5.56 × 45 mm NATO projectile in sandstone for example were 3× deeper, and twice as wide as craters from 7.62 × 39 mm. The steel penetrator of NATO ammunition often remains embedded in the target face of both lithologies.

- Oblique impacts cause shallower, narrower impact craters than perpendicular impacts under similar conditions. Oblique impacts can be discerned from perpendicular ones using asymmetry in the crater profiles of oblique impacts, and larger aspect ratios of the crater shape. Oblique impact trajectories produce an asymmetric stress field and distribution of damage.

- The volume of impact craters caused by bullet impacts can be approximated as a simple cone. Measurements of only depth and diameter can estimate crater volume to within 5% of the accurate volume measured from photogrammetry models.

- Bullet impacts into stone result in conical fractures, or zones of increased fracture intensity, that dip away from the impact point. These fractures have the potential to form interconnected networks that affect a larger region than is immediately obvious from the surface

damage. Observable surface damage from bullet impacts in stone therefore indicates the minimum likely extent of damage.

- Subsurface fracture intensity is greatest proximal to the impact, with peak average values of 0.02 mm^{-1} and 0.05 mm^{-1} for limestone and sandstone targets respectively, and rapidly decreases by at least 80% with distances greater than 10 mm from the crater centre. The demonstration of a link between the surface and subsurface damage supports the use of non-destructive testing and photogrammetry on damaged heritage as a way of informing on the subsurface condition of the stone.

- Subsurface damage to stone from bullet impacts is characterised by grain crushing and pore space collapse proximal to the impact point, with damage further from the impact characterised by discrete radial fracturing. Fractures tend to have a sub-parallel orientation to free surfaces where they are in close proximity to them.

- The formation of multiple and branching factures on both the surface and subsurface are indicative of dynamic fracture processes. Damage to stone from bullet impacts occupies a parameter space in between conditions from quasi-static loading and hypervelocity impact experiments. Damage observed in this thesis has similarities to observations in both quasi-static and hypervelocity experiments, such as radial fractures on the surface and in the subsurface, conical shaped fracture planes dipping away from the crater centre, and grain crushing below the loading point. However, the formation mechanisms in each type of experiment are different, with bullet impacts governed by momentum transfer, hypervelocity experiments governed by energy transfer, and quasi-static experiments following Griffith's steady state fracture mechanics.

7.7 Suggestions for Future Work

The results of this thesis have led to the formation of new questions on the damage caused by bullet impacts that were not addressed in this thesis.

Bullet impacts into sandstone and limestone targets have shown that the target material is one of the main influences on the size and extent of impact damage. However, built heritage has far more diversity in its construction materials, with marble, granite, and clay bricks all potential materials for future investigation. Experiments similar to those conducted here but with a wider range of target properties would strengthen the relationships proposed in this thesis, as well as

providing conservators with greater confidence in the applicability of experimental results to their particular field sites.

Additional experiments studying similar lithologies could build upon the work of this thesis by expanding the range of impact variables studied. Increasing the number of intervals for the angle of impact obliquity would improve our understanding of how crater morphology changes with angle of impact. This would provide baseline data for comparing to field scenarios where the angles of impact would be far more diverse that the two categories studied here. With these additional experiments comes a larger database of impact damage at a range of conditions. This larger dataset may enable the derivation of scaling relationships, using a similar approach to that taken for hypervelocity experiments, but resulting in the first relationships for ordnance velocity impacts. Conflict scenarios have more diverse causes of impact damage, with artillery and high explosives capable of creating variable and abundant shrapnel that can affect a wide area. With more possible sources of shrapnel projectiles, it is possible these impacts may be more numerous in a conflict situation than those caused by bullets. A study investigating the difference between damage caused by shrapnel and damage caused by bullet impacts would help ascertain the applicability of this thesis's findings to shrapnel impacts.

Chapter 5 characterised the subsurface damage caused by bullet impacts and found spatial relationships between greater damage intensity and the crater centre. This study only investigated in detail two samples out of the 8 produced during controlled firearm experiments, investigating the influence of lithology on the subsurface damage. Similar detailed investigation on the remaining samples and variables (angle of impact, projectile type) would provide the results to test the universality of the relationships proposed.

The use of additional technologies, such as X-Ray Computed Tomography (XRT), to investigate the subsurface fracturing in 3D would further improve our understanding of the nature and distribution of damage beneath bullet impacts. XRT has been successfully used to quantify the porosity of reservoir rocks (Verhelst et al., 1995; Yang et al., 2013; Martínez-Martínez et al., 2016), so could be adapted to image fractures and changes in porosity caused by bullet impacts. XRT was tried on samples of this study, but target block size limited the spatial resolution to a voxel size larger than the scale of the damage that was intended to be imaged. This would have to be overcome, possibly through a subsampling regime or smaller target blocks, but if successful would further the understanding of the spatial distribution of damage around bullet impacts, and would be a complementary method to destructive methods (thin sections) of investigating the microscale damage in the subsurface .

Photogrammetry has been proven useful in producing accurate 3D models to enable quantitative analysis of damage morphology. Whilst this study used ground based cameras, there is no reason why imagery obtained from drone based cameras cannot be used. Drone based photogrammetry has widespread use in the geoscience and heritage communities (Fernández-Hernandez et al., 2015; Manousakis et al., 2016; James et al., 2017; Hellman, 2018), but its application to the surveying of conflict damaged heritage is currently untested. A possible next step would be to develop and test a method for creating photogrammetry models of damaged heritage using drone based imaging. Post-conflict scenarios may still pose residual dangers to conservators seeking to access a site for assessment, so utilising remote operated drones would enable the damage to be assessed and regions of risk identified without risk to personnel.

Bibliography

Abdel-Mooty, M., Al Attar, A., & El Tahawy, M. (2013). Experimental evaluation of stone masonry walls with lime based mortar under vertical loads. https://doi.org/10.2495/978-1-84564-839-8/008

Allen, C. D., Ester, S., Groom, K. M., Schubert, R., Hagele, C., Olof, D., & James, M. (2018). A geologic assessment of historic saint elizabeth of hungary church using the cultural stone stability index, Denver, Colorado. In *Urban geomorphology: Landforms and processes in cities* (pp. 277–302). Elsevier. https://doi.org/10.1016/B978-0-12-811951-8.00014-X

Amnesty International. (2015). Taking Stock: The Arming of Islamic State. (December), 1–28.

Andrews, B., Roberts, J., Shipton, Z., Bigi, S., Chiara Tartarello, M., & Johnson, G. (2019). How do we see fractures? Quantifying subjective bias in fracture data collection. *Solid Earth*, *10*(2), 487–516. https://doi.org/10.5194/se-10-487-2019

Arakawa, M., Shirai, K., & Kato, M. (2000). Shock wave and fracture propagation in water ice by high velocity impact. *Geophysical Research Letters*, *27*(3), 305–308. https://doi.org/10.1029/1999GL010841

Azeggagh, N., Joly-Pottuz, L., Nélias, D., Chevalier, J., Omori, M., & Hashida, T. (2015). Hertzian contact damage in silicon nitride ceramics with different porosity contents. *Journal of the European Ceramic Society*, *35*, 2269–2276. https://doi.org/10.1016/j.jeurceramsoc.2015.01.031

Backman, M. E., & Goldsmith, W. (1978). The Mechanics of Penetration of Projectiles into Targets. *International Journal of Engineering Science*, *16*, 1–99.

Bahsforth, F. (1873). *A mathematical treatise on the motion of projectiles: Founded chiefly on the results of experiments made with the author's chronograph.* Asher & Company.

Baldwin, E. C., Milner, D. J., Burchell, M. J., & Crawford, I. A. (2007). Laboratory impacts into dry and wet sandstone with and without an overlying water layer: Implications for scaling

laws and projectile survivability. *Meteoritics and Planetary Science*, *42*(11), 1905–1914. https://doi.org/10.1111/j.1945-5100.2007.tb00549.x

Barnouin-Jha, O. S., Yamamoto, S., Toriumi, T., Sugita, S., & Matsui, T. (2007). Non-intrusive measurements of crater growth. *Icarus*, *188*(2), 506–521. https://doi.org/10.1016/j.icarus.2007.01.009

Booker, P. M., Cargile, J. D., Kistler, B. L., & La Saponara, V. (2009). Investigation on the response of segmented concrete targets to projectile impacts. *International Journal of Impact Engineering*, *36*(7), 926–939. https://doi.org/10.1016/j.ijimpeng.2008.10.006

Bourne, N. K., & Rosenberg, Z. (1996). The dynamic response of soda-lime glass. *AIP Conference Proceedings*, *370*, 567–572. https://doi.org/10.1063/1.50660

Brandolini, F., & Patrucco, G. (2019). Structure-from-motion (sfm) photogrammetry as a non-invasive methodology to digitalize historical documents: A highly flexible and low-cost approach? *Heritage*, *2*, 2124–2136. https://doi.org/10.3390/heritage2030128

Braslau, D. (1970). Partitioning of Energy in Hypervelocity Impact against Loose Sand Targets. *Journal of Geophysical Research*, *75*(20), 3987–3999.

Buhl, E., Kowitz, A., Elbeshausen, D., Sommer, F., Dresen, G., Poelchau, M. H., Reimold, W. U., Schmitt, R. T., & Kenkmann, T. (2013). Particle size distribution and strain rate attenuation in hypervelocity impact and shock recovery experiments. *Journal of Structural Geology*, *56*, 20–33. https://doi.org/10.1016/j.jsg.2013.08.007

Buhl, E., Poelchau, M. H., Dresen, G., & Kenkmann, T. (2013). Deformation of dry and wet sandstone targets during hypervelocity impact experiments, as revealed from the MEMIN Program. *Meteoritics and Planetary Science*, *48*(1), 71–86. https://doi.org/10.1111/j.1945-5100.2012.01431.x

Campbell, O., Blenkinsop, T., Gilbert, O., & Mol, L. (2021). Surface and Subsurface Damage Caused by Bullet Impacts into Sandstone. *Geosciences*, *11*(9), 395. https://doi.org/10.3390/geosciences11090395

Campbell, O., Blenkinsop, T., Gilbert, O., & Mol, L. (2022a). Bullet impacts in building stone excavate approximately conical craters, with dimensions that are controlled by target material. *Scientific Reports*, *12*, 1–11. https://doi.org/https://doi.org/10.1038/s41598-022-22624-

Campbell, O., Blenkinsop, T., Gilbert, O., & Mol, L. (2022b). Surface damage from perpendicular and oblique bullet impacts in stone. *Royal Society Open Science*. https://doi.org/https://doi.org/10.1098/rsos.220029

Chaudhri, M. M. (2015). Dynamic fracture of inorganic glasses by hard spherical and conical projectiles. *Philosophical Transactions of the Royal Society A: Mathematical, Physical and Engineering Sciences*, *373*. https://doi.org/10.1098/rsta.2014.0135

Chaudhri, M. M., & Kurkjian, C. R. (1986). Impact of small steel spheres on the surfaces of "normal" and "anomalous" glasses. *Journal of the American Ceramic Society*, *69*, 404–410. https://doi.org/10.1111/j.1151-2916.1986.tb04769.x

Chen, S. Y., Farris, T. N., & Chandrasekari, S. (1995). Contact mechanics of hertzian cone cracking. *International Journal of Solids and Structures*, *32*, 329–340. https://doi.org/10.1016/0020-7683(94)00127-I

Chen, Z., Wang, X., Atkinson, A., & Brandon, N. (2016). Spherical indentation of porous ceramics: Cracking and toughness. *Journal of the European Ceramic Society*, *36*, 3473–3480. https://doi.org/10.1016/j.jeurceramsoc.2016.05.010

Cho, S. H., Ogata, Y., & Kaneko, K. (2003). Strain-rate dependency of the dynamic tensile strength of rock. *International Journal of Rock Mechanics and Mining Sciences*, *40*(5), 763–777. https://doi.org/10.1016/S1365-1609(03)00072-8

Cignoni, P., Callieri, M., Corsini, M., Dellepiane, M., Ganovelli, F., & Ranzuglia, G. (2008). MeshLab: an Open-Source Mesh Processing Tool. *Eurographics Italian Chapter Conference 2008: Salerno, Italy*, 129–136. https://doi.org/10.2312/LocalChapterEvents/ItalChap/ItalianChapConf2008/129-136

Clifton, R. (1980). Material response to ultra high loading rates.

CloudCompare. (2020). Retrieved from: http://www.cloudcompare.org/.

Collins, A. L., Addiss, J. W., Walley, S. M., Promratana, K., Bobaru, F., Proud, W. G., & Williamson, D. M. (2011). The effect of rod nose shape on the internal flow fields during the ballistic penetration of sand. *International Journal of Impact Engineering*, *38*(12), 951–963. https://doi.org/10.1016/j.ijimpeng.2011.08.002

Conflict Armament Research. (2014). Dispatch From the Field: Islamic State Weapons in Iraq and Syria. (September), 18.

Cook, R. F., & Pharr, G. M. (1990). Direct observation and analysis of indentation cracking in glasses and ceramics. *Journal of the American Ceramic Society*, *73*, 787–817. https://doi.org/10.1111/j.1151-2916.1990.tb05119.x

Cueto, N., Benavente, D., Martıénez-Martıénez, J., & Garcıéa-del-Cura, M. (2009). Rock fabric, pore geometry and mineralogy effects on water transport in fractured dolostones. *Engineering Geology*, *107*(1-2), 1–15.

Delmonaco, G., Margottini, C., Spizzichino, D., & Khrisat, B. (2014). Rock slope potential failures in the Siq of Petra (Jordan). *Landslide Science for a Safer Geoenvironment: Volume 3: Targeted Landslides*, (June), 341–347. https://doi.org/10.1007/978-3-319-04996-0_52

Dershowitz, W. S., & Einstein, H. H. (1988). Characterizing rock joint geometry with joint system models. *Rock Mechanics and Rock Engineering 1988 21:1*, *21*(1), 21–51. https://doi.org/10.1007/BF01019674

Dershowitz, W. S., & Herda, H. H. (1992). Interpretation of fracture spacing and intensity.

Dufresne, A., Poelchau, M. H., Kenkmann, T., Deutsch, A., Hoerth, T., Schäfer, F., & Thoma, K. (2013). Crater morphology in sandstone targets: The MEMIN impact parameter study. *Meteoritics and Planetary Science*, *48*(1), 50–70. https://doi.org/10.1111/maps.12024

Ebert, M., Hecht, L., Deutsch, A., & Kenkmann, T. (2013). Chemical modification of projectile residues and target material in a MEMIN cratering experiment. *Meteoritics and Planetary Science*, *48*(1), 134–149. https://doi.org/10.1111/j.1945-5100.2012.1429.x

El-Nahhas, F., Moustafa, A., & Abdel-Tawab, S. (1990). Geotechnical characteristics of limestone formations of Gebel Mokattam area. *First Alexandria Conference on Structural and Geotechnical Engineering*, *1*(December), 9–19.

Fernández-Hernandez, J., González-Aguilera, D., Rodríguez-Gonzálvez, P., & Mancera-Taboada, J. (2015). Image-Based Modelling from Unmanned Aerial Vehicle (UAV) Photogrammetry: An Effective, Low-Cost Tool for Archaeological Applications. *Archaeometry*, *57*(1), 128–145. https://doi.org/10.1111/arcm.12078

Fitzsimmons, S. (2015). *Private Security Companies During the Iraq War - Military performance and the use of deadly force*. Taylor & Francis.

Franchi, R., Savelli, D., Colosi, F., Drapp, P., Gabrielli, R., Moretti, E., & Peloso, D. (2009). Petra and Beida (Jordan): two adjacent archaeological sites up to an exploitation of geomorphology-related topics for a cultural and touristic development Petra e Beida (Giordania): due siti archeologici confinanti idonei per una valorizzazione di temi. *Mem. Descr. Carta Geol. D'It.*, *87*, 77–90.

Frew, D. J. (2001). *Dynamic Response of Brittle Materials from Penetration and Split Hopkinson Pressure Bar Experiments* (tech. rep. No. 5). U.S. Army Engineer Research and Development Center. https://doi.org/ERDC/GSLTR-01-6

Gault, D. E., Shoemaker, E. M., & Moore, H. J. (1963). Spray ejected from the lunar surface by meteoroid impact. *NASA TN D-1767*, 40.

Gault, D. E., & Wedekind, J. A. (1978). Experimental studies of oblique impact. *Proceedings of 9th Lunar and Planetary Science Conference*, *9*, 3843–3875.

Gilbert, O., Mol, L., Campbell, O., & Blenkinsop, T. (2019). Permeability and Surface Hardness Surveying of Stone Damaged by Ballistic Impact. *Heritage*, *2*(2), 1369–1389. https://doi.org/10.3390/heritage2020087

Gilbert, O., Mol, L., Campbell, O., & Blenkinsop, T. (2020). The influence of angle of ballistic impact on stone weathering. *14th International Congress on the Deterioration and Conservation of Stone*, 309–313.

Goudie, A., & Viles, H. A. (1997). *Salt weathering hazard*. Wiley.

Greene, O., & Macaspac Penetrante, A. (2012). Arms, private militias and fragile state dynamics. In O. Greene & N. Marsh (Eds.), *Small arms, crime and conflict: Global governance and the threat of armed violence2* (pp. 138–159). Routledge.

Grujicic, M., Pandurangan, B., Coutris, N., Cheeseman, B. A., Fountzoulas, C., Patel, P., Templeton, D. W., & Bishnoi, K. D. (2009). A simple ballistic material model for soda-lime glass. *International Journal of Impact Engineering*, *36*, 386–401. https://doi.org/10.1016/j.ijimpeng.2008.08.001

Güttler, C., Hirata, N., & Nakamura, A. M. (2012). Cratering experiments on the self armoring of coarse-grained granular targets. *Icarus*, *220*(2), 1040–1049. https://doi.org/10.1016/j.icarus.2012.06.041

Hatır, M. E., İnce, İ., & Korkanç, M. (2021). Intelligent detection of deterioration in cultural stone heritage. *Journal of Building Engineering*, *44*(5), 102690. https://doi.org/10.1016/j.jobe.2021.102690

Hatzor, Y. H., & Palchik, V. (1997). The influence of grain size and porosity on crack initiation stress and critical flaw length in dolomites. *International Journal of Rock Mechanics and Mining Sciences*, *34*(5), 805–816. https://doi.org/10.1016/S1365-1609(96)00066-6

Helié, F. (1840). *Traité balistique expérimentale*. Dumaine.

Hellman, A. (2018). *Geohazard assessments of rock climbing sites Development of UAV and field based solutions* [Doctoral dissertation, University of Gothenburg].

Hogan, J. D., Spray, J. G., Rogers, R. J., Boonsue, S., Vincent, G., & Schneider, M. (2011). Microscale energy dissipation mechanisms during dynamic fracture in natural polyphase ceramic blocks. *International Journal of Impact Engineering*, *38*(12), 931–939. https://doi.org/10.1016/j.ijimpeng.2011.06.004

Holsapple, K. A., & Schmidt, R. M. (1982). On the scaling of crater dimensions - 2. impact processes. *Journal of Geophysical Research*, *87*(B3), 1849–1870. https://doi.org/10.1029/JB087iB03p01849

Holsapple, K. A. (1993). The Scaling of Impact Processes in Planetary Sciences. *Annual Review of Earth and Planetary Sciences*, *21*(1), 333–373. https://doi.org/10.1146/annurev.ea.21.050193.002001

Holsapple, K. A., & Schmidt, R. M. (1987). Point Source Solutions and Coupling Parameters in Cratering Mechanics. *Journal of Geophysical Research*, *92*(B7), 6350–6376.

Hörz, F. (1969). Structural and mineralogical evaluation of an experimentally produced impact crater in granite. *Contributions to Mineralogy and Petrology*, *21*(4), 365–377.

Housen, K. R., & Holsapple, K. A. (2011). Ejecta from impact craters. *Icarus*, *211*(1), 856–875. https://doi.org/10.1016/j.icarus.2010.09.017

Isakhan, B., & González Zarandona, J. A. (2018). Layers of religious and political iconoclasm under the Islamic State: symbolic sectarianism and pre-monotheistic iconoclasm. *International Journal of Heritage Studies*, *24*(1), 1–16. https://doi.org/10.1080/13527258.2017.1325769

James, M. R., Robson, S., D'Oleire-Oltmanns, S., & Niethammer, U. (2017). Optimising UAV topographic surveys processed with structure-from-motion: Ground control quality, quantity and bundle adjustment. *Geomorphology*, *280*, 51–66. https://doi.org/10.1016/j.geomorph.2016.11.021

Jancosek, M., & Pajdla, T. (2011). Multi-view reconstruction preserving weakly-supported surfaces. *Proceedings of the IEEE Computer Society Conference on Computer Vision and Pattern Recognition*, 3121–3128. https://doi.org/10.1109/CVPR.2011.5995693

Jo, Y. H., & Lee, C. H. (2011). Making Method of Deterioration Map and Evaluation Techniques of Surface and Three-dimensional Deterioration Rate for Stone Cultural Heritage. *Journal of Conservation Science*, *27*(3), 251–260.

Kamb, W. B. (1959). Ice petrofabric observations from Blue Glacier, Washington, in relation to theory and experiment. *Journal of Geophysical Research*, *64*(11), 1891–1909. https://doi.org/10.1029/JZ064I011P01891

Kempa, M. (1993). Monitoring the Weathering of Stone: Setup and First Results. *International Archives of Photogrammetry and Remote Sensing*, *29*, 292.

Kenkmann, T., Deutsch, A., Thoma, K., Ebert, M., Poelchau, M. H., Buhl, E., Carl, E.-R., Danilewsky, A. N., Dresen, G., Dufresne, A., Durr, N., Ehm, L., Grosse, C., Gulde, M., Güldemeister, N., Hamann, C., Hecht, L., Hiermaier, S., Hoerth, T., … Wünnemann, K.

(2018). Experimental impact cratering: A summary of the major results of the MEMIN research unit. *Meteoritics & Planetary Science*, *53*(8), 1543–1568. https://doi.org/10.1111/maps.13048

Kenkmann, T., Wünnemann, K., Deutsch, A., Poelchau, M. H., Schäfer, F., & Thoma, K. (2011). Impact cratering in sandstone: The MEMIN pilot study on the effect of pore water. *Meteoritics and Planetary Science*, *46*(6), 890–902. https://doi.org/10.1111/j.1945-5100.2011.01200.x

Kocer, C., & Collins, R. E. (1998). Angle of hertzian cone cracks. *Journal of the American Ceramic Society*, *81*, 1736–1742. https://doi.org/10.1111/j.1151-2916.1998.tb02542.x

Kosteski, L. E., Riera, J. D., Iturrioz, I., Singh, R. K., & Kant, T. (2015). Assessment of empirical formulas for prediction of the effects of projectile impact on concrete structures. *Fatigue and Fracture of Engineering Materials and Structures*, *38*(8), 948–959. https://doi.org/10.1111/ffe.12285

Koutsoudis, A., Vidmar, B., Ioannakis, G., Arnaoutoglou, F., Pavlidis, G., & Chamzas, C. (2013). Multi-image 3D reconstruction data evaluation. *Journal of Cultural Heritage*, *15*(1), 73–79. https://doi.org/10.1016/j.culher.2012.12.003

Krenn, P., Kalaus, P., & Hall, B. (1995). Material culture and military history: test-firing early modern small arms. *Material Culture Review/Revue de la*, *42*, 101–.

Kumar, P. S. (2005). Structural effects of meteorite impact on basalt: Evidence from Lonar crater, India. *Journal of Geophysical Research: Solid Earth*, *110*(12), 1–10. https://doi.org/10.1029/2005JB003662

Küpferle, J., Röttger, A., & Theisen, W. (2017). Fatigue and surface spalling of cemented carbides under cyclic impact loading – evaluation of the mechanical properties with respect to microstructural processes. *Wear*, *390-391*, 33–40. https://doi.org/10.1016/j.wear.2017.07.002

Lange, M. A., Ahrens, T. J., & Boslough, M. B. (1984). Impact cratering and spall failure of gabbro. *Icarus*, *58*(3), 383–395. https://doi.org/10.1016/0019-1035(84)90084-8

Latella, B. A., O'Connor, B. H., Padture, N. P., & Lawn, B. R. (1997). Hertzian contact damage in porous alumina ceramics. *Journal of the American Ceramic Society*, *80*, 1027–1031. https://doi.org/10.1111/j.1151-2916.1997.tb02940.x

Lawn, B. (1993). *Fracture of Brittle Solids*. Cambridge University Press. https://doi.org/10.1017/CBO9780511623127

Lawn, B. (1998). Indentation of ceramics with spheres: A century after hertz. *Journal of the American Ceramic Society*, *81*, 1977–1994. https://doi.org/10.1111/j.1151-2916.1998.tb02580.x

Lawn, B., & Wilshaw, T. (1975). *Fracture of brittle solids*. Cambridge University Press.

Lebedeva, M. I., & Brantley, S. L. (2017). Weathering and erosion of fractured bedrock systems. *Earth Surface Processes and Landforms*, *42*(13), 2090–2108. https://doi.org/10.1002/ESP.4177

Li, C. Q. (2003). Life-cycle modeling of corrosion-affected concrete structures: Propagation. *Journal of Structural Engineering*, *129*(6), 753–761. https://doi.org/10.1061/(ASCE)0733-9445(2003)129:6(753)

Luetzenburg, G., Kroon, A., & Bjørk, A. A. (2021). Evaluation of the apple iphone 12 pro lidar for an application in geosciences. *Scientific Reports*, *11*(1), 22221. https://doi.org/10.1038/s41598-021-01763-9

Manousakis, J., Zekkos, D., Saroglou, H., & Clark, M. (2016). Comparison of UAV-enabled photogrammetry-based 3D point clouds and interpolated DSMs of sloping terrain for rockfall hazard analysis. *International Archives of the Photogrammetry, Remote Sensing and Spatial Information Sciences - ISPRS Archives*, *42*(2W2), 71–77. https://doi.org/10.5194/isprs-archives-XLII-2-W2-71-2016

Martínez-Martínez, J., Fusi, N., Galiana-Merino, J., Benavente, D., & Crosta, G. (2016). Ultrasonic and x-ray computed tomography characterization of progressive fracture damage in low-porous carbonate rocks. *Engineering Geology*, *200*, 47–57. https://doi.org/https://doi.org/10.1016/j.enggeo.2015.11.009

McCabe, S., Smith, B. J., & Warke, P. A. (2010). Exploitation of inherited weakness in fire-damaged building sandstone: the 'fatiguing' of 'shocked' stone. *Engineering Geology*, *115*(3-4), 217–225. https://doi.org/10.1016/J.ENGGEO.2009.06.003

Melosh, H. J. (1980). Cratering Mechanics - Observational , Experimental, and Theoretical. *Annual Review of Earth and Planetary Sciences*, *8*(1), 65–93.

Melosh, H. J. (1984). Impact Ejection, Spallation, and the Origin of Meteorites. *Icarus*, *260*, 234–260.

Mertz, J., Colas, E., Yahmed, A. B., & Lenormand, R. (2016). Assesment of a non-destructive and portable mini permeameter based on a pulse decay flow applied to historical surfaces of porous materials. *13th International Congress on the Deterioration and Conservation of Stone. Science and Art: A Future for Stone*, 415–422.

Michikami, T., Hagermann, A., Morota, T., Haruyama, J., & Hasegawa, S. (2017). Oblique impact cratering experiments in brittle targets: Implications for elliptical craters on the Moon. *Planetary and Space Science*, *135*, 27–36. https://doi.org/10.1016/j.pss.2016.11.004

MKIP. (2022). Resource for collecting evidence of crimes against humanity and culture by the russian army. [[Online; accessed 2022-04-24]].

MOD-UK. (2018). Army field manual - Warfighting tactics: part 5b; mechanized and light infantry tactics.

Mol, L. (2017). Armed conflict impacts on the microscale. *Journal of Physics: Conference Series*, *902*(1), 012032. https://doi.org/10.1088/1742-6596/902/1/012032

Mol, L., Brassey, C., Clarke, L., Gilbert, O., Campbell, O., & Blenkinsop, T. (2020). Heritage in the crossfire. *2020*, 835–840.

Mol, L., & Clarke, L. (2019). Integrating structure-from-motion photogrammetry into rock weathering field methodologies. *Earth Surface Processes and Landforms*, *44*(13), 2671–2684. https://doi.org/10.1002/esp.4693

Mol, L., & Gomez-Heras, M. (2018). Bullet impacts and built heritage damage 1640–1939. *Heritage Science*, *6*(1), 35. https://doi.org/10.1186/s40494-018-0200-7

Mol, L., Gomez-Heras, M., Brassey, C., Green, O., & Blenkinsop, T. (2017). The benefit of a tough skin: bullet holes, weathering and the preservation of heritage. *Royal Society Open Science*, *4*(2), 160335. https://doi.org/10.1098/rsos.160335

Mol, L., & Green, O. (2015). Shot to pieces and shocked to the core. *infocus Magazine*, (38), 30–40. https://doi.org/10.22443/rms.inf.1.123

Mol, L., & Viles, H. A. (2012). The role of rock surface hardness and internal moisture in tafoni development in sandstone. *Earth Surface Processes and Landforms*, *37*(3), 301–314. https://doi.org/10.1002/ESP.2252

Moore, H. J., Gault, D. E., & Lugn, R. (1963). Experimental impact craters in basalt. *Transactions of the Society of Mining Engineers*, *226*, 258–262.

Moulon, P., Monasse, P., & Marlet, R. (2012). Adaptive Structure from Motion with a Contrario Model Estimation. In *Asian conference on computer vision* (pp. 257–270). https://doi.org/10.1007/978-3-642-37447-0_20

Navarre-Sitchler, A., Brantley, S. L., & Rother, G. (2015). How Porosity Increases During Incipient Weathering of Crystalline Silicate Rocks. *Reviews in Mineralogy and Geochemistry*, *80*(1), 331–354. https://doi.org/10.2138/RMG.2015.80.10

Nyberg, B., Nixon, C. W., & Sanderson, D. J. (2018). NetworkGT: A GIS tool for geometric and topological analysis of two-dimensional fracture networks. *Geosphere*, *14*(4), 1618–1634. https://doi.org/10.1130/GES01595.1

Palchik, V. (2006). Application of Mohr-Coulomb failure theory to very porous sandy shales. *International Journal of Rock Mechanics & Mining Sciences*, *43*, 1153–1162. https://doi.org/10.1016/j.ijrmms.2006.03.007

Pierazzo, E., & Melosh, H. J. (2000a). Melt Production in Oblique Impacts. *Icarus*, *145*, 252–261. https://doi.org/10.1006/icar.1999.6332

Pierazzo, E., & Melosh, H. J. (2000b). Understanding oblique impacts from experiments, observations, and modelling. *Annual Review of Earth and Planetary Sciences*, *28*(1), 87–124. https://doi.org/10.2499/2020focus13

Poelchau, M. H., Kenkmann, T., Hoerth, T., Schäfer, F., Rudolf, M., & Thoma, K. (2014). Impact cratering experiments into quartzite, sandstone and tuff: The effects of projectile size and target properties on spallation. *Icarus*, *242*, 211–224. https://doi.org/10.1016/J.ICARUS.2014.08.018

Poelchau, M. H., Kenkmann, T., Thoma, K., Hoerth, T., Dufresne, A., & Schäfer, F. (2013). The MEMIN research unit: Scaling impact cratering experiments in porous sandstones. *Meteoritics and Planetary Science*, *48*(1), 8–22. https://doi.org/10.1111/maps.12016

Polanskey, C. A., & Ahrens, T. J. (1990). Impact Spallation Experiments- Fracture Patterns and Spall Velocities. *Icarus*, *87*, 140–155.

Pope, G. A., Meierding, T. C., & Paradise, T. R. (2002). Geomorphology's role in the study of weathering of cultural stone. *Geomorphology*, *47*(2-4), 211–225. https://doi.org/10.1016/S0169-555X(02)00098-3

Rae, A. S. P., Kenkmann, T., Padmanabha, V., Poelchau, M. H., & Schäfer, F. (2021). Dynamic Compressive Strength and Fragmentation in Sedimentary and Metamorphic Rocks. *Tectonophysics PREPRINT*. https://doi.org/10.1029/2020JE006561

Rae, A. S., Kenkmann, T., Padmanabha, V., Poelchau, M. H., & Schäfer, F. (2020). Dynamic Compressive Strength and Fragmentation in Felsic Crystalline Rocks. *Journal of Geophysical Research: Planets*, *125*(10). https://doi.org/10.1029/2020JE006561

Rajput, A., & Iqbal, M. A. (2017). Ballistic performance of plain, reinforced and pre-stressed concrete slabs under normal impact by an ogival-nosed projectile. *International Journal of Impact Engineering*, *110*, 57–71. https://doi.org/10.1016/j.ijimpeng.2017.03.008

Ranzuglia, G., Callieri, M., Dellepiane, M., Cignoni, P., & Scopigno, R. (2013). MeshLab as a complete tool for the integration of photos and color with high resolution 3D geometry data. *CAA 2012 Conference Proceedings*, 406–416.

Ravi-Chandar, K. (1998). Dynamic fracture of nominally brittle materials. *Internation Journal of Fracture*, *90*(1901), 83–102.

Rinehart, J. S. (1968). Intense Destructive Stresses Resultign From Stress Wave Interactions. In B. M. French & M. Short, Nicholas (Eds.), *Shock metamorphism of natural materials* (pp. 31–42). Mono Book Corp.

Riquelme, A. J., Tomás, R., Cano, M., Pastor, J. L., & Jordá-Bordehore, L. (2021). Extraction of discontinuity sets of rocky slopes using iphone-12 derived 3dpc and comparison to tls and sfm datasets. *IOP Conference Series: Earth and Environmental Science*, *833*. https://doi.org/10.1088/1755-1315/833/1/012056

Rizzi, A., Voltolini, F., Girardi, S., Gonzo, L., Remondino, F., & Kessler-irst, F. (2007). Digital preservation , documentation and analysis of paintings , monuments and large cultural heritage with infrared technology , digital cameras and range sensors. *International Archives of the Photogrammetry, Remote Sensing and Spatial Information Sciences*, *36*((Part5/C53)), 1–6.

Road Research Laboratory. (1941). *The resistance of concrete to the penetration of high velocity projectiles resembling bomb splinters*. Department of Scientific and Industrial Research.

Robertson, H. (1941). *Terminal ballistics*. National Research Council.

Robins, B. (1742). *New principles of gunnery*. J Nourse.

Rosenberg, Z., & Dekel, E. (2016). *Terminal ballistics, second edition*. https://doi.org/10.1007/978-981-10-0395-0

Sancho, C., Fort, R., & Belmonte, A. (2003). Weathering rates of historic sandstone structures in semiarid environments (Ebro basin, NE Spain). *Catena*, *53*(1), 53–64. https://doi.org/10.1016/S0341-8162(02)00197-2

Sanderson, D. J., & Nixon, C. W. (2015). The use of topology in fracture network characterization. *Journal of Structural Geology*, *72*, 55–66. https://doi.org/10.1016/j.jsg.2015.01.005

Scherer, G. W. (2004). Stress from crystallization of salt. *Cement and Concrete Research*, *34*(9), 1613–1624. https://doi.org/10.1016/J.CEMCONRES.2003.12.034

Soe, K. T., Zhang, Y. X., & Zhang, L. C. (2013). Impact resistance of hybrid-fiber engineered cementitious composite panels. *Composite Structures*, *104*, 320–330. https://doi.org/10.1016/j.compstruct.2013.01.029

Sovják, R., Vavřiník, T., Zatloukal, J., Máca, P., Mičunek, T., & Frydrýn, M. (2015). Resistance of slim UHPFRC targets to projectile impact using in-service bullets. *International Journal of Impact Engineering*, *76*, 166–177. https://doi.org/10.1016/j.ijimpeng.2014.10.002

Stone, P. G. (2015). The Challenge of Protecting Heritage in Times of Armed Conflict. *Museum International*, *67*(1-4), 40–54. https://doi.org/10.1111/MUSE.12079

Teza, G., & Pesci, A. (2019). Evaluation of the temperature pattern of a complex body from thermal imaging and 3D information: A method and its MATLAB implementation. *Infrared Physics and Technology*, *96*(September 2018), 228–237. https://doi.org/10.1016/j.infrared.2018.11.029

Teza, G., Trevisani, S., & Pesci, A. (2019). The role of geoenvironmental sciences in Cultural Heritage preservation: the case of 1000 year old leaning bell tower of Caorle (Venice). *Journal of Cultural Heritage*, *39*, 270–277. https://doi.org/10.1016/j.culher.2019.03.013

Theoulakis, P., & Moropoulou, A. (1997). Microstructural and mechanical parameters determining the susceptibility of porous building stones to salt decay. *Construction and Building Materials*, *11*(1), 65–71. https://doi.org/10.1016/S0950-0618(96)00029-3

Thiele, S. T., Grose, L., Samsu, A., Micklethwaite, S., Vollgger, S. A., & Cruden, A. R. (2017). Rapid, semi-automatic fracture and contact mapping for point clouds, images and geophysical data. *Solid Earth*, *8*(6), 1241–1253. https://doi.org/10.5194/se-8-1241-2017

Tiab, D., & Donaldson, E. C. (2015). *Petrophysics: Theory and practice of measuring reservoir rock and fluid transport properties*. Gulf professional publishing.

Tikoff, B., Chatzaras, V., Newman, J., & Roberts, N. M. (2019). Big data in microstructure analysis: Building a universal orientation system for thin sections. *Journal of Structural Geology*, *125*, 226–234. https://doi.org/10.1016/J.JSG.2018.09.019

Tolch, N. A., & Bushkovitch, A. V. (1947). *Penetration and Crater Volume in Various Kinds of Rocks as Dependent on Caliber, Mass, and Striking Velocity of Projectile* (tech. rep.). Ballistic Research Labratories. Maryland.

Tumbajoy-Spinel, D. Y., Feulvarch, É., Bergheau, J. M., & Kermouche, G. (2013). 2d axisymmetric x-fem modeling of the hertzian cone crack system. *Comptes Rendus - Mecanique*, *341*, 715–725. https://doi.org/10.1016/j.crme.2013.09.004

Verhelst, F., Vervoort, A., De Bosscher, P., & Marchal, G. (1995). *X-ray computerized tomography: Determination of heterogeneities in rock samples* (Vol. All Days) [ISRM-8CONGRESS-1995-023].

Veysset, D., Lee, J. H., Hassani, M., Kooi, S. E., Thomas, E. L., & Nelson, K. A. (2021). High-velocity micro-projectile impact testing. *Applied Physics Reviews*, *8*. https://doi.org/10.1063/5.0040772

Vollmer, F. W. (1995). C program for automatic contouring of spherical orientation data using a modified Kamb method. *Computers and Geosciences*, *21*(1), 31–49. https://doi.org/10.1016/0098-3004(94)00058-3

Walley, F. (1994). The effect of explosions on structures. *Proceedings of the Institution of Civil Engineers: Structures and Buildings*, *104*(3), 325–334. https://doi.org/10.1680/istbu.1994.26782

Walley, S. M. (2010). Historical review of high strain rate and shock properties of ceramics relevant to their application in armour. *Advances in Applied Ceramics*, *109*(8), 446–466. https://doi.org/10.1179/174367609X422180

Wallis, D., Burchell, M. J., Cook, A. C., Solomon, C. J., Mcbride, N., Burchell, †. M. J., Cook, A. C., Solomon, C. J., & Mcbride, N. (2005). Azimuthal impact directions from oblique impact crater morphology. *Monthly Notices of the Royal Astronomical Society*, *359*(3), 1137–1149. https://doi.org/10.1111/j.1365-2966.2005.08978.x

Weiss, T. G., & Connelly, N. (2017). Cultural Cleansing and Mass Atrocities: Protecting Cultural Heritage in Armed Conflict Zones. *J.Paul Getty Trust Occasional Papers in Cultural Heritage Policy*, *1*.

Westoby, M. J., Brasington, J., Glasser, N. F., Hambrey, M. J., & Reynolds, J. M. (2012). 'Structure-from-Motion' photogrammetry: A low-cost, effective tool for geoscience applications. *Geomorphology*, *179*, 300–314. https://doi.org/10.1016/j.geomorph.2012.08.021

White, M. P. (1946). *Effects Of Impact and Explosion* (tech. rep.). OSD or Non-Service DoD Agency. Defense Technical INformation Centre. https://doi.org/10.21236/AD0221586

Winkler, R., Luther, R., Poelchau, M. H., Wünnemann, K., & Kenkmann, T. (2018). Subsurface deformation of experimental hypervelocity impacts in quartzite and marble targets. *Meteoritics and Planetary Science*, *53*(8), 1733–1755. https://doi.org/10.1111/maps.13080

Wünnemann, K., Nowka, D., Collins, G. S., Elbeshausen, D., & Bierhaus, M. (2011). Scaling of impact crater formation on planetary surfaces – insights from numerical modeling. *Proceedings of the 11th Hypervelocity Impact Symposium*, (120), 1–16.

Yang, Z., Ren, W., Mostafavi, M., McDonald, S. A., & Marrow, T. J. (2013). Characterisation of 3D fracture evolution in concrete using in situ x ray computed tomography testing and digital

volume correlation. *VIII international Conference on Frature Mechanics of Concrete and Concrete Structures*, 1–7.

Yankelevsky, D. (1997). Local Response of Concrete Slabs to Low Velocity Missile Impacts. *International Journal of Impact Engineering*, *19*(4), 331–343.

Yoffe, E. H. (1982). Elastic stress fields caused by indenting brittle materials. *Philosophical Magazine A: Physics of Condensed Matter, Structure, Defects and Mechanical Properties*, *46*, 617–628. https://doi.org/10.1080/01418618208236917

Zhang, Q. B., & Zhao, J. (2014). A review of dynamic experimental techniques and mechanical behaviour of rock materials. *Rock Mechanics and Rock Engineering*, *47*(4), 1411–1478. https://doi.org/10.1007/s00603-013-0463-y

Zhang, X., & Sanderson, D. J. (1995). Anisotropic features of geometry and permeability in fractured rock masses. *Engineering Geology*, *40*(1-2), 65–75.

Zhang, Z., Kou, S., Jiang, L., & Lindqvist, P. A. (2000). Effects of loading rate on rock fracture: Fracture characteristics and energy partitioning. *International Journal of Rock Mechanics and Mining Sciences*, *37*(5), 745–762. https://doi.org/10.1016/s1365-1609(00)00008-3

Appendix

Please find the Appendix materials in the digital repository submitted alongside this thesis.

Appendix A: Huesca Sandstone 3D Photogrammetry Model

Appendix B: Cotswold Hill Cream Limestone 3D Photogrammetry Models

Appendix C: Stoneraise Red Sandstone 3D Photogrammetry Models

Appendix D: Crater Depth Maps for CHCL and SRS Targets

Appendix E: Profile Method Comparisons for CHCL and SRS Targets

Appendix F: Python Script of Methods Used in Chapter 6

Appendix G: Crater Geometry Data and RMS Values used in Chapter 6

Appendix H: Impact Variables, Crater Geometry, and Complied Literature Data Used in Chapter 4

Appendix I: QGIS Package for Fracture Intensity Analysis of Sample CHCL_09

Appendix J: QGIS Package for Fracture Intensity Analysis of Sample SRS_09